Università degli Studi di Pavia

Faculty of Engineering
Department of Electrical, Computer and Biomedical Engineering

Master Degree in Industrial Automation Engineering
Robotics and Mechatronics

Development and Validation of an Optical System for 3D Morphological Reconstruction of Cutting Tools

Supervisor:
Luca Lombardi

Co-supervisor:
Alessandro Peverelli

Candidate:
Simone Revelli

Student ID:
544735

Academic Year 2024/2025

Abstract

In the current manufacturing context, tool presetting systems still rely mainly on two-dimensional optical measurements, which are effective for inspecting projected profiles but limited when the objective is to describe the actual morphology of the cutting edge. Within this framework, this thesis aims to identify the technology best suited to support an evolution of industrial presetting toward a three-dimensional measurement approach.

The work is based on a comparative study of the main three-dimensional acquisition technologies applicable to the inspection of cutting tools. Among the solutions considered, laser triangulation and structured light proved to be the most promising in terms of metrological sensitivity and compatibility with industrial constraints. On this basis, an experimental validation phase was carried out through static tests on certified gauge blocks and industrial tools, aimed at evaluating repeatability, spatial dispersion, and robustness in the presence of reflective metallic surfaces.

Building on this validation phase, the main contribution of the thesis consists in the development of a workflow dedicated to the three-dimensional reconstruction of cutting tools from multiple acquisitions. The proposed procedure makes it possible to align and merge partial scans into a common tool-centered reference system and to interactively extract local sections for the geometric analysis of functional surfaces. The results obtained with laser triangulation show that, through four angular scans, it was possible to obtain coherent and metrically meaningful 3D reconstructions, from which local profiles were extracted. Structured light, by contrast, exhibited higher surface noise, lower useful coverage per view, and less robust multi-view reconstruction. Overall, laser triangulation proved to be the most suitable technology for a three-dimensional extension of industrial tool presetting.

Sommario

Nel contesto manifatturiero attuale, i sistemi di presetting degli utensili si basano ancora prevalentemente su misure ottiche bidimensionali, efficaci per l'ispezione di profili proiettati ma limitate quando l'obiettivo è descrivere la reale morfologia del tagliente. In questo quadro, la presente tesi si propone di individuare la tecnologia più adatta a supportare un'evoluzione del presetting industriale verso una modalità di misura tridimensionale.

Il lavoro si basa su uno studio comparativo delle principali tecnologie di acquisizione tridimensionale applicabili all'ispezione di utensili da taglio. Tra le soluzioni considerate, triangolazione laser e luce strutturata sono risultate le più promettenti in termini di sensibilità metrologica e compatibilità con i vincoli industriali. Su questa base è stata condotta una fase di validazione sperimentale mediante prove statiche su blocchetti pianparalleli certificati e su utensili industriali, finalizzata alla valutazione di ripetibilità, dispersione spaziale e robustezza in presenza di superfici metalliche riflettenti.

A partire da questa fase di validazione, il contributo principale della tesi consiste nello sviluppo di un workflow dedicato alla ricostruzione tridimensionale di utensili da taglio da acquisizioni multiple. La procedura proposta consente di allineare e unire scansioni parziali in un sistema di riferimento comune centrato sull'utensile e di estrarre interattivamente sezioni locali per l'analisi geometrica delle superfici funzionali. I risultati ottenuti con la triangolazione laser mostrano che, mediante quattro scansioni angolari, è stato possibile ottenere ricostruzioni 3D coerenti e significative, dalle quali sono stati estratti profili locali. La luce strutturata, al contrario, ha evidenziato maggiore rumore superficiale, minore copertura utile per vista e una ricostruzione multivista meno robusta. Nel complesso, la triangolazione laser si è dimostrata la tecnologia più adatta per l'evoluzione 3D del presetting.

Contents

List of Figures

List of Tables

Acronyms

CNC Computer Numerical Control

BUE Built-up Edge

CMOS Complementary Metal-Oxide-Semiconductor

CCD Charge-Coupled Device

VDI/VDE Verein Deutscher Ingenieure / Verband der Elektrotechnik

MR Measurement Range

CD Clearance Distance

FOV Field of View

ROI Region of Interest

Chapter 1

Introduction

In the context of modern manufacturing, production processes require increasingly high levels of automation, data integration, and quality control. Computer numerical control (CNC) machines operate at increasing speeds and with high precision in order to meet the dimensional tolerances required by the most advanced manufacturing sectors. Within this framework, tool metrology is playing an increasingly important role, since tool geometry significantly affects machining behavior, process stability, and tool service life. The availability of reliable geometrical information therefore makes it possible not only to verify compliance with dimensional specifications, but also to support presetting, monitoring, and process optimization activities in a more informed way. For this reason, the metrological analysis of cutting tools must now simultaneously meet the demands of production, measurement accuracy, and technological innovation.

1.1 Industrial context and problem statement

Within this scenario, two-dimensional optical presetting systems have reached a high level of technological maturity over time and still represent a well-established solution for the measurement of numerous geometrical parameters. These systems are particularly effective when the required metrological information can be reliably derived from the projection of the tool profile onto an observation plane, while ensuring speed, robustness, and operational accuracy compatible with the industrial environment.

However, the evolution of production requirements, the increasing geometrical complexity of cutting tools, and the demand for ever tighter micrometric tolerances are making the intrinsic limitations of an exclusively two-dimensional approach increasingly evident. In many cases, indeed, the observation of a projected profile alone is not sufficient to describe the actual morphology of the tool in a complete manner, especially when the aim is to analyze complex geometries in which micrometric details are present, particularly in correspondence with the cutting edges.

The transition toward three-dimensional analysis thus becomes relevant not merely as a technological evolution, but as a response to a concrete metrological need. The possibility of acquiring the 3D geometry of the tool would in fact make it possible to overcome some of the inherent limitations of 2D measurement, providing a more complete description of the surface and opening the way to more advanced evaluations, both in geometrical terms and in terms of the potential analysis of wear conditions or the morphological characteristics of the cutting edges.

This transition, however, is not without difficulties. The introduction of three-dimensional technologies into an industrial context requires compliance with particularly demanding constraints, including high metrological accuracy, acquisition repeatability, noise management, data reliability, compatibility with limited measurement times, and the possibility of integration with existing machines and procedures.

1.2 Objectives and contributions

The present work assessed the feasibility of extending presetting systems to both two-dimensional and three-dimensional analysis modes through advanced acquisition technologies compatible with the constraints of the target industrial environment.

To this end, a comparative study of the main 3D technologies applicable to the case under investigation was carried out, examining their operating principles, limitations, and potential with respect to the required metrological specifications. This analysis made it possible to identify the most promising solutions in terms of expected accuracy, integration feasibility,

and availability of surface information relevant to tool analysis.

A subsequent experimental phase was then developed for the preliminary validation of the selected solutions, including the integration of sensors on the reference machines and the definition of the acquisition setup. The work also involved the acquisition and processing of the raw data provided by the selected sensors, which were not directly compatible with the measurement software already in use within the company, thus making the development of dedicated tools necessary.

Scripts and procedures were developed in Python and MATLAB for the two-dimensional analysis of profiles, including functions for edge detection, angle estimation, calculation of characteristic lengths, and evaluation of deviations from expected values. Procedures were also defined for the processing of three-dimensional data, with the aim of obtaining reliable geometric representations and progressive reconstructions of the tool from the available acquisitions. Finally, visualization and geometric verification activities were carried out using external point-cloud processing software in order to complete and validate the results obtained.

These activities made it possible to establish an initial methodological and experimental framework for evaluating the potential use of 3D technologies in industrial presetting, highlighting both opportunities and critical issues related to the integration of additional surface views and geometric reconstruction procedures within an application context that requires precision, repeatability, and reliability.

1.3 Industrial partnership

The present thesis activity was carried out within the framework of an industrial collaboration between iMAGE S S.p.A. and Speroni S.p.A., whose contributions proved to be complementary throughout the different phases of the project.

iMAGE S contributed as a technology partner in the field of machine vision, supporting both the preliminary analysis of the most suitable optical technologies and the subsequent experimental evaluation of the selected sensors. Its contribution was particularly relevant in the study of the different acqui-

sition principles, in the identification of their expected operating ranges and limitations, as well as in the interpretation of the performance declared by manufacturers. On this basis, initial validation tests were carried out in order to assess, under controlled yet application-oriented conditions, to what extent the behavior of the considered sensors was consistent with the specifications reported in the corresponding datasheets. In addition, the technical collaborators of iMAGE S supported the work throughout the analysis and experimental phases, providing technical guidance in the evaluation and comparison of the different solutions, while leaving the final choices to the thesis work itself.

Speroni, on the other hand, provided the industrial application context in which the project found its concrete implementation, making available its presetting machines and supporting the integration of the considered sensors on the available systems. This aspect was particularly relevant, since it made it possible to perform tests under realistic operating conditions while exploiting the high positioning accuracy and motion-control capabilities of the machines themselves. As a result, the experimental activity could be carried out on a stable and metrologically reliable platform, suitable for the preliminary validation of the selected acquisition approaches. In addition, the technical staff of Speroni provided continuous support during the setup and testing phases, contributing practical knowledge of the machines, the measurement workflow, and the main constraints associated with the industrial use case.

Within this collaborative framework, the thesis therefore took shape as a study and preliminary experimental validation path developed in close connection with an actual industrial environment. The combined contribution of iMAGE S and Speroni made it possible to address the problem from both a technological and an application-oriented perspective: on the one hand through a reasoned analysis of the candidate vision technologies and their potential, and on the other hand by maintaining constant reference to the practical requirements of tool measurement and machine integration.

Chapter 2

State of the art

This chapter analyses the main theoretical and technological elements required to address the dimensional inspection of cutting tools by means of optical measurement systems. It first introduces the geometric parameters of interest and the reference framework required to describe the local geometry of the cutting edge. The main metrological challenges associated with their measurement are then discussed, including the need to describe the spatial orientation of micrometric surfaces, the geometric complexity of the profiles, the reflectivity of the surfaces, and the stringent accuracy requirements imposed by the application context. The chapter then examines two-dimensional optical presetting systems, highlighting their established role in industrial practice and the limitations that emerge when the analysis requires information that cannot be obtained from a single profile projection. This is followed by a comparative review of the main three-dimensional acquisition technologies potentially applicable to the case under study, including laser triangulation, structured light, stereo vision, focus variation, and confocal microscopy. Finally, the chapter concludes by defining the technology selection criteria adopted in this work, which provide the basis for comparing the different solutions analysed and for identifying the most suitable approach for the application under consideration.

2.1 Cutting Tool Geometry

The geometry of a cutting tool cannot be described solely in terms of linear dimensions, since cutting-edge behaviour depends not only on nominal sizes, but also on the relative orientation of the functional surfaces involved in chip formation and interaction with the newly machined surface. In this work, the rake angle is denoted by γ, the clearance angle by α, and the wedge angle by β. These quantities are the main local parameters used to describe cutting-edge geometry and to relate nominal tool design to actual cutting behaviour.

To introduce these concepts, a solid end mill is adopted as a representative example. This choice is motivated by its strongly three-dimensional geometry, characterised by helical cutting edges, flutes, and local tooth surfaces whose orientation cannot be fully captured by a simple two-dimensional profile. Although the discussion focuses on an end mill, the same geometric principles also apply to many other cutting tools, including twist drills, single-point turning tools, indexable inserts, reamers, and inserted milling cutters. The end mill is therefore used as an explanatory case study rather than as the only relevant tool geometry.

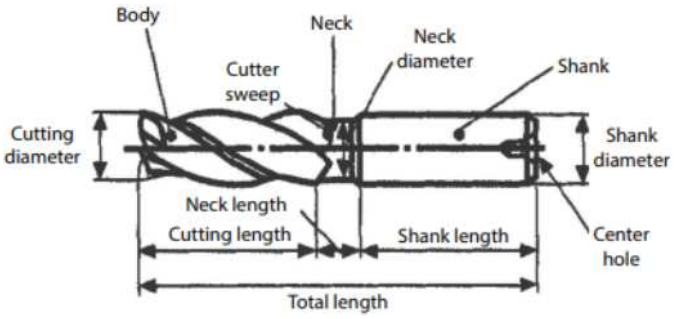

Figure 2.1: General geometry of a solid end mill, showing the main structural and dimensional regions of the tool. Adapted from [1].

Considering the overall geometry of the tool, the *body* identifies the active cutting portion of the end mill, i.e., the region containing teeth and flutes. The *neck* is the transition zone between the cutting region and the shank, often reduced in diameter to improve accessibility and avoid interference during machining. The *neck diameter* denotes the diameter of this transition region, whereas the *shank* is the clamped portion of the tool and the *shank diameter* its nominal diameter. The *cutting diameter* is the external

diameter of the active cutting portion, while the *cutting length* denotes the useful axial extent of the cutting edges. Similarly, the *neck length* and *shank length* describe the axial extension of the neck and shank regions, and the *total length* represents the overall length of the tool. The term *cutter sweep* refers to the helical development of the flutes along the body, whereas the *center hole*, when present, identifies the central hole used for manufacturing or centring purposes. Although these quantities are not angular parameters, they define the dimensional and structural framework within which the local rake and clearance surfaces are generated and measured. Cutting-tool geometry should therefore be regarded as a three-dimensional system of surfaces, edges, and reference regions, rather than as a mere collection of nominal dimensions [1].

Within this framework, the most relevant aspect for both functional interpretation and metrological analysis is the local orientation of the active surfaces adjacent to the cutting edge. In particular, the rake angle γ describes the orientation of the rake face, the clearance angle α the separation of the flank face from the machined surface, and the wedge angle β the angular extent of the cutting wedge between these two surfaces. Although these definitions are straightforward in simplified orthogonal cutting models, their determination in real tools is considerably more complex because of helical edges, curved surfaces, fillets, and local microgeometry. A rigorous geometric framework is therefore required before addressing the measurement problem in detail.

2.1.1 Rake Angle and Local Tooth Geometry

The rake angle, denoted by γ, describes the orientation of the rake face, i.e., the surface along which the removed material flows during chip formation. It is one of the most influential geometric parameters of the cutting edge, since it affects chip-flow conditions, stress distribution near the tool–chip interface, cutting forces, and, more generally, the mechanical response of the cutting process.

In end mills, however, the rake angle cannot be interpreted as a purely two-dimensional quantity, because it is embedded in the local three-dimensional geometry of each tooth. This is evident in the representation of the tooth

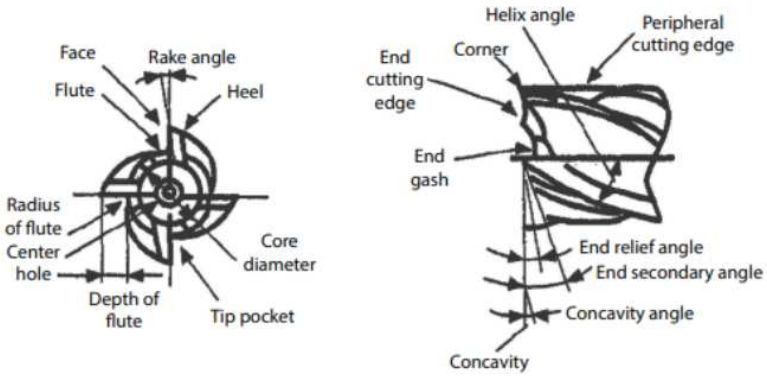

Figure 2.2: Geometric features of an end mill tooth. Adapted from [1].

geometry, where γ is shown together with other local features. The *face* identifies the rake face itself, namely the local surface along which the chip slides. The *flute* is the helical groove that provides the free volume required for chip accommodation and evacuation, and its geometry directly contributes to the shape of the rake region. The *heel* denotes the region immediately behind the rake face and contributes to the mechanical support of the tooth near the cutting edge. Other terms visible in the frontal view, such as *radius of flute* and *depth of flute*, describe the local size and shape of the flute, while the *core diameter* identifies the diameter of the central core of the tool, i.e., the solid inner portion that provides structural stiffness. The *tip pocket* denotes a local cavity near the tool tip, and the *center hole*, when present, identifies the central bore already mentioned in the overall tool geometry. Although these quantities do not directly define the rake angle, they shape to the actual configuration of the rake face [1].

The side view of the same tooth introduces additional terms that further clarify the three-dimensional geometry of the cutting region. The *peripheral cutting edge* is the cutting edge active along the cylindrical outer surface of the end mill, whereas the *end cutting edge* is active in the frontal region of the tool. The *corner* identifies the transition region between peripheral and end cutting edges and is often critical for local stress concentration. The *helix angle* describes the helical inclination of the tooth along the cutter body and plays an important role in gradual edge engagement and chip evacuation. The *end gash* is the terminal groove that contributes to the frontal cutting geometry and helps enable cutting action near the centre of the tool. The *end relief angle* and *end secondary angle* describe local relief

surfaces in the frontal region, while *concavity* and *concavity angle* refer to the local curved shape of the end face. Taken together, these features show that the rake angle is not an isolated line angle, but a local quantity embedded in a complex spatial geometry [1].

From a functional point of view, a positive rake generally promotes freer cutting action, facilitates chip formation, and may reduce cutting resistance. Conversely, a smaller or negative rake increases the mechanical support of the cutting wedge and may therefore be advantageous under more severe operating conditions. A neutral configuration represents an intermediate condition. In the present discussion, however, the emphasis is placed less on a detailed classification of positive, neutral, and negative rake configurations, and more on the fact that γ is a local geometric quantity whose interpretation depends on the selected position along the cutting edge and on the adopted reference system.

From a metrological perspective, this is particularly important. Because of the helical form of the cutter and the complexity of the local tooth geometry, the rake angle cannot always be represented satisfactorily by a single nominal value valid for the entire tool. Its measurement instead requires the rigorous identification of the local section under investigation and of the geometric reference according to which the angle is defined. An accurate determination of γ is essential, since even limited deviations from the intended geometry may modify chip-flow conditions, force distribution, and wear evolution, thereby affecting the actual cutting performance of the tool.

2.1.2 Clearance Angle and Flank Geometry

The clearance angle, denoted by α, describes the inclination of the flank face with respect to the newly machined surface. In machining literature, this quantity is also commonly referred to as the *relief angle*, because its primary function is to provide geometric separation between the tool body and the surface generated immediately behind the cutting edge. Whereas the rake angle mainly affects chip-flow conditions, the clearance angle primarily governs contact conditions at the flank face and is therefore closely related to rubbing, friction, and flank wear.

The local section shown in the figure makes it clear that flank geometry is

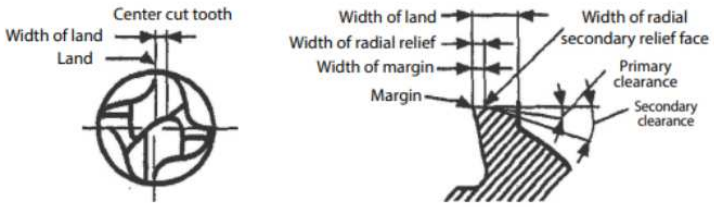

Figure 2.3: Local cross-sectional representation of an end mill tooth. Adapted from [1].

not simply represented by a single inclined plane. The *primary clearance* corresponds to the relief surface immediately adjacent to the cutting edge, i.e., the first surface ensuring separation from the machined workpiece. The *secondary clearance* is a subsequent relief surface located behind the primary one and contributes to the overall flank geometry and structural support of the tooth. The presence of both primary and secondary clearance shows that the real flank face is not described by a single ideal surface, but by a sequence of local surfaces designed to balance geometric separation and edge support.

Other terms shown in the same representation help define the local flank region more rigorously. The *land* is the narrow strip immediately adjacent to the cutting edge, often intentionally maintained to provide local support; the *width of land* is its width. The *margin* is a narrow peripheral strip that contributes to guiding and stabilising the tool, while the *width of margin* specifies its extent. The *width of radial relief* identifies the width of the primary radial relief region, whereas the *width of radial secondary relief* denotes the width of the secondary radial relief region. In the frontal cross-sectional view, the term *center cut tooth* indicates a tooth geometry designed to permit cutting action up to the centre of the tool, which is particularly relevant in operations involving axial penetration. Altogether, these terms show that the clearance angle is associated with a local geometric region composed of surfaces and strips, rather than with a single abstract line angle.

If the value of α is too small, the flank face tends to interfere with the machined surface, increasing friction, promoting rubbing and ploughing phenomena, and accelerating flank wear. Conversely, if the clearance angle is too large, the amount of material supporting the cutting edge is reduced,

and the local strength of the tooth may become insufficient. The selection of α must therefore be interpreted as a compromise between two opposite requirements: ensuring adequate geometric separation from the workpiece and preserving sufficient mechanical support behind the cutting edge [1].

This issue is particularly important in rotary tools, where the local value of the clearance angle may vary with the selected section, the helical development of the tooth, and the actual three-dimensional morphology of the cutter. As a consequence, the measurement of α cannot be reduced to a simple evaluation on a projected profile, but requires correct identification of the local flank region and a consistent geometric reference system. From a metrological point of view, the clearance angle is therefore a key parameter for linking the real geometry of the tool to contact behaviour, wear evolution, and the dimensional and surface quality of the machined component.

2.1.3 Wedge Angle and Cutting Edge Structure

The wedge angle, denoted by β, represents the angular extent of the cutting wedge included between the rake face and the flank face. From a geometric point of view, it expresses the local resistant mass of the cutting edge and can therefore be regarded as a synthetic descriptor of the balance between sharpness and mechanical robustness [1].

In the simplified orthogonal cutting model, the rake angle γ, the clearance angle α, and the wedge angle β are related by:

$$\alpha + \beta + \gamma = 90^\circ$$

from which it follows that:

$$\beta = 90^\circ - (\alpha + \gamma).$$

This relationship shows that the wedge angle cannot be considered an independent quantity, since it directly depends on the geometric balance between rake and clearance. If either γ or α increases, the value of β decreases; conversely, a larger wedge angle reduces the geometric space available for rake and clearance. From a functional perspective, a small value of β corresponds to a sharper and potentially more penetrating cutting edge, but

also to lower structural robustness. A larger wedge angle, on the other hand, provides greater support to the cutting edge, often at the expense of penetration capability and with a possible increase in cutting resistance.

In real tools, and especially in end mills, the wedge angle must also be regarded as a local quantity. Its value depends on the tooth section considered, on the position along the helix, and on the actual morphology of the cutting region. From a metrological perspective, its evaluation therefore requires the same care as the measurement of γ and α: the local reference section must be clearly identified, and the adopted geometric system must be consistent with the intended angular definition. In this sense, β can be interpreted as a compact descriptor of the local cutting-edge configuration and of the trade-off between cutting capability and mechanical integrity.

2.2 Measurement Challenges

The definitions introduced in the previous sections provide a rigorous framework for describing rake angle, clearance angle, and wedge angle within idealised orthogonal cutting models. Their determination on real cutting tools, however, is considerably more complex. The difficulty lies not only in observing the tool profile, but in describing the local morphology of the functional surfaces near the cutting edge in a geometrically and metrologically consistent way.

A first challenge is geometric. In real tools, especially rotary tools such as milling cutters and drills, the active surfaces cannot usually be reduced to a simple planar configuration. The cutting edge often follows a helical or curved path, the rake and flank faces may vary locally, and the cutting-edge microgeometry introduces further deviations from the ideal model. As a result, rake and clearance angles cannot be treated as unique global quantities, but must be defined with respect to a specific local section and reference system. The measurement therefore depends not only on acquisition quality, but also on the correct definition of the evaluation plane and of the functionally relevant region.

A second challenge is optical. The most relevant regions are typically located close to the cutting edge, where dimensions are small, curvature is

high, and partial occlusions may occur. In addition, cutting tools are generally metallic and highly reflective, which can cause saturation, specular reflections, and local signal loss. This is critical because the measurement requires not only detecting the edge, but also reliably acquiring the orientation of the adjacent surfaces, from which the functional angles are derived.

A third challenge is metrological. Reliable evaluation of these parameters requires not only visibility of the region of interest, but also a coherent and repeatable reference framework consistent with the required accuracy. Observing a feature does not automatically mean measuring it. Limited uncertainties in cutting-edge localisation, section orientation, or acquisition stability may produce significant errors when micrometric surfaces and tight tolerances are involved.

For these reasons, the challenge is not simply to "see" the tool, but to reconstruct its local three-dimensional morphology reliably in the regions of greatest functional interest. This also explains the limitations of two-dimensional optical systems: while effective for projected profiles and macroscopic dimensions, they are less suitable when the objective is the spatial characterisation of functional surfaces. This motivates the use of three-dimensional acquisition technologies, discussed in the following sections as possible extensions of the industrial presetting paradigm currently adopted in practice.

2.3 2D Optical Presetting Systems

As discussed in the previous sections, the correct quantification of cutting-edge geometry is essential for reliable tool performance. To frame the related metrological challenges, it is therefore useful to examine the presetting technologies currently adopted in industrial practice. In this work, the main industrial reference is provided by the measurement and presetting systems developed by Speroni S.p.A., and in particular by the STP FUTURA machinery, which represents a significant example of the current state of the art in optical presetting architectures [5].

From a mechanical and kinematic perspective, these systems are designed to provide stable and repeatable measurement conditions. Structural rigidity, accurate axis control, and precise spindle positioning reduce the influence

of vibrations, positioning errors, and environmental disturbances typical of the shop-floor setting. The reliability of the optical measurement therefore depends not only on the camera or image-processing algorithms, but on the overall mechanical and control architecture supporting the acquisition.

From the optical point of view, the measurement principle is essentially two-dimensional. In a typical configuration, the tool is observed through a frontal vision system combined with precision optics and dedicated illumination to enhance profile visibility. The software then extracts the projected contour of the tool and analyzes it through image-processing and edge-detection algorithms to derive the quantities of interest. Measurement is thus based on the accurate analysis of the projected representation of the tool on the image plane, rather than on a volumetric reconstruction of its surface.

Figure 2.4: Example of a two-dimensional acquisition interface of the Speroni STP FUTURA system during the presetting of a cutting tool.

Figure 2.4 shows an example of a two-dimensional acquisition screen from the STP FUTURA system. The operator interface provides a real-time view of the tool, with graphical references, dimensional annotations, and measurement aids superimposed. This clearly illustrates the physical principle of industrial presetting: what the system measures with high accuracy is primarily the apparent silhouette or projected profile of the tool. From this

representation, several macroscopic quantities of practical interest can be derived. In this respect, current 2D presetting machines achieve very high levels of accuracy, precision, and repeatability, and are fully adequate for a wide range of industrial dimensional inspections.

The value of these systems lies in the integration of mechanics, optics, motion control, and software processing within a stable, rapid, and production-oriented measurement chain. Their limitations should therefore not be interpreted as a lack of technological maturity. On the contrary, two-dimensional optical presetting is the dominant industrial paradigm and performs very effectively within the measurement domain for which it was conceived.

This framework is not specific to a single manufacturer. Major competitors such as ZOLLER [6] and HAIMER [7] offer systems based on the same principle: two-dimensional optical acquisition of the tool profile, extraction of measurable features through image processing, automation of the inspection sequence, and direct transfer of tool data to the CNC machine. Differences among manufacturers mainly concern automation level, software interface, additional functions, connectivity, and integration with tool management environments, rather than the underlying measurement principle. This confirms that the 2D approach has reached a high degree of industrial sophistication and remains the established standard for presetting and dimensional verification of cutting tools.

For this reason, two-dimensional optical presetting should not be regarded as an outdated solution, but as a mature and highly effective metrological framework for a broad class of industrial applications. It is particularly well suited to the measurement of external diameters, axial lengths, profile positions, and other macroscopic features that can be identified on the projected silhouette of the tool.

However, when the analysis moves from projected macroscopic geometry to the microgeometry of the cutting wedge, the intrinsic limits of planar optical measurement become evident. A 2D image is, by definition, the projection of a three-dimensional object onto the camera focal plane. This entails a loss of depth information, since points that are distinct in space but aligned along the same line of sight collapse into the same image position. As a result, geometrically different surfaces may become indistinguishable

in the planar representation, especially when they remain enclosed within the overall dark envelope of the tool.

This becomes particularly critical for the characterization of rake angle and clearance angle. These parameters depend not only on the external contour of the tool, but on the real spatial orientation of the rake face and flank face near the cutting edge. In a conventional two-dimensional acquisition, these surfaces are not observed in their actual three-dimensional configuration, but remain embedded in the apparent profile of the tool. Consequently, even with excellent image quality and highly accurate edge-detection algorithms, the depth information required for their measurement is not difficult to recover: it is physically absent.

The current industrial landscape is instructive in this respect. While leading presetting manufacturers have refined the 2D approach through structural stability, precision optics, advanced image processing, automation, and digital connectivity, the growing need to describe the three-dimensional morphology of the cutting edge has motivated the development of complementary solutions based on volumetric acquisition and 3D topographical inspection [8].

Accordingly, the research developed in this thesis should not be interpreted as an attempt to replace current 2D presetting architectures, but rather as their natural extension. Since industrial systems already provide a mature and reliable platform for the inspection of projected geometry, the next step is to assess whether these architectures can be enhanced through the integration of three-dimensional acquisition techniques. The move toward 3D is therefore motivated not by a weakness of 2D presetting, but by the need to access geometric information that planar projection cannot provide.

2.4 3D Optical Acquisition Technologies

As discussed in the previous section, the main limitation of two-dimensional optical presetting is the absence of depth information. The observed geometry corresponds to the projection of the tool profile onto the image plane rather than to the actual three-dimensional morphology of the functional surfaces near the cutting edge. Overcoming this limitation requires 3D ac-

quisition systems capable of assigning a spatial coordinate to each observed point and thus providing a more complete description of the local tool topography.

In general, three-dimensional measurement methods can be divided into **contact** and **non-contact** techniques. Contact methods rely on direct mechanical interaction with the surface and are suitable for many conventional dimensional applications, such as Coordinate Measuring Machines (CMMs). However, they are often unsuitable for the rapid and non-destructive characterization of micrometric cutting edges and delicate functional surfaces. Non-contact techniques, by contrast, retrieve geometric information without physical interaction and are therefore better suited to cutting-tool metrology.

Within non-contact methods, a further distinction can be made between **optical** and **non-optical** approaches. While non-optical techniques are based on acoustic or electromagnetic principles, optical techniques exploit the propagation and interaction of light with the observed surface. This work focuses exclusively on optical methods, since they offer the non-invasiveness, speed, and resolution required to acquire small metallic surfaces with micrometric precision.

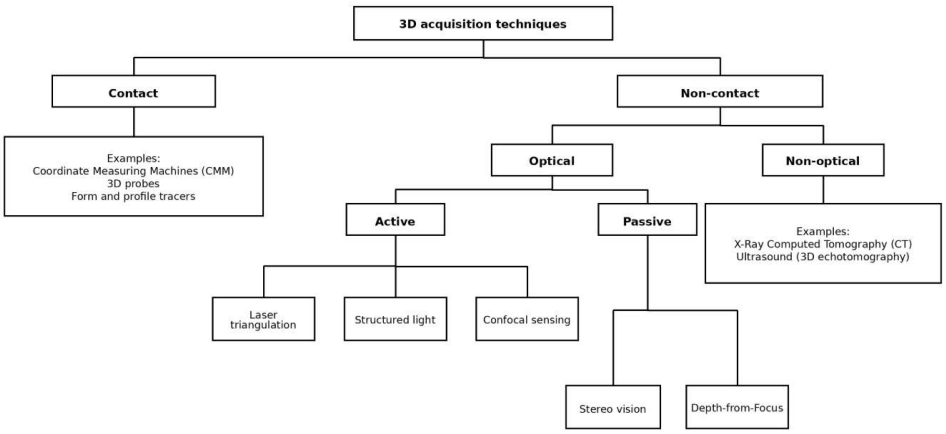

Figure 2.5: Classification of 3D acquisition technologies.

Within the optical domain, the distinction between **active** and **passive** techniques becomes fundamental, as shown in Figure 2.5.

- **Active techniques** project a controlled light signal, such as a laser line, a structured-light pattern, or modulated illumination, and derive

depth from its response on the surface. *Laser Triangulation*, *Structured Light*, and *Confocal Sensing* belong to this category.

- **Passive techniques** estimate depth from images acquired under ambient or diffused light, using principles such as disparity in *Stereo Vision* or focus analysis in *Depth-From-Focus*.

This classification provides a systematic framework for the technologies discussed in the following sections. In the case of cutting tools, the choice depends not only on shape reconstruction capability, but also on robustness against specular metallic surfaces, occlusion management, and ease of industrial integration. The following paragraphs review the key technologies and guide the selection for industrial application.

2.4.1 Laser Triangulation

Laser triangulation is an active, non-contact optical measurement technique that determines the spatial position of a point on an object's surface by exploiting known geometrical and trigonometrical relationships. The measurement system generally consists of two main components placed at a fixed distance, referred to as the *baseline* (d): a coherent light source, usually a laser diode, and an optical receiver, typically a camera equipped with a high-resolution CMOS or CCD sensor.

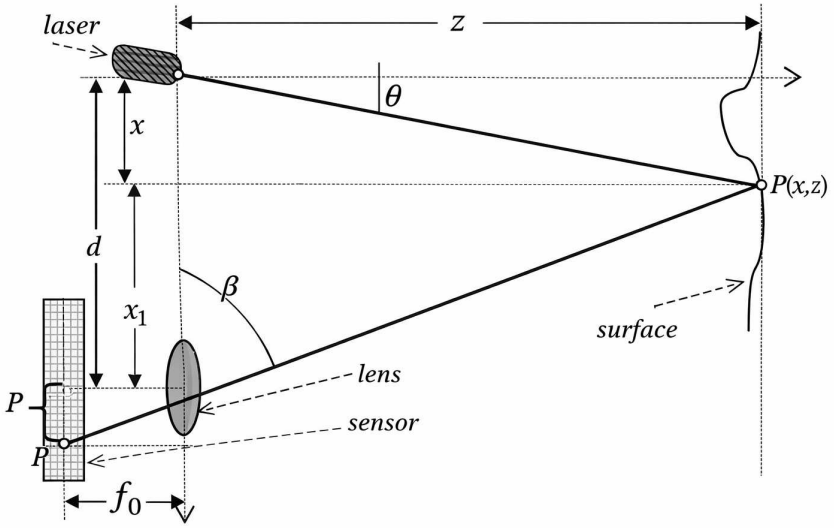

Figure 2.6: Geometrical scheme of the *Laser Triangulation* principle.

The operating principle is based on the fact that the laser emitter and the camera observe the same point on the surface from two different viewpoints. As illustrated in Fig. 2.6, depth reconstruction is therefore obtained through triangulation rather than by direct time-of-flight measurement [9]. In the simplified two-dimensional model, the baseline d is known, the angle θ defines the direction of the emitted laser beam, and the angle β describes the observation direction associated with the receiving optics. Under this configuration, the depth coordinate z can be expressed as

$$d = z \tan\theta + z \cot\beta \tag{2.1}$$

from which it follows that

$$z = \frac{d}{\tan\theta + \cot\beta}. \tag{2.2}$$

This relation shows that, once the baseline and angular configuration are known, the position of the illuminated point can be reconstructed through elementary trigonometric relations [9].

In practical systems, however, reconstruction is based on the position of the laser signal in the image acquired by the camera. When the laser beam strikes the surface, the reflected or diffusely scattered light is collected by the receiving optics, and local height variations produce a displacement of the observed laser trace on the sensor. Depth is therefore inferred from the image position of the optical signal through calibration, which links image measurements to the three-dimensional coordinates of the observed points. Accurate reconstruction thus depends on camera calibration, laser-plane geometry, and the relative alignment of the optical components.

In industrial systems, the method is typically extended from a single point to a projected laser line, in the so-called *sheet-of-light* or *light-blade* configuration. In this case, depth is computed simultaneously for all points along the line, so that each acquisition returns the three-dimensional profile of an entire cross-section. By introducing relative motion between the sensor and the object, adjacent profiles can then be combined into a dense point cloud or a complete surface reconstruction [10]. This is particularly relevant for cutting tools, since it enables rapid acquisition of local profiles of the cutting edge and adjacent functional surfaces.

From a metrological perspective, laser triangulation offers several advantages. As an active technique, it does not depend strictly on the natural texture of the object, since the optical reference is projected by the system itself. It is also appreciated for its favourable balance between acquisition speed, implementation simplicity, and measurement sensitivity, while modern industrial profilers can achieve high profile rates and dense local sampling. These characteristics make laser triangulation especially attractive when the objective is the reconstruction of the true three-dimensional morphology of functionally critical regions.

At the same time, the technique presents important geometric and optical limitations. A first issue is related to occlusion and *shadowing*: because the emitter and the camera observe the scene from different directions, some regions may be illuminated but not visible, or visible but not reached by the projected laser line. This is particularly critical in the presence of grooves, undercuts, sharp edges, and helical geometries, which are common in cutting tools [10]. In some cases, these limitations can be reduced through multi-view or multi-sensor configurations [11].

A further limitation concerns the optical behaviour of metallic surfaces. Cutting tools made of cemented carbide or ground steel often exhibit highly reflective finishes, which may cause local sensor saturation or a severe reduction of the usable return signal. In addition, coherent illumination gives rise to *speckle* noise, which can degrade laser-line localisation and reduce final measurement accuracy [10].

Finally, the quality of the three-dimensional reconstruction depends not only on the optical head, but on the entire opto-mechanical measurement chain. Complete reconstruction is generally obtained through controlled motion of the sensor or the object, so positioning uncertainty, structural vibration, straightness errors, or synchronisation issues directly affect the final dataset [12]. The overall metrological performance is therefore determined by the combined effect of sensor resolution, calibration quality, and the kinematic accuracy of the scanning system.

In light of these considerations, laser triangulation can be regarded as a particularly promising technology for the application considered in this work, since it provides access to the real three-dimensional morphology of the func-

tional surfaces near the cutting edge, overcoming the intrinsic limitation of two-dimensional systems based only on projected profiles. Its effectiveness, however, remains strongly dependent on tool geometry, surface optical properties, and the overall performance of the integrated sensor-machine system [11].

Reference Industrial Solution

A practical industrial benchmark for laser triangulation can be obtained by examining the solutions currently available within the technological framework of the present work. In particular, a selection of commercial laser line profilers from the three main suppliers accessible through iMAGE S, namely LMI Technologies, Teledyne, and AT Sensor, was considered [13, 14, 15]. The purpose of this comparison is not to repeat the sheet-of-light principle discussed above, but rather to show how the expected advantages of laser triangulation are reflected in the specifications of real industrial devices. In order to preserve readability and avoid oversized tables, only a subset of representative models was retained for each supplier.

LMI Technologies				
Technical Parameter	**2420**	**2520**	**2618**	**6310**
Linearity Z [± % of MR]	0.006	0.006	0.015	0.016
Resolution X [μm]	14.0–16.5	13.0–17.0	5.0–5.4	< 2.1
Repeatability Z [μm]	0.4	0.4	0.38	0.15
Field of View [mm]	27.0–32.0	25.0–32.5 (diffuse)	20.0–23.0	13.4–14.5
Clearance Distance [mm]	60.0	47.5	44.5	18.15
Measurement Range [mm]	25.0	25.0	12.0	5.5

Table 2.1: Representative technical specifications of selected LMI Gocator laser line sensors considered in this work.

The selected LMI models show the internal flexibility of the Gocator laser line family, spanning from configurations with wider operating geometry to sensors characterised by finer lateral sampling and more favourable repeatability values. This confirms the broad industrial adaptability of laser triangulation within a single supplier portfolio.

Among the other commercial solutions available in the same industrial framework, the Teledyne Z-Trak family provides a more compact and geometrically regular set of configurations, which is useful for assessing more standardised operating conditions.

Teledyne			
Technical Parameter	**S2K-0004-B3**	**V2K-0015-B3**	**LP2C-4K-0004-B3**
Resolution X [μm]	7.46	15.96	3.45
Repeatability Z [μm]	0.30	0.50	0.30
Field of View [mm]	15.2	32.0	14.15
Clearance Distance [mm]	33.15	32.7	33.15
Measurement Range [mm]	4.0	15.0	4.0

Table 2.2: Representative technical specifications of selected Teledyne Z-Trak laser line sensors considered in this work.

The Teledyne models highlight a more regular measurement layout, with limited variation in clearance distance and a compact operating domain. This makes them particularly useful for evaluating laser triangulation under more controlled and standardised geometric conditions.

A further perspective is provided by AT Sensor, whose product range extends toward larger stand-off distances and broader measurable regions, thereby enlarging the range of potential integration scenarios.

AT Sensor			
Technical Parameter	**ECS 2040-23-100**	**Model G6**	**XCS 3070**
Resolution X [μm]	49.0	5.0–26.0	16.0
Resolution Z [μm]	1.9	0.2–1.2	0.5
Field of View [mm]	102.0	7.0–53.0	48.0
Clearance Distance [mm]	106.0	31.0–90.0	146.0
Measurement Range [mm]	60.0	5.0–46.0	20.0

Table 2.3: Representative technical specifications of selected AT Sensor laser line sensors considered in this work.

The selected AT Sensor models cover a wider geometric domain, extending toward larger fields of view and stand-off distances. This broadens the

comparison and shows how laser triangulation may also be configured for less compact but more spatially extended inspection layouts.

Taken together, the three sets of specifications confirm that laser triangulation is currently available in a wide variety of industrial configurations, ranging from compact high-resolution profilers to systems designed for larger stand-off distances and wider measurable regions. From the point of view of the present application, these data support the view that laser triangulation offers a particularly favourable balance between metrological sensitivity, compact optical geometry, and practical integrability.

It should nevertheless be noted that the datasheets are not fully homogeneous in the way Z-axis performance is expressed. In particular, LMI and Teledyne report repeatability-related quantities, whereas AT Sensor reports Z resolution. For this reason, the comparison should not be interpreted as a strict one-to-one ranking of absolute performance, but rather as an application-oriented overview of the current commercial solutions available within the industrial framework of the project.

Overall, the analysed commercial solutions reinforce the role of laser triangulation as one of the most credible candidates for the present work. Its main industrial advantage lies not only in the high local sensitivity that can be achieved, but also in the fact that this sensitivity is combined with operating geometries compatible with controlled profile-by-profile scanning. The final suitability of each sensor family, however, must still be assessed by considering the actual optical response of cutting-tool surfaces, the integration constraints of the measurement platform, and the consistency between nominal sensor specifications and the metrological requirements of the application.

2.4.2 Structured Light

Structured light is an active, non-contact optical measurement technique in which the three-dimensional geometry of an object is reconstructed by projecting a known light pattern onto its surface and observing its deformation from a different viewpoint. In the most common configuration, the system consists of a digital projector and one or more cameras arranged in a fixed geometry. Unlike laser triangulation, where the projected feature is

typically a point or a line, structured light illuminates a wider portion of the field of view with a spatially coded pattern, enabling the simultaneous reconstruction of a dense set of surface points.

The operating principle can be interpreted as a triangulation problem between a camera pixel and the corresponding projector pixel. The projector emits a known pattern onto the object surface, such as stripes, sinusoidal fringes, grids, or other coded structures. Since the surface is generally non-planar, the pattern appears geometrically deformed in the image acquired by the camera. Once the correspondence between an observed image point and the projected pattern has been established, the three-dimensional coordinates of the surface point can be reconstructed by triangulation, provided that the intrinsic parameters of the camera and projector, as well as their relative pose, are known [16].

From a geometric point of view, the projector can be modelled as an inverse camera. Each illuminated point observed by the camera is associated with a viewing ray originating from the camera and a projection ray originating from the projector. After calibration, the three-dimensional surface point is determined by the intersection, or best approximate intersection, of these two rays.

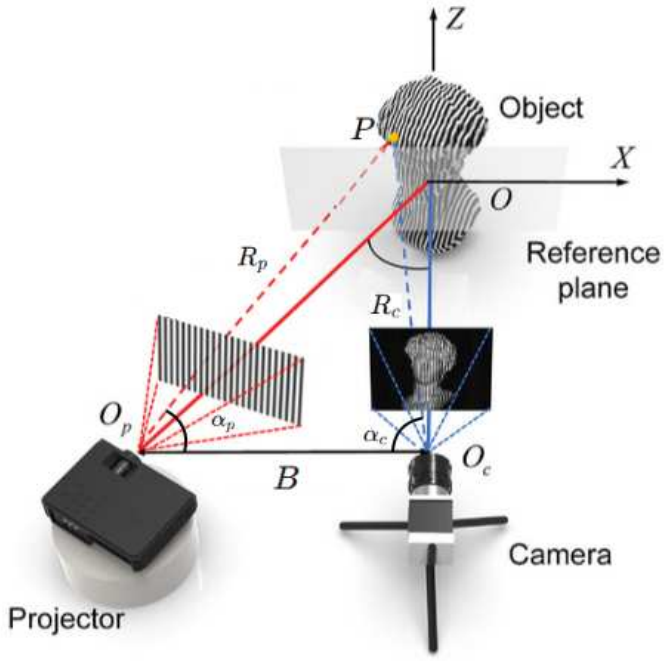

Figure 2.7: Simplified geometrical scheme of the *Structured-Light.*

Figure 2.7 makes it possible to state explicitly the geometrical criterion underlying the reconstruction. Considering the planar section defined by the projector optical centre O_p, the camera optical centre O_c, and the reconstructed surface point P, one obtains the triangle O_pO_cP, in which the distance between projector and camera defines the baseline $B = \overline{O_pO_c}$. The point P is identified by two known directions: the projection ray O_pP, forming an angle α_p with the baseline, and the observation ray O_cP, forming an angle α_c with the same baseline. Denoting by $R_p = \overline{O_pP}$ and $R_c = \overline{O_cP}$ the distances of the point from the two optical centres, the point position can be obtained by applying the law of sines to the triangle [16].

Since the angle at the vertex P is equal to $180° - (\alpha_p + \alpha_c)$, the law of sines yields

$$\frac{R_c}{\sin \alpha_p} = \frac{R_p}{\sin \alpha_c} = \frac{B}{\sin[180° - (\alpha_p + \alpha_c)]}.$$

By exploiting the trigonometric identity $\sin(180° - x) = \sin x$, the previous relation can be rewritten as

$$R_c = B \, \frac{\sin \alpha_p}{\sin(\alpha_p + \alpha_c)}$$

and, similarly,

$$R_p = B \, \frac{\sin \alpha_c}{\sin(\alpha_p + \alpha_c)}.$$

These expressions show that, once the baseline and the two optical directions are known, the spatial position of the point can be reconstructed geometrically. In particular, R_c and R_p represent distances measured along the viewing and projection rays, from which the actual three-dimensional coordinates can subsequently be derived.

In real systems, however, the angles α_p and α_c are generally not measured explicitly, but result from system calibration and correct decoding of the observed pattern. A central issue is therefore not only triangulation, but also the retrieval of reliable correspondences between the observed image and the projected pattern. For this reason, the pattern is usually encoded so that each observed region can be identified unambiguously. Common

strategies include binary and Gray-code patterns, in which a sequence of projected images progressively labels projector columns or rows, and phase-shifting techniques, in which sinusoidal fringes are projected with controlled phase offsets to estimate depth with sub-pixel precision [17]. Gray-code approaches are generally appreciated for their robustness and unambiguous decoding, whereas phase-shifting methods are attractive when high spatial resolution and local accuracy are required [18]. Hybrid strategies combining absolute coding and phase information are also common.

This highlights one of the main differences with respect to laser triangulation. In laser triangulation, the measurement problem is essentially reduced to the localisation of a projected point or line on the sensor. In structured light, by contrast, the system must also determine which element of the projected pattern corresponds to each position in the observed image. Measurement performance therefore depends not only on triangulation geometry, but also on the adopted coding strategy, the robustness of the decoding algorithm, the radiometric response of the surface, and the synchronisation between projection and acquisition.

From a metrological point of view, structured light offers several advantages. It enables dense areal acquisition, since an entire portion of the visible surface can be reconstructed in a limited number of projected frames rather than by scanning a single point or line at a time. This makes the technique attractive when the objective is to obtain a global description of the local topography of the cutting edge and adjacent functional surfaces. In addition, coded patterns improve the observability of surfaces with insufficient natural texture, while modern digital projection systems allow the pattern type, spatial frequency, and temporal coding strategy to be adapted to the required trade-off between speed, density, and robustness.

At the same time, structured light presents important limitations. Since the technique relies on the faithful observation of a projected intensity pattern, highly reflective metallic surfaces may generate specular reflections, local saturation, blooming, or severe radiometric distortions, thereby compromising pattern decoding [19]. This is particularly relevant for cutting tools, whose ground or coated surfaces often exhibit directional reflectance and abrupt local variations near the cutting edge. In addition, steep slopes,

grooves, undercuts, and helical geometries may produce shadowing and occlusion effects, preventing some regions from being illuminated or observed reliably by the camera [16].

A further limitation concerns acquisition dynamics. Many of the most accurate structured-light approaches are multi-shot techniques, meaning that several patterns must be projected sequentially to recover the full code or phase information. Under these conditions, both the object and the sensor must remain stable throughout the sequence; otherwise, motion between successive frames introduces correspondence errors and reconstruction artefacts. Single-shot methods reduce this constraint and are more suitable for dynamic scenes, but generally at the expense of robustness, spatial discrimination, or sensitivity to surface colour and reflectance variations.

Finally, reconstruction quality depends strongly on calibration. Accurate three-dimensional measurement requires precise knowledge of camera and projector intrinsic parameters, optical distortions, and the extrinsic geometry of the projector–camera system. The projector must therefore be treated not simply as an illumination device, but as an active imaging component. The overall metrological performance thus results from the combination of triangulation accuracy, pattern decoding quality, radiometric control, and opto-mechanical stability [20].

In light of these considerations, structured light can be regarded as a promising technology for the dimensional inspection of cutting tools, since it combines dense three-dimensional acquisition, potentially high accuracy, and relatively short measurement times over the observable field of view [16]. Its actual suitability, however, depends on the ability of the system to cope with specular metallic surfaces, local occlusions, and the calibration complexity associated with projector–camera integration.

Industrial Reference Solution

In order to complement the theoretical discussion with a more application-oriented perspective, it is also useful to consider some of the structured-light sensors currently adopted in industrial environments. In the present work, the reference to specific commercial solutions arises from the actual experimental framework and from the technological context in which the

activity was carried out. For this reason, the devices reported below are introduced as representative industrial reference cases, useful to show how the general characteristics of structured-light technology are translated into real specifications and practical measurement trade-offs.

Within this perspective, the Gocator Snapshot series by LMI Technologies was considered as a meaningful example of commercially available area-based structured-light sensors [13]. The purpose of this reference is not to identify a universally optimal solution, but rather to frame the current level reached by this class of systems in terms of field of view, achievable resolution, and nominal accuracy under realistic industrial constraints.

LMI Technologies			
Technical Parameter	**Model 3210**	**Model 3506**	**Model 3520**
Resolution XY [μm]	60.0 to 90.0	20.0 to 25.0	74.0 to 121.0
VDI/VDE Accuracy [μm]	35.0	12.0	90.0 to 200.0
Field of View [mm]	71.0 × 98.0 to 100.0 × 154.0	27.0 × 45.0 to 30.0 × 45.0	179.0 × 115.0 to 282.0 × 175.0
Clearance distance [mm]	165.0	87.0	203.0
Measurement range [mm]	110.0	25.0	150.0

Table 2.4: Representative technical specifications of the LMI Gocator Snapshot structured-light sensors considered in this work.

The specifications reported in Table 2.4 clearly highlight the internal trade-off that characterises the analysed structured-light family. Model 3506 provides the most favourable values in terms of lateral resolution and nominal VDI/VDE accuracy, although within a relatively limited field of view and measurement range. On the other hand, Model 3520 covers a significantly larger observable area and a wider measurement range, at the cost of a coarser spatial sampling and lower nominal depth performance. Model 3210 can be regarded as an intermediate configuration between these two design choices.

From the point of view of the present application, these data confirm that the main strength of snapshot structured-light sensors lies in their ability to acquire relatively large surface portions in a limited number of acquisitions.

This aspect is particularly relevant when the objective is to obtain a rapid three-dimensional overview of the tool geometry or to reduce the overall inspection time.

At the same time, the reported specifications also suggest that the advantage in areal coverage is generally associated with a lower local metrological sensitivity, especially when compared with solutions specifically oriented toward high-resolution profile acquisition or micro-scale surface reconstruction. Consequently, although these industrial reference systems effectively illustrate the current capabilities of structured-light technology, their suitability for the present task must still be assessed with respect to the required level of geometric detail, especially in the cutting-edge region and in the adjacent functional surfaces.

2.4.3 Stereo Vision

Stereo vision is a passive, non-contact optical measurement technique that reconstructs the three-dimensional geometry of a scene from two images acquired from different viewpoints [21]. In its simplest configuration, the system consists of two cameras rigidly mounted at a known distance from each other, denoted by b, which defines the stereo baseline. Unlike active techniques such as laser triangulation or structured light, stereo vision does not project a controlled optical signal onto the object, but infers depth from the geometric differences between the two acquired views.

The operating principle is based on the fact that the same spatial point, shown in Figure 2.8, is projected onto different positions on the two image planes. Depth is then recovered by triangulating the two optical rays originating from the camera centres and intersecting at the observed point.

Figure 2.8 illustrates a rectified stereo configuration, convenient for explaining the mathematical basis of the technique. In this arrangement, the two cameras have parallel optical axes and the same focal length f. The point P is described in the coordinate system of the left camera by the coordinates (x^c, z^c), while its projections onto the two image planes are denoted by u_1 and u_2. The distance between the two camera centres is the baseline b [2].

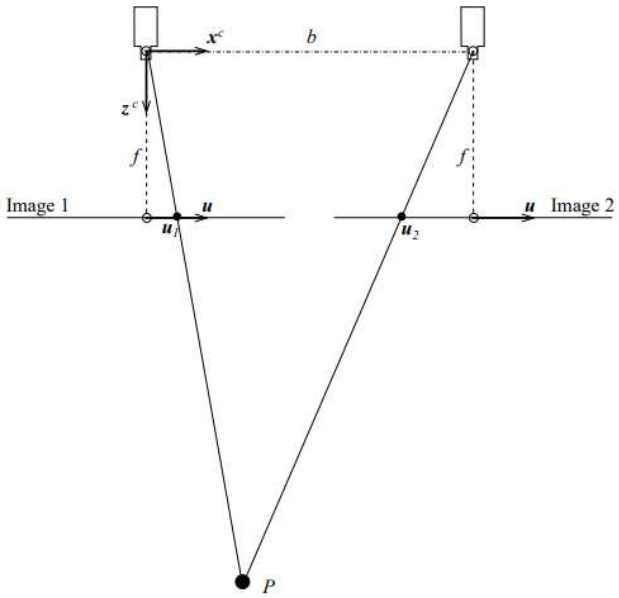

Figure 2.8: Simplified geometrical scheme of a rectified *Stereo Vision* system. Adapted from [2].

From the pinhole camera model, the projection equations are

$$u_1 = f\frac{x^c}{z^c}$$

for the left camera, and

$$u_2 = f\frac{x^c - b}{z^c}$$

for the right camera.

The difference between the two image coordinates defines the stereo disparity:

$$d = u_1 - u_2.$$

By substituting the previous expressions, one obtains

$$d = f\frac{b}{z^c},$$

from which the depth of the point in the reference frame of the left camera follows:

$$z^c = \frac{fb}{d}.$$

This is the fundamental result of stereo vision: depth is inversely proportional to disparity [2]. Once z^c has been estimated, the lateral coordinate can also be recovered:

$$x^c = \frac{u_1 z^c}{f} = \frac{u_1 b}{d}.$$

The point P can therefore be localised in space from the system baseline, camera focal length, and the positional difference between the two projections. Although the same reasoning can be extended to the vertical coordinate in the full three-dimensional case, the two-dimensional scheme in Figure 2.8 is sufficient to illustrate the reconstruction mechanism [21].

Although triangulation is the geometric core of the method, the main difficulty of stereo vision lies in the reliable identification of corresponding points in the two images. In order to apply the previous relations, it is necessary to determine which point in the first image corresponds to the same physical point in the second. In a rectified stereo configuration, this problem is simplified because corresponding points lie on the same image row; nevertheless, correspondence search remains the most critical stage of the pipeline.

From this point of view, stereo vision differs conceptually from structured light. In structured light, the information needed to distinguish surface points is actively introduced by the system through a known projected pattern. In stereo vision, by contrast, this information must be recovered passively from the natural texture or radiometric features of the scene. As a result, reconstruction quality depends strongly on the presence of sufficiently distinctive visual details and on the robustness of the matching algorithm [22].

From a metrological perspective, stereo vision offers several advantages. Being a passive technique, it does not require projectors or dedicated structured illumination. Moreover, the scene can be acquired simultaneously by the two cameras, making dense areal reconstruction possible without point-by-point or line-by-line scanning. The hardware architecture is also relatively simple, since the system essentially requires two calibrated cameras and a mechanically stable support preserving their relative pose.

At the same time, stereo vision presents important limitations. A first critical issue is its dependence on surface texture. If the observed scene contains uniform, low-contrast, or poorly textured regions, correspondence search may become ambiguous and generate local errors in the depth map. This is particularly relevant for cutting tools, which often exhibit polished, coated, or highly reflective metallic surfaces with limited natural texture

and pronounced specular effects.

A second issue concerns occlusions. Since the two cameras observe the scene from different viewpoints, some regions may be visible in one view but not in the other. In such cases, a physical correspondence is not available and depth reconstruction becomes incomplete or uncertain. This problem is especially significant in the presence of complex geometries, sharp edges, grooves, undercuts, and strongly inclined surfaces, all of which may occur in the microgeometry of cutting tools.

A further limitation is the sensitivity of depth to disparity estimation errors. From the relation

$$z^c = \frac{fb}{d},$$

it follows that small errors in d produce increasingly large depth errors as disparity decreases. In practice, depth resolution degrades with increasing distance from the cameras and depends directly on the baseline, the focal length, and the sub-pixel precision of disparity estimation.

Finally, calibration plays an essential role. Reliable three-dimensional reconstruction requires precise knowledge of the intrinsic parameters of both cameras, optical distortions, the relative pose between the sensors, and the effective baseline of the system. Calibration errors, mechanical misalignments, or structural instabilities directly affect rectification quality, correspondence consistency, and final reconstruction accuracy [2]. In an industrial context, stereo performance therefore depends not only on the matching algorithm, but on the entire opto-mechanical chain supporting the acquisition.

In light of these considerations, stereo vision is theoretically attractive for three-dimensional reconstruction, since it provides depth information without active illumination and with a relatively simple hardware configuration. Its actual suitability for cutting-tool inspection, however, depends strongly on its ability to handle poorly textured, reflective, and geometrically complex surfaces, as well as on the robustness of matching and the quality of system calibration.

Reference Industrial Solution

The current industrial landscape of stereo vision also provides a useful reference for relating the theoretical properties of the method to commercially

available systems. In this case, a selection of commercial models from the Ensenso family by IDS was considered as a representative example of industrial stereo sensors [23]. The objective of this comparison is to examine how the main geometric and metrological characteristics of stereo vision are expressed in the specifications of real systems.

IDS Sensor				
Technical Parameter	**B57 4**	**C57 S**	**C57 M**	**X36 5CP**
Z Accuracy [mm]	0.1 at 300.0	0.1 at 975.0	0.2 at 1850.0	0.3 at 1700.0
Focus distance [mm]	350.0	975.0	1850.0	1700.0
Focal length [mm]	4.0	4.0	4.0	8.0
Working distance [mm]	210.0 to 2000.0	500.0 to 5000.0	650.0 to 5000.0	1700.0
Measurement range [mm]	1047.0 to 1573.0	991.0 to 1495.0	1304.0 to 1807.0	1363.0 to 1865.0

Table 2.5: Representative technical specifications of the IDS Ensenso stereo sensors considered in this work.

The specifications reported in Table 2.5 show that the analysed stereo sensors are designed to operate over working distances and measurement volumes that are considerably larger than those typically associated with local micrometric inspection tasks. In particular, the most favourable nominal Z accuracy values are achieved only under specific focus conditions, while the corresponding sensing distances remain in the order of hundreds or thousands of millimetres. This clearly indicates that the main strength of these systems lies in the three-dimensional observation of relatively extended scenes rather than in extremely fine local metrology.

From a comparative point of view, models such as B57 4 provide the best nominal depth accuracy within the analysed group, whereas C57 S, C57 M and X36 5CP progressively extend the usable measurement volume toward larger stand-off distances. This internal distribution of specifications reflects a typical trade-off in stereo sensing: as the observation volume increases, the system becomes more suitable for general three-dimensional perception tasks, but its capability to resolve very small local variations in depth becomes intrinsically more limited.

With respect to the present application, these data suggest that commercial stereo-vision sensors are particularly attractive when robustness, flexible working distance, and volumetric scene acquisition are prioritised. However, when the objective shifts toward the accurate reconstruction of the local morphology of the cutting edge and of the adjacent functional surfaces, the available specifications indicate a level of dimensional sensitivity that is generally less aligned with the stringent metrological requirements of cutting-tool inspection. For this reason, stereo vision remains highly relevant as a general three-dimensional sensing technology, but appears less naturally suited to the most demanding stages of micrometric tool-edge characterisation.

2.4.4 Depth-from-Focus

Depth-from-Focus (DFF) is a non-contact optical technique for three dimensional surface reconstruction based on the acquisition of multiple images at different focus positions. The method relies on the limited depth of field of an optical system: for a given focus setting, only points within a certain distance range are sharply imaged, while points at other depths appear blurred. By acquiring a sequence of images at different object distances, commonly referred to as a *focus stack*, each object point appears sharply focused in at least one image. The three-dimensional reconstruction is then obtained by identifying the image in which each point is best focused. In addition to the depth map, the method also provides a synthetic sharp image obtained by selecting the focused gray values from the stack.

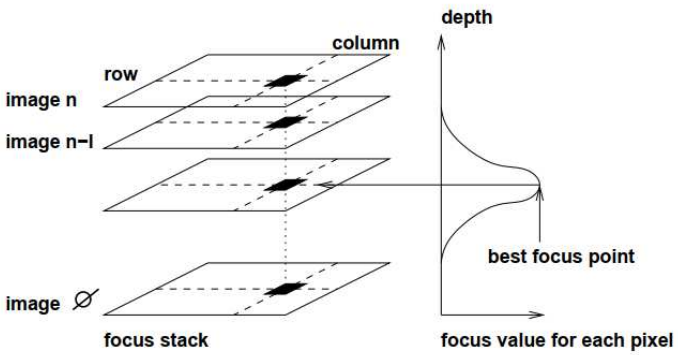

Figure 2.9: Conceptual scheme of the *Depth-from-Focus* principle. Adapted from [2].

As illustrated in Figure 2.9, the method associates each image point with the position in the focus stack at which its sharpness is maximal. From an instrumental point of view, DFF typically requires a single camera equipped with a telecentric lens or a microscopic imaging system, so as to achieve an approximately parallel projection. This is important because the method compares the same image coordinates across successive images, which therefore must remain comparable throughout the sequence. For the same reason, the focusing displacement must be applied parallel to the optical axis; otherwise, lateral shifts occur and pixel correspondence is compromised [2].

A central parameter of the method is the depth of field (DOF), which represents the distance range within which the image appears sharp. A low DOF improves sensitivity to height variations along the optical axis and therefore increases precision, but it also requires a larger number of focus positions to cover the full measurement range. According to the MVTec guide, since the depth of field of the lens is fixed, the minimum number of focus positions has to exceed

$$N_{\min} > \frac{\text{focus range}}{\text{depth of field of the used lens}}.$$

This ensures overlap between the depth-of-field regions of successive images, which is necessary for correct reconstruction. The same source also states that the transition of a surface region from blurred to sharp and back to blurred should extend over approximately five images. On this basis, a practical rule of thumb for the minimum number of acquired images is

$$N \approx \frac{\text{object height}}{\text{depth of field}} \times 5.$$

This relation should be interpreted as an empirical guideline for selecting a sufficiently dense focus stack, rather than as a fundamental physical law.

If the focus sequence is acquired with a constant displacement step z between consecutive images, the height difference between two points whose depth indices differ by n can be expressed as

$$\Delta h = z \cdot n.$$

In this case, the depth image returned by DFF is initially an index image, and metric height information can be obtained once the spacing between consecutive focus positions is known. The MVTec guide also notes that the

minimum number of images is typically around 10, whereas more than about 150 images usually do not provide further practical improvement because the achievable precision is eventually limited by camera noise [2].

From a metrological point of view, this family of techniques is particularly interesting because it can characterize both form and roughness within the same measurement framework. The literature also highlights its suitability for complex surfaces, steep flanks, and wear-measurement applications, making it relevant for the local characterization of cutting-tool microgeometries and surface topography [24].

At the same time, the technique presents important limitations. DFF is most suitable for small objects with textured surfaces, whereas perfectly polished or highly specular surfaces remain problematic. Reflections and overexposure may generate false sharp pixels and degrade the reliability of the reconstructed depth map. Moreover, because DFF is intrinsically based on multi-image acquisition, runtime is generally longer than in other 3D techniques, and final accuracy depends not only on the optical setup but also on the precision of the focusing displacement and the quality of the acquired images. In light of these considerations, DFF/FV can be regarded as an attractive solution when the objective is to characterize the local topography of small-scale features with high axial sensitivity, although its effective applicability to cutting tools depends on the compromise between resolution, acquisition time, robustness to reflections, and ease of integration into an industrial measurement system.

Reference Industrial Solution

To complement the theoretical discussion with a concrete industrial benchmark, this work considers a selection of Bruker Alicona instruments as representative examples of commercial systems based on focus-based optical topography [25]. Bruker Alicona is not an industrial partner of iMAGE, but was selected as a technological reference because of its established role in advanced optical surface metrology and three-dimensional topographic measurement. The analysis of the corresponding specifications shows how the expected strengths and limitations of this approach are reflected in the declared characteristics of real metrological devices

Bruker Alicona			
Technical Parameter	**IF Sensor R25 10x**	**IF Sensor R25 2xSX**	**EdgeMasterX 2xSX**
Working distance [mm]	17.5	34.0	34.0
Field X Y [mm]	2.0×2.0	10.0×10.0	10.0×10.0
Vertical resolution [μm]	0.10	3.5	3.5
Min. measurable radius [μm]	5.0	20.0	20.0

Table 2.6: Representative technical specifications of the Bruker Alicona configurations considered in this work.

The specifications reported in Table 2.6 show that the analysed systems are mainly oriented toward high-resolution local measurements rather than rapid inspection of extended areas. In particular, the IF Sensor R25 10x provides sub-micrometric vertical resolution, but over a strongly limited field of view. By contrast, the configurations based on 2xSX optics extend the observable area up to 10.0×10.0 mm, while offering lower vertical resolution and a larger minimum measurable radius.

For the present application, these specifications confirm that focus-based optical metrology is especially suitable for the detailed characterization of local microgeometry, such as very small radii, fine surface morphology, and subtle height variations. At the same time, they highlight the main trade-off of this class of systems: the highest vertical sensitivity is generally obtained only over a restricted field of view, limiting the surface area captured in a single acquisition.

Overall, the commercial solutions considered here support the view that depth-from-focus-related instruments are particularly promising when local metrological detail is prioritised over global acquisition efficiency. However, when the inspection task requires rapid and spatially extended reconstruction of the overall tool geometry, the reduced field of view of the most accurate configurations may become a significant practical limitation. Their suitability for the present study must therefore be assessed by balancing local measurement capability, acquisition coverage, and integration requirements.

2.4.5 Confocal Sensing

Confocal sensing is a non-contact optical measurement technique that reconstructs surface topography by exploiting the axial selectivity of a confocal optical system. In chromatic confocal sensing, this principle is combined with chromatic dispersion: a broadband light source is focused by a dispersive optical system so that different wavelengths come to focus at different axial positions. The height of the measured point is then inferred from the wavelength that is most sharply focused and most efficiently transmitted through the confocal detection path. Depth is therefore obtained not from geometric triangulation or multi-view disparity, but from the calibrated correspondence between wavelength and axial position.

From an instrumental point of view, a typical chromatic confocal sensor includes a broadband illumination source, dispersive optics, conjugate pinholes, and a spectral detection unit. The confocal arrangement suppresses most out-of-focus light, while the dispersive objective encodes axial position into the spectrum of the reflected signal. The optical architecture shown in Figure 2.10 represents a full-field implementation based on a pinhole array, beam splitter, dispersion optics, and hyperspectral detection, showing how the system can preserve a coaxial measurement geometry while extending the principle from point sensing to areal surface profilometry [26].

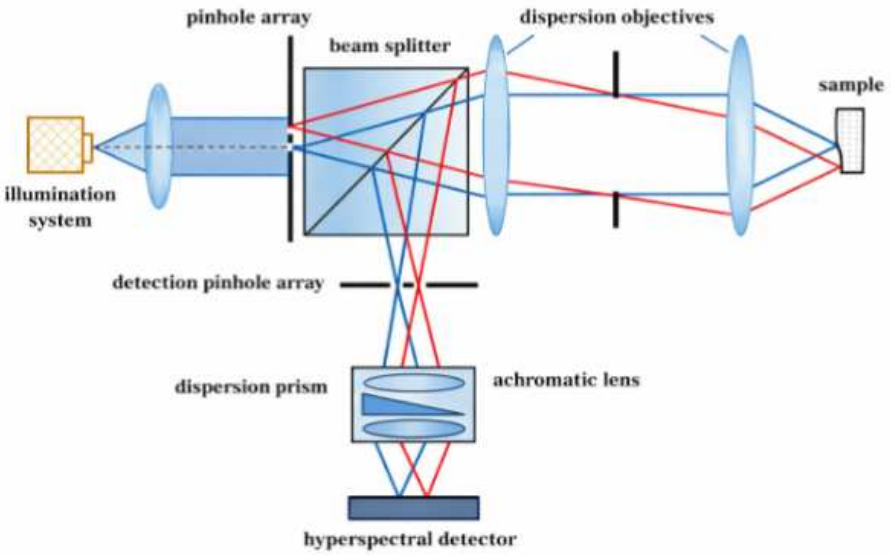

Figure 2.10: Simplified optical scheme of a full-field chromatic *Confocal Sensing* system. Adapted from [3].

A key advantage of confocal sensing is its high axial resolution and its ability to provide precise topographical information without physical contact. Recent review literature highlights the wide industrial use of chromatic confocal technology for high-precision displacement and profile measurements, owing to its compact optical configuration, robustness in displacement detection, and ease of integration into on-machine and online measurement systems. The same literature also reports its applicability to contour measurement, thickness measurement, and surface characterization in advanced manufacturing contexts.

Recent developments have also extended chromatic confocal microscopy toward full-field or quasi-area-scan profilometry, reducing dependence on conventional point-by-point mechanical scanning. In particular, Chen and Chen presented a quasi-area-scan chromatic confocal microscopy system for full-field surface profilometry, motivated by the need for accurate and efficient measurements in in-line automated optical inspection. Their results showed sub-micrometer performance, with measurement bias below 0.239 µm and a standard deviation of 0.126 µm on calibrated step-height gauges, while also highlighting the advantage of avoiding positioning uncertainties associated with mechanical platform scanning [3].

At the same time, confocal sensing presents important limitations. Measurement performance depends strongly on the quality and stability of the broadband source, the design of the dispersive optics, the spectral detection process, and the accuracy of wavelength-peak extraction and calibration. Review literature also points out that nonlinearities in the wavelength–position response, source instability, and the trade-off between speed and accuracy remain critical issues. Chen and Chen further note that, although chromatic confocal systems are attractive for industrial profilometry, they are not equally robust for all surface conditions, and difficulties may arise for surfaces whose color-filtering properties prevent the reflected signal from covering the full usable height range in a sufficiently linear way [26].

For the application considered in this work, confocal sensing is particularly attractive when the objective is the high-resolution characterization of local tool topography, especially near the cutting edge. Its coaxial measurement geometry, high axial sensitivity, and suitability for surface profilome-

try make it potentially more effective than several other optical techniques when the target is not merely the overall shape of the tool, but the fine morphology of micrometric functional surfaces. Its actual suitability for integration into an industrial presetting framework, however, depends on the achievable compromise among axial accuracy, field of view, acquisition speed, optical complexity, and robustness with respect to the reflective and material properties of real cutting tools [3].

Reference Industrial Solution

A similar comparison with industrial devices is also useful for confocal sensing, in order to relate the general metrological potential of the technique to actual operating specifications.To this end, a selection of high-precision confocal line scan sensors available from iMAGE S suppliers was analyzed. [13].

LMI Technologies				
Technical Parameter	**Model 4010**	**Model 4011**	**Model 4020**	**Model 4021**
Resolution X [μm]	1.9	1.9	2.6	2.6
Linearity Z [± % of MR]	0.04	0.04	0.02	0.02
Resolution Z [μm]	0.25	0.20	0.50	0.40
Repeatability Z [μm]	0.12	0.10	0.25	0.20
Field of View [mm]	3.5	3.5	5.0	5.0
Clearance distance [mm]	9.3 ± 0.2	9.3 ± 0.2	27.8 ± 0.3	27.8 ± 0.3
Measurement range [mm]	1.05	1.05	2.5	2.5

Table 2.7: Representative technical specifications of the confocal sensors considered in this work.

The specifications reported in Table 2.7 show clearly that the analysed confocal sensors are designed for highly localised measurement tasks requiring very high axial sensitivity. In particular, Models 4010 and 4011 provide the finest lateral sampling and the most favourable resolution and repeatability values along the Z axis, whereas Models 4020 and 4021 extend the field of view and the measurement range at the cost of slightly coarser lateral and axial performance. This internal distribution of specifications reflects a typical trade-off within the same technological family: the configurations that

offer the highest local sensitivity are also those operating over the smallest observable area.

From the point of view of the present application, these data confirm that confocal sensing is especially attractive when the objective is the accurate reconstruction of small-scale surface morphology, local edge geometry, and subtle height variations in the vicinity of the cutting edge. The reported sub-micrometric Z resolution and repeatability are fully consistent with the use of this technology for high-detail topographical inspection. At the same time, the available specifications also indicate that this performance is achieved over relatively limited fields of view and measurement ranges, which naturally restrict the extent of the surface that can be inspected in a single acquisition.

For this reason, the analysed commercial solutions support the view that confocal sensing should be regarded as one of the most promising technologies when local metrological accuracy is prioritised. Nevertheless, its effective suitability within the present work must be assessed by considering not only the achievable measurement quality, but also the reduced acquisition area and the practical implications that this may have for the inspection of complete cutting-tool geometries in an industrial environment.

2.5 Technology Comparison and Selection

The comparison developed in this chapter shows that the selection of a three-dimensional sensing technology for cutting-tool inspection must be treated as a trade-off problem rather than as the search for a universally superior solution. Each technology offers specific strengths and limitations, and its suitability depends on the requirements of the application.

Technologies such as confocal sensing and depth-from-focus are attractive from a metrological point of view because of their high axial sensitivity, but their limited field of view, reduced measurement range, and slower acquisition strategies make them less suitable for the efficient reconstruction of complete cutting-tool geometries in an industrial context. Conversely, stereo vision and structured light allow faster acquisition over larger areas, which is advantageous for broader surface reconstruction, but they do not

always provide the local sensitivity required for the most critical aspects of cutting-edge analysis. In particular, stereo vision appears more suitable for macroscopic 3D perception than for the accurate reconstruction of small cutting-edge features.

Within this framework, laser triangulation and structured light emerged as the two most promising technologies. Among the solutions analysed, they provided the best balance between resolution, observable area, working distance, acquisition speed, and integration feasibility. They were also the technologies most consistent with the sensor families made available by the suppliers involved in the project.

Laser triangulation proved particularly suitable because it combines micrometric profilometric capability with compact operating geometries and a scanning logic well adapted to the reconstruction of local cross-sections of the tool. Structured light, in contrast, offers dense areal acquisition and faster coverage of wider visible portions, making it attractive when surface coverage and acquisition efficiency are prioritised.

The final focus on these two technologies was therefore driven by practical and geometric constraints of the case study, including the size of the regions of interest, limited installation space, the presence of occlusions near the cutting edge, and the need for acquisition times compatible with an industrial workflow.

In conclusion, laser triangulation and structured light represent the most favourable trade-off for the three-dimensional reconstruction of cutting tools. Their selection was motivated not only by their theoretical suitability, but also by the fact that the available commercial sensor families offered the most appropriate combination of technical characteristics for the intended application. For this reason, they were chosen as the most promising candidates for the subsequent experimental investigation and system development carried out at iMAGE S and Speroni.

Chapter 3

Vision System Validation

Based on the considerations emerging from the state of the art, this chapter introduces the preliminary validation phase of the three-dimensional technologies deemed most suitable for the dimensional analysis of cutting tools. After identifying laser triangulation and structured light as the most promising solutions, an experimental assessment was conducted to verify whether the performance declared by manufacturers could be effectively achieved under the specific testing conditions of this study.

To this end, several profile and surface acquisitions were carried out in order to analyse key parameters such as resolution, repeatability, linearity, accuracy, and measurement range. However, to ensure a rigorous interpretation of these experimental results, it is first necessary to establish a solid theoretical framework. The following section outlines the fundamental metrological principles that define the validation methodology adopted throughout the experimental campaign.

3.1 Fundamental Metrological Concepts

In the present work, the experimental campaign is not intended to develop a complete uncertainty budget in the strict sense of the Guide to the Expression of Uncertainty in Measurement. Its purpose is instead to establish the main metrological concepts and statistical indicators required to interpret the behaviour of the vision system under repeated acquisitions and controlled laboratory conditions. The emphasis is therefore placed on the

experimental characterisation of sensor performance, rather than on the formal propagation and combination of all uncertainty contributions associated with the final measurement result [27].

This distinction is particularly relevant in the case of three-dimensional optical measurements. A vision sensor does not directly return a single scalar quantity, but rather a set of sampled coordinates, profiles, or surfaces, whose interpretation depends on the adopted geometric model and on the subsequent data-processing strategy. For this reason, the metrological discussion developed in this section is intended to provide a coherent framework for analysing systematic deviation, random dispersion, local fitting residuals, and repeatability over time, all of which are central to the validation methodology adopted in this chapter.

Measurement, Measurand, and Reference Value

Measurement: In metrology, a measurement is not merely a numerical output generated by an instrument; rather, it is the assignment of a value to a quantity that has been clearly specified in advance. This apparently simple statement is crucial, because the meaning of a measurement result depends not only on the sensor itself, but also on the exact quantity that is intended to be observed.

Measurand: The quantity intended to be measured is referred to as the *measurand*. In the context of a three-dimensional vision system, the measurand may correspond to different geometric entities depending on the purpose of the test, such as a height, a diameter, a radius, the position of an edge, or the local deviation of a profile from an ideal geometry. As a consequence, the result of measurement is inseparable from the way the measurand is defined, modelled, and observed.

Reference value: In experimental practice, the true value of the measurand is generally unknown. For this reason, the assessment of a measuring system is commonly carried out with respect to a *reference value*, that is, a value known with sufficiently small uncertainty for the intended purpose of the validation. Such a value may be provided by a certified artefact, a calibrated standard, or a measurement system of superior metrological quality [28].

Measurement Error, Sample Mean, and Bias

Measurement error: When a measured value x is compared with a reference value x_{ref}, the measurement error can be defined as

$$e = x - x_{\text{ref}} \tag{3.1}$$

This quantity expresses the deviation of the measured result from the adopted reference. It should nevertheless be noted that the reference value itself is generally associated with uncertainty; therefore, the error is not a perfectly known quantity, but rather an operational descriptor of agreement with the best available reference [28].

Sample mean: When repeated measurements of the same quantity are available, the first statistical descriptor of interest is the sample mean,

$$\bar{x} = \frac{1}{N} \sum_{i=1}^{N} x_i \tag{3.2}$$

where x_i denotes the i-th observation and N is the total number of repeated measurements. Under fixed experimental conditions, the sample mean provides the central estimate of the system response and constitutes the natural starting point for assessing possible systematic deviation with respect to the reference [29].

Bias: The systematic displacement of the mean result from the reference value is commonly estimated through the bias,

$$b = \bar{x} - x_{\text{ref}} \tag{3.3}$$

which represents an operational estimate of the systematic component of the error. In practical terms, a non-zero bias indicates that the system tends to return values that are consistently shifted with respect to the adopted reference, even when the measurement is repeated under nominally identical conditions [29].

Systematic Error and Random Error

Systematic error: The systematic component of measurement error is the part that remains constant, or varies in a predictable manner, when repeated measurements are performed under the same conditions. It is therefore associated with persistent causes such as misalignment, calibration

offsets, geometric mis-modelling, or deterministic drifts of the measurement chain. In experimental validation, the bias is the most direct estimator of this contribution.

Random error: The random component of error is the part that varies unpredictably from one observation to another. It is generated by stochastic fluctuations in the acquisition process, including sensor noise, environmental perturbations, small illumination changes, or local variations in the interaction between the optical signal and the observed surface. Unlike systematic error, random error does not produce a stable offset, but rather a statistical dispersion of the measured values around their mean [28].

This distinction is particularly important in the analysis of optical sensors. A system may be affected by a substantial systematic offset while still maintaining a very limited random spread, or conversely it may be well centred with respect to the reference and yet exhibit poor repeatability due to a high stochastic component. In metrological terms, these two behaviours correspond to fundamentally different limitations and must therefore be evaluated separately [29].

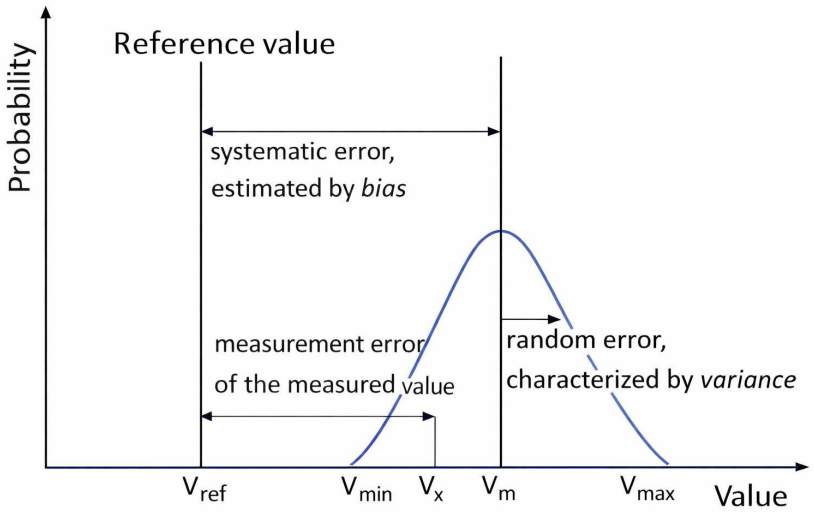

Figure 3.1: Systematic and random components of measurement error.

The graphical representation of error components is particularly useful because it makes explicit the different roles of location and spread in the interpretation of repeated measurements. The displacement of the centre of the distribution with respect to the target is associated with systematic

behaviour, whereas the width of the distribution reflects the contribution of random effects [30].

Standard Deviation and Dispersion of Repeated Measurements

Standard deviation: The dispersion of repeated measurements around their mean is commonly described through the sample standard deviation,

$$s = \sqrt{\frac{1}{N-1}\sum_{i=1}^{N}(x_i - \bar{x})^2} \tag{3.4}$$

with the corresponding sample variance

$$s^2 = \frac{1}{N-1}\sum_{i=1}^{N}(x_i - \bar{x})^2 \tag{3.5}$$

The use of the factor $N-1$ reflects the standard Bessel correction for finite samples. [29]

Interpretation: The standard deviation quantifies how tightly the repeated values cluster around the mean. A small value indicates limited random variability and therefore a stable response of the measurement system under repeated conditions. A large value, on the contrary, indicates that the sensor output is strongly affected by stochastic fluctuations. Since the standard deviation is expressed in the same unit as the measured quantity, it provides an immediately interpretable measure of dispersion [29].

Trueness, Precision, and Accuracy

Trueness: Trueness describes the closeness of agreement between the mean of a large number of repeated results and an accepted reference value. It is therefore mainly related to the systematic component of the measurement error. A system characterised by low bias may be described as having high trueness [31].

Precision: Precision describes the closeness of agreement among independent results obtained under specified conditions. It is governed by the dispersion of the measured values and therefore depends on random effects rather than on the distance from a reference value. A highly precise system is one that produces tightly clustered results, regardless of whether these are centred on the correct value [31].

Accuracy: Accuracy expresses the closeness of agreement between a measurement result and the accepted reference value. In practical terms, it depends on both trueness and precision. Nevertheless, within the VIM framework, accuracy is not generally treated as a quantity to which a single numerical value can always be assigned; rather, it is regarded as a qualitative property of a measurement result or of a measurement system. For this reason, in the experimental sections that follow, the discussion is explicitly articulated in terms of bias, dispersion, and repeatability, while the term *accuracy* is used only in a broad descriptive sense [28].

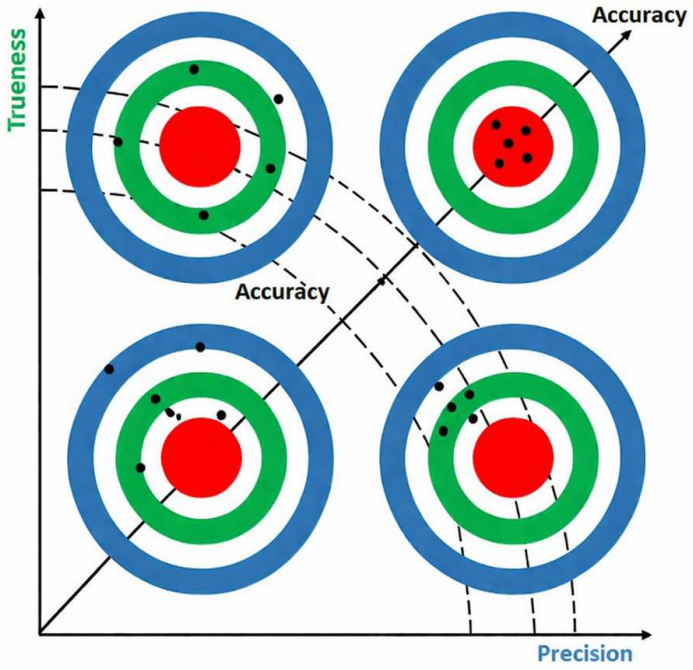

Figure 3.2: Relationship among trueness, precision, and accuracy.

The target-style diagram remains a useful didactic representation provided that trueness, precision, and accuracy are interpreted correctly. In particular, a clustered group of points far from the target centre corresponds to high precision but low trueness, whereas a broadly dispersed cloud centred around the target corresponds to higher trueness but lower precision [30].

Reference Fitting and Residual Analysis

Reference fitting: In the characterisation of continuous profiles acquired by a vision sensor, the reference is not always an externally assigned scalar value. In many practical cases, the observed data are compared with an ideal geometric model, such as a line, a plane, or a circle, estimated directly from the acquired points through a least-squares fitting procedure. This fitted geometry provides an analytical representation of the global shape of the measured feature.

Residuals: Once the reference model has been estimated, the local deviations between the measured coordinates z_i and the values predicted by the model $\hat{z}_i$ can be written as

$$r_i = z_i - \hat{z}_i \tag{3.6}$$

These quantities are referred to as residuals and describe the local mismatch between the acquired profile and the adopted geometric model [29].

Metrological meaning: Residual analysis is particularly relevant in optical metrology because it makes it possible to separate the global geometric trend of the object from local deviations. In the present context, residuals are used to evaluate the internal consistency of the acquired profile and to quantify the small-scale fluctuations that remain once the nominal geometry has been removed. It should, however, be emphasised that residuals do not directly express the absolute measurement error with respect to an external standard, since the reference model is estimated from the same dataset. They are therefore especially suited to characterising local spatial dispersion rather than absolute trueness [29].

Spatial Variability and Temporal Repeatability

Spatial variability: A first source of dispersion in a vision-based acquisition is the point-to-point variability observed within a single frame or profile. In this work, such behaviour is evaluated through the residuals computed with respect to the fitted reference geometry. The standard deviation of the residuals therefore acts as an indicator of local spatial noise, capturing the amplitude of short-scale deviations that remain after the nominal shape has been removed.

Temporal repeatability: A second source of variation concerns the sta-

bility of the system over time. This property is assessed by repeating the acquisition of the same measurand under nominally identical conditions and by tracking the variation of a selected geometric parameter across the repeated measurements. If y_j denotes the value of a given parameter estimated from the j-th acquisition, temporal repeatability may be described through

$$\sigma_{\text{temp}} = \sqrt{\frac{1}{N-1}\sum_{j=1}^{N}(y_j - \bar{y})^2} \tag{3.7}$$

where $\bar{y}$ is the mean of the repeated estimates. [28]

Interpretative distinction: The distinction between spatial variability and temporal repeatability is essential in the analysis of optical sensors. The former quantifies the internal structure of dispersion within one acquisition, whereas the latter quantifies the stability of the same result across repeated acquisitions. These two aspects should not be merged into a single indicator, because they reflect different physical mechanisms and provide different information about the measurement system [31].

Statistical Indicators Adopted in This Work

Mean Absolute Error (MAE): In order to quantify the deviation between measured data and the adopted reference, the Mean Absolute Error is defined as

$$MAE = \frac{1}{N}\sum_{i=1}^{N}|x_i - \hat{x}_i| \tag{3.8}$$

where x_i denotes the measured value and $\hat{x}_i$ the corresponding expected or reference value. The MAE provides a direct estimate of the average magnitude of the deviation and is expressed in the same unit as the measured quantity [29].

Root Mean Square Error (RMSE): The Root Mean Square Error is defined as

$$RMSE = \sqrt{\frac{1}{N}\sum_{i=1}^{N}(x_i - \hat{x}_i)^2} \tag{3.9}$$

Because the squared term increases the weight of larger deviations, the RMSE is more sensitive than the MAE to local peaks, outliers, or strong departures from the expected behaviour [29].

Standard deviation of residuals: When the reference is a fitted geometric model, the local dispersion of the acquired data is described through the standard deviation of the residuals,

$$\sigma_r = \sqrt{\frac{1}{N-1}\sum_{i=1}^{N}(r_i - \bar{r})^2} \tag{3.10}$$

where r_i denotes the residual associated with the i-th point and $\bar{r}$ is the mean residual. In the present work, this quantity is treated as the primary indicator of local spatial noise and of the effective internal consistency of the reconstructed profile [29].

Within the validation framework adopted in this chapter, MAE and RMSE are mainly used to quantify the global agreement between the acquired data and the adopted reference, whereas the standard deviation of the residuals is used to describe the local spatial dispersion of the profile. Temporal repeatability is instead evaluated separately through repeated acquisitions of the same feature. Taken together, these indicators provide the minimum statistical and metrological basis required to interpret the behaviour of the sensor in a rigorous way before moving to the experimental results presented in the following sections.

3.2 Experimental Setup and Initial Tests

The experimental investigation began with the Gocator 2520 laser line profiler. In order to assess the suitability of the selected sensor, it was tested, in an initial exploratory phase, on a series of tools provided by Speroni, with the aim of analyzing the overall quality of the acquired profiles and verifying its practical compatibility with the intended application.

In the first experimental phase, a dedicated test bench was assembled, in which the sensor was mounted on a fixed structure to keep the laser beam as perpendicular as possible to the underlying plane. The tool under analysis was instead positioned on a movable stage designed to allow linear motion, as shown in Figure 3.3.

Table 3.1: Main nominal specifications of the Gocator 2520. Adapted from [4]

Parameter	Nominal value
Data points per profile	1920
Scan rate	1600–20000 Hz
X resolution	13–17 μm
Z linearity	$\pm$0.006% of MR
Z repeatability	0.4 μm
Clearance distance (CD)	47.5 mm
Measurement range (MR)	25 mm
Field of view (FOV)	25.0–32.5 mm
Dimensions	46 × 80 × 110 mm
Weight	0.65 kg

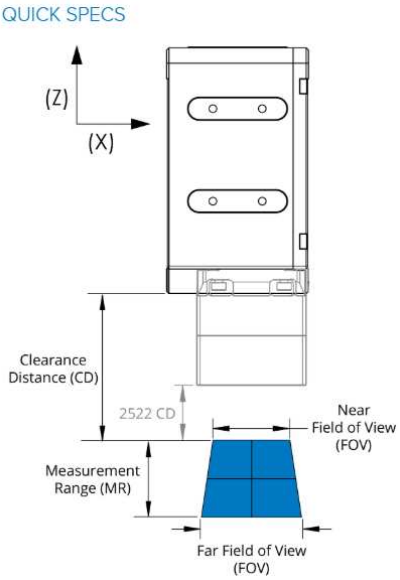

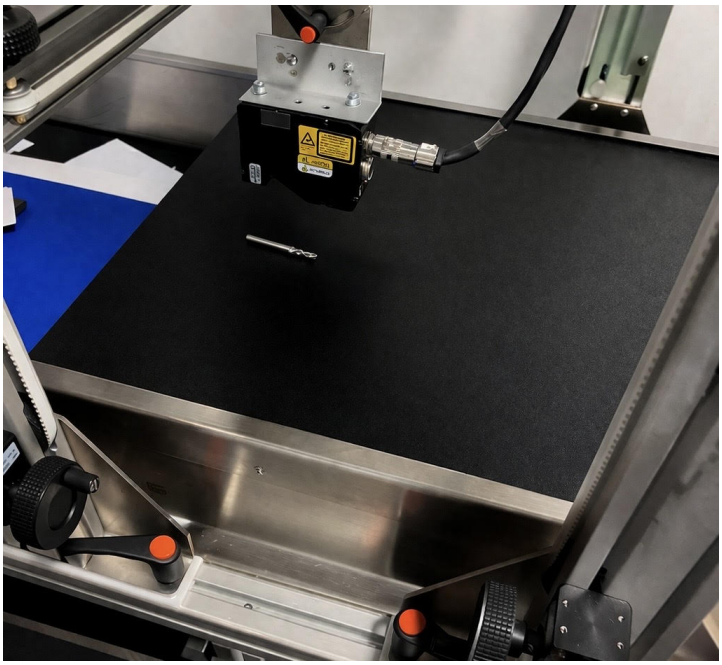

Figure 3.3: Initial experimental setup.

The first scans acquired with the proposed setup revealed a variation in the vertical distance between the tool and the sensor along the scanning direction, suggesting a systematic misalignment of the motion system.

To quantify this effect, the data were processed in MATLAB. Two circles

were fitted to two significant sections of the tool profile, and the uppermost point of each circle was extracted:

$$P_1 = (-0.7937,\ 5.9320,\ 5.9766) \qquad P_2 = (-0.5126,\ 15.9299,\ 6.0154)$$

Considering their projection in the YZ-plane, the reference line was defined as:

$$z(y) = z_1 + \frac{z_2 - z_1}{y_2 - y_1}(y - y_1) \tag{3.11}$$

and the corresponding slope was computed as:

$$m = \frac{\Delta z}{\Delta y} = \frac{6.0154 - 5.9766}{15.9299 - 5.9320} \approx 0.00388 \text{ mm/mm} = 3.88\ \mu\text{m/mm}. \tag{3.12}$$

This result confirmed the presence of a systematic longitudinal drift not attributable to the actual tool geometry. For this reason, the subsequent validation phase was carried out using certified gauge blocks in order to isolate the intrinsic sensor performance from motion-related positioning errors.

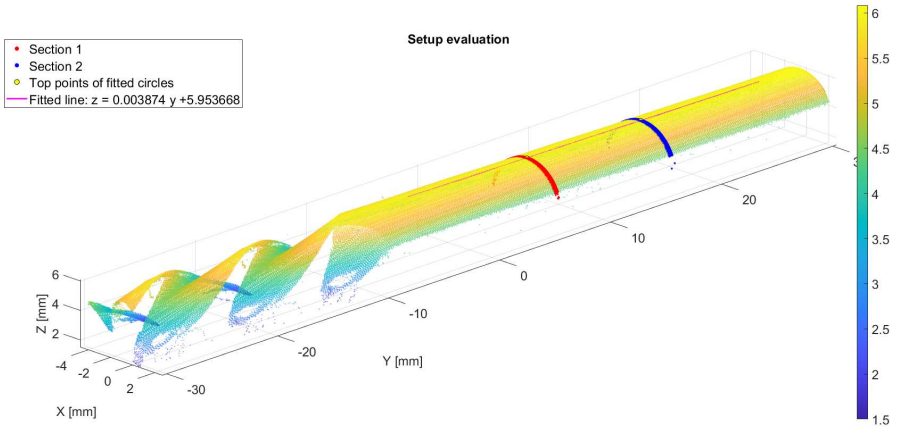

Figure 3.4: Analysis of the longitudinal slope through linear fitting.

3.3 Static Gauge Block Validation

In light of the initial exploratory scans, a more controlled validation procedure based on artefacts with known and certified geometry became necessary. Although the first acquisitions on actual cutting tools helped identify

the main limitations of the experimental setup, they did not provide a sufficiently robust reference for rigorous metrological assessment, owing to the combined influence of part geometry, positioning uncertainty, and motion-system imperfections. For this reason, before the subsequent tests, the setup was modified to achieve the most stable and controlled support condition possible within the available experimental constraints. In particular, the structural support was reinforced and the original plywood surface was replaced with a smooth aluminium plate, which was stiffer, heavier, and mechanically more stable. This modification reduced local deformation, minimised bench displacement during gauge block placement, and provided a more regular contact surface for the artefact. In the initial configuration, even inserting or replacing a block could slightly alter system alignment, causing undesired variations in the acquired profiles. The structural improvement therefore significantly reduced these effects, simplifying data analysis and increasing the overall stability of the measurement process.

For the subsequent validation phase, certified Johansson gauge blocks were selected because of both their simple geometry and their established role as material length standards in dimensional metrology [32]. These artefacts fall within the framework defined by ISO 3650, which specifies their main constructive and metrological characteristics, together with the admissible deviations and tolerances as a function of calibration grade and accuracy class.

Figure 3.5: Certified Johansson gauge block set used as material length standards during the experimental validation.

For gauge blocks with nominal lengths between 1 mm and 10 mm, which are relevant to the present study, the standard specifies two main metrological parameters: the maximum deviation from nominal length, i.e. the maximum allowable difference between the actual block length and its nominal value, and the variation in length, i.e. the maximum allowable difference in length measured at different points on the same measuring face [32]. In other words, the first parameter is related to how close the block is to its nominal value, whereas the second describes the geometrical uniformity of the measuring face. For this dimensional range, the limits are reported below, where the first value denotes the maximum deviation from nominal length, the second the variation in length and the grade represents the four different levels of precision:

- **Grade K**: ± 0.20 μm; 0.05 μm
- **Grade 0**: ± 0.12 μm; 0.10 μm
- **Grade 1**: ± 0.20 μm; 0.16 μm
- **Grade 2**: ± 0.45 μm; 0.30 μm

Despite the improvements introduced in the setup, the adopted configuration did not reproduce the formal wringing conditions prescribed by ISO 3650 for the metrological determination of gauge block length: the blocks were simply placed on the support surface and scanned from above, rather than wrung to an auxiliary platen under standard reference conditions [32]. Consequently, in this study the certified gauge block was not used to reproduce its primary calibration procedure, but as a high-quality dimensional artefact within a practical and mechanically stabilised configuration. This distinction is relevant, but it does not invalidate the analysis. Even without the ideal metrological conditions required for the absolute determination of gauge block length, the test remains meaningful for evaluating the behaviour of the laser triangulation sensor. By acquiring multiple consecutive profiles of the same artefact under unchanged operating conditions, it is possible to assess whether the system response remains stable over time and whether variability between successive acquisitions is limited. In this sense, even if the measured height does not exactly coincide with the certified nominal value of the gauge block, a low dispersion among repeated measurements still provides a reliable indication of system repeatability and,

more generally, of sensor precision. The mean deviation from the expected value, on the other hand, must be interpreted separately, since it also reflects systematic effects introduced by the measurement configuration, the support plane, and the absence of wringing. Therefore, in the present work Johansson gauge blocks are used not to verify their length according to the primary definition established by the standard, but as high-quality geometric references for analysing the stability, repeatability, and dimensional behaviour of the sensor in an experimental configuration that is as controlled as possible.

A schematic representation of the acquisition setup adopted for the first scans of the Johansson gauge blocks is shown in Figure 3.6.

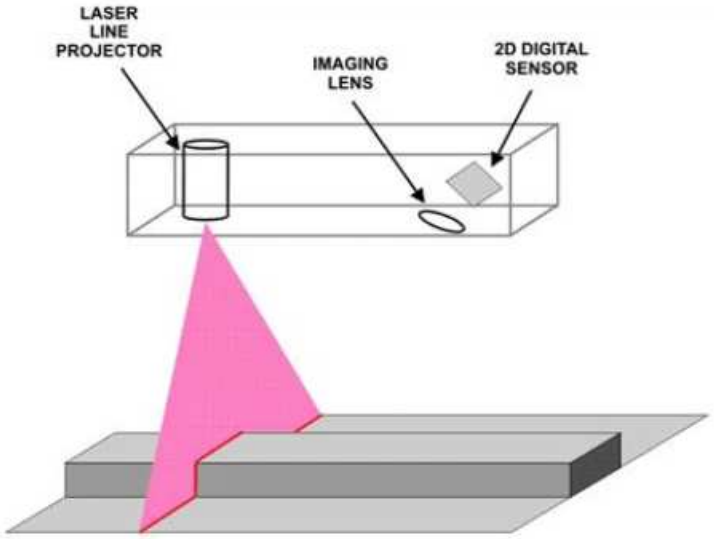

Figure 3.6: Representation Gauge block acquisition setup.

Once the experimental setup was defined, the first controlled acquisitions were performed on a certified 1 mm Johansson gauge block. This component is presented as a representative case study to illustrate the analytical methodology, without repeating the results for the other dimensional classes, given their similar behaviour. The artefact was placed on the support plane under the laser triangulation sensor and kept stationary throughout the test. Under these conditions, the sensor acquired 10 consecutive profiles in the same position to evaluate its response under repeatable and geometrically stable conditions.

The acquisitions were first visualised in GoPxL, the software environment

provided by LMI, enabling an initial qualitative inspection of the recorded profiles. The profiles were then exported as `.csv` files and imported into MATLAB for more detailed analysis and for generating the graphical representations used in the study. Within this environment, a dedicated script was developed to analyse both the single profile, through linear fitting and residual computation, and the full set of 10 acquisitions through point-by-point averaging of the coordinates of the measured points.

3.3.1 Profile Visualization and Linear Reference Fitting

The following figure shows, as an example, a single acquired profile of the 1 mm gauge block and its corresponding best-fit line. This representation enables a visual assessment of the distribution of measured points around the interpolating model, providing an initial qualitative evaluation of the sensor's local dispersion.

At this stage, the analysis focuses on **measurement precision**, understood as the stability of the system response and the stochastic deviation of the acquired points from the ideal reference geometry. The observed dispersion reflects the intrinsic noise of the laser acquisition process. In the case of the 1 mm block, the sensor shows a consistent response across the 1882 points of the profile, confirming the high quality of the data captured on the lapped surface.

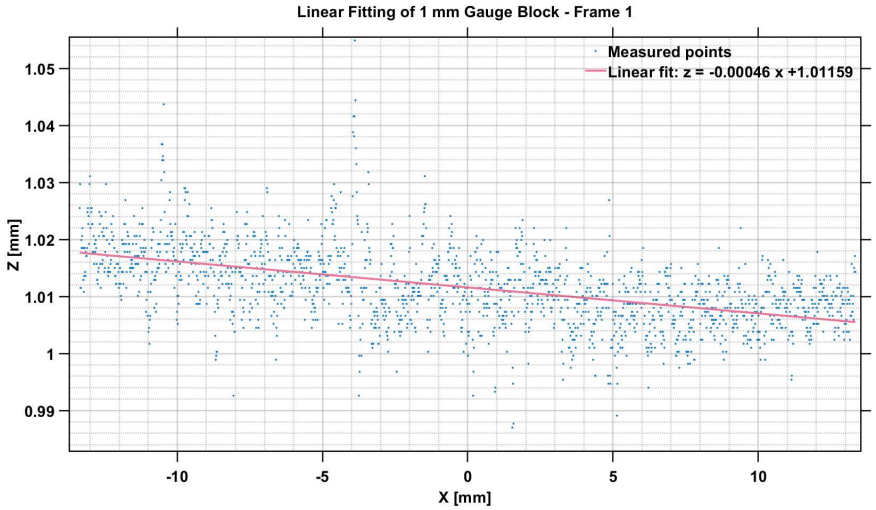

Figure 3.7: Linear fitting of the 1 mm gauge block profile.

To evaluate the acquired profile against an ideal planar reference, the measured points in the $X - Z$ plane were approximated by a straight line of the form:

$$z = ax + b,$$

where a is the slope and b is the intercept. This fitting step is necessary because the sensor provides a discrete set of measured points rather than a continuous geometric entity; therefore, a single representative line must be extracted from the profile before any residual analysis can be carried out.In the present case, the X coordinate is defined by a fixed sampling grid, the resolution of which varies as a function of the object's distance within the measurement range; meanwhile, the Z coordinate represents the measured height of the profile. For this reason, the reference line was estimated by means of an ordinary least-squares linear regression, implemented using MATLAB's `polyfit` function. The method determines the coefficients a and b that minimize the sum of the squared vertical residuals between the measured points and the fitted line:

$$\min_{a,b} \sum_{i=1}^{N} \left[z_i - (ax_i + b) \right]^2 .$$

Once computed, the best-fit line is used as the geometric reference of the profile. This makes it possible to separate the overall tilt of the scan from the local deviations of the measured points, which can then be analyzed through the residual distribution. In particular, the fitted slope provides a direct indication of any systematic inclination of the profile, while the residuals quantify the dispersion of the data around the reference line and are therefore used to assess measurement quality and repeatability.

The core implementation of the linear fitting procedure is reported in Listing 3.1.

Listing 3.1: Linear fitting using MATLAB's `polyfit` function.

```
% Linear regression to estimate the reference line
p = polyfit(x, z, 1);
a = p(1);
b = p(2);

% Evaluate the fitted profile and residuals
z_fit = polyval(p, x);
r = z - z_fit;
```

3.3.2 Residual Error Analysis

Once the best-fit line has been estimated, the quality of the acquired profile can be evaluated through the analysis of the residuals, namely the deviations between the measured points and the fitted reference line. This step makes it possible to separate the global geometric trend of the scan, associated with the overall tilt of the profile, from the local fluctuations of the signal.

Let z_i be the measured height at position x_i, and let $z_{\text{fit},i}$ be the value predicted by the fitted line at the same location. The residual is defined as

$$r_i = z_i - z_{\text{fit},i} \qquad \text{with} \qquad z_{\text{fit},i} = ax_i + b.$$

In this way, the linear component of the profile is removed, and the residuals describe only the local deviations of the acquired points with respect to the geometric reference.

For the first frame of the 1 mm gauge block, the residual analysis yielded the following values:

- **Mean Absolute Error (MAE)**: 0.004421 mm $\approx$ 4.42 μm;
- **Root Mean Square Error (RMSE)**: 0.005977 mm $\approx$ 5.98 μm;
- **Standard deviation of the residuals**: $\sigma = 0.005977\,\text{mm} \approx 5.98\,\mu\text{m}$.

These values indicate that, for a single acquisition, the dispersion of the profile around the fitted line is limited to a few micrometers, thus confirming the good metrological quality of the measurement even without temporal averaging. The near coincidence between RMSE and σ is consistent with the fact that the residuals are centered around zero, as expected for an ordinary least-squares fit.

The aligned residual plot provides a spatial representation of the error distribution along the scan axis. In the present case, the residuals remain globally distributed around the zero reference without showing evident large-scale trends, such as residual slope or curvature. This suggests that the linear model correctly represents the overall geometry of the profile. At the same time, some localized peaks are visible, which can reasonably be attributed to isolated disturbances in the acquisition process, such as optical noise, local reflections, or small variations in the triangulation response.

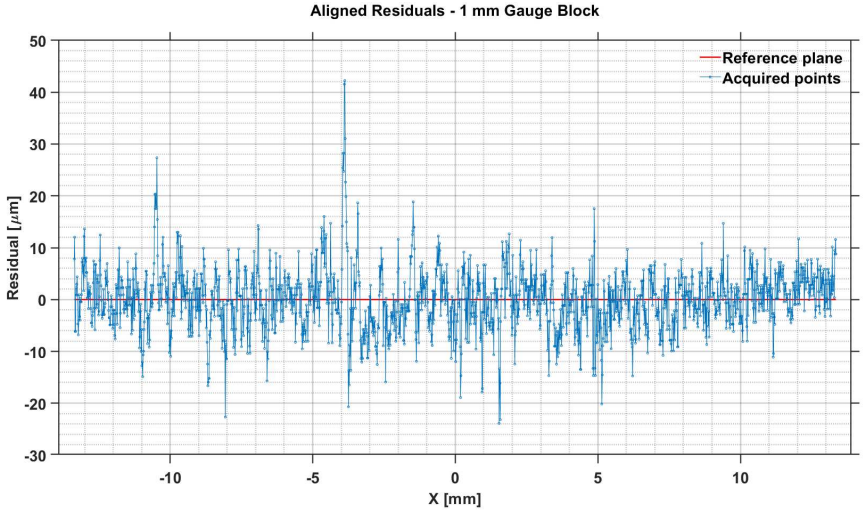

Figure 3.8: Aligned residuals of frame 1 on the 1 mm gauge block.

The residual histogram provides a complementary view of the deviations. Centered around zero and approximately bell-shaped, it indicates that the measurements are mainly affected by random noise. Most points lie close to the fitted line, while larger deviations are rare.

The profile shows high spatial precision: 95.5% of residuals fall within $\pm 2\sigma$, and 98.9% within $\pm 3\sigma$. This confirms that point dispersion along the scan is mainly due to stochastic random error rather than systematic distortion, and remains clearly distinct from the system's much lower temporal variability.

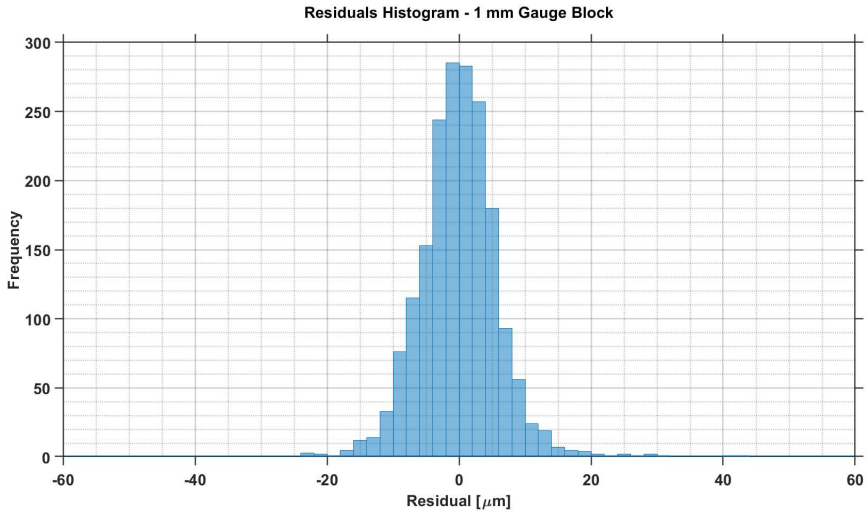

Figure 3.9: Residual histogram for frame 1 on the 1 mm gauge block.

Overall, the residual analysis of a single profile confirms two important aspects. First, the fitted line provides an adequate geometric representation of the acquired profile, since no significant systematic trend remains after detrending. Second, the residual dispersion is limited and substantially centered around zero, which indicates that the remaining uncertainty is mainly associated with local random effects. This analysis therefore provides the basis for the subsequent repeatability assessment, in which multiple profiles acquired under the same operating conditions are compared.

3.3.3 Temporal Analysis

While the residual analysis of a single frame provides information regarding the local measurement error within a single acquisition, temporal repeatability must be evaluated by comparing multiple profiles acquired under unchanged operating conditions. To this end, ten consecutive scans of the 1 mm gauge block were analyzed to quantify the measurement stability and the scan-to-scan variability of the reconstructed profile.

For each sampling position x_i, the mean profile was computed over the ten acquisitions, along with the pointwise temporal standard deviation (σ_{temporal}). The resulting representation provides two complementary pieces of information: the mean profile describes the average geometric behavior of the scan, while the vertical error variations associated with each point quantify the oscillation of the measured height across repeated acquisitions at the same spatial location.

By applying the same ordinary least-squares linear regression approach, the reference line for the mean profile was defined.

$$z = -0.000438911x + 1.011192$$

This enabled the integration within the same diagram of both the average geometry of the gauge block and the vertical variability of each point relative to the mean of the ten acquisitions.

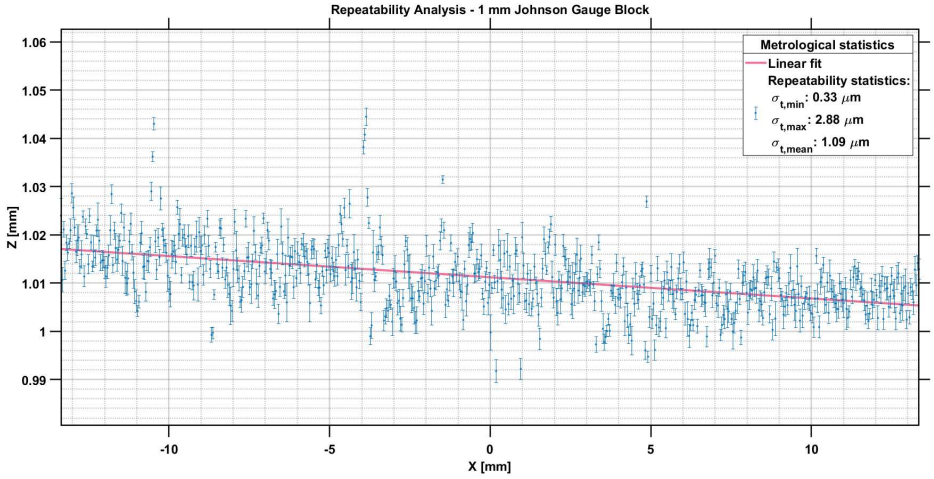

Figure 3.10: Mean profile of the 1 mm gauge block with temporal variability visualization. For graphic clarity, one data point in every three is shown.

The pointwise standard deviation across the ten acquisitions was used to evaluate the temporal stability of the measurement. The following values were obtained:

- $\sigma_{\mathbf{temporal,min}} = 0.33$ μm;
- $\sigma_{\mathbf{temporal,max}} = 2.88$ μm;
- $\sigma_{\mathbf{temporal,mean}} = 1.09$ μm.

These values are significantly smaller than the residual dispersion observed within a single frame, which was approximately 6 μm. This indicates that the dominant contribution to the residuals of a single profile is associated with local measurement noise, whereas the variability between repeated scans performed under the same conditions remains much more limited. In this sense, the superposition of the ten profiles confirms a high level of repeatability for the acquisition system.

For completeness, the main residual-based indicators were evaluated independently for each of the ten frames. In this case, MAE, RMSE, and the residual standard deviation were used to describe the spatial dispersion of each individual profile relative to its own fitted line, while the pointwise standard deviation across repeated scans served as an indicator of temporal repeatability. The results reported in Table 3.2 show a high level of

consistency across the entire dataset, with only minor frame-to-frame fluctuations. Specifically, the residual standard deviation remains close to 6 μm for all frames, while the MAE stays around 4.4 μm, confirming the overall stability of the acquisition process.

Table 3.2: Residual-based metrics for the ten repeated acquisitions of the 1 mm gauge block.

Frame	**MAE** [μm]	**RMSE** [μm]	σ_{spatial} [μm]	**Slope** a	**Intercept** b
1	4.4213	5.9769	5.9785	-4.5551×10^{-4}	1.01159
2	4.4201	5.9875	5.9891	-4.2225×10^{-4}	1.01145
3	4.3755	5.9877	5.9893	-4.1473×10^{-4}	1.01137
4	4.3519	5.9359	5.9374	-4.3360×10^{-4}	1.01140
5	4.3855	5.9367	5.9383	-4.3278×10^{-4}	1.01092
6	4.3398	5.9246	5.9262	-4.3761×10^{-4}	1.01139
7	4.4905	6.0346	6.0362	-4.4143×10^{-4}	1.01130
8	4.3492	5.9637	5.9653	-4.4528×10^{-4}	1.01085
9	4.4578	6.0257	6.0273	-4.6414×10^{-4}	1.01088
10	4.4340	5.9884	5.9899	-4.4178×10^{-4}	1.01077
Mean	4.4026	5.9762	5.9777	-4.3891×10^{-4}	1.01119

3.3.4 Comparative Analysis Across Different Gauge Blocks

To ensure the validity of the results, the experimental procedure was extended to gauge blocks of different nominal lengths: 1 mm, 2 mm, 5 mm, and 10 mm. The objective was to verify if the sensor's performance, remained constant across the measuring range.

Table 3.3 summarizes the main metrological indicators for all the analyzed blocks, comparing spatial dispersion and temporal repeatability.

Table 3.3: Summary of error metrics, spatial precision, and temporal repeatability for all analyzed gauge blocks.

Gauge Block	**MAE** [μm]	**RMSE** [μm]	σ_{spatial} [μm]	σ_{temporal} [μm]
1 mm	4.40	5.98	5.98	1.09
2 mm	7.10	9.88	9.88	0.89
5 mm	3.92	5.02	5.03	0.57
10 mm	5.69	7.77	7.77	0.63

The comparative analysis leads to the following conclusions:

- **Resolution**: The spatial standard deviation ($\sigma_{spatial}$) remains stable, ranging approximately between 5 μm and 10 μm across all tested blocks. This consistency suggests that these values represent the intrinsic resolution limit of the Gocator 2520 under the specific laboratory conditions. Since this dispersion is not significantly reduced by averaging the ten frames, it is attributable to a systematic spatial pattern associated with the optical interaction between the laser and the lapped metallic surfaces.
- **Setup Stability Validation**: The mean temporal standard deviation ($\sigma_{temporal}$) was systematically lower than 1.1 μm for every tested dimension. This result confirms the effectiveness of the mechanical solutions adopted to stabilize the system, demonstrating that environmental vibrations or structural drifts are negligible and do not affect the quality of the profile reconstruction.
- **Uniformity of Response**: The lack of significant correlations or trends between the block size and the error metrics (MAE and RMSE) proves that the sensor maintains a stable uncertainty profile and a linear response throughout its entire measuring range.

In conclusion, the tests performed on the certified gauge blocks yielded satisfactory results, confirming that the system is characterized by high repeatability and spatial precision adequate for the objectives of the study. Although the scan is affected by a systematic residual uncertainty (often associated with reflection phenomena), the overall performance demonstrates that the instrument serves as a reliable reference for the subsequent geometric characterization of the profiles.

3.4 Static Tool Validation

At the conclusion of the experimental activity carried out at the iMAGE S laboratories, further analyses were conducted on the cutting tools provided by Speroni. Although the intrinsic limitations of the experimental setup were acknowledged, in particular the issues related to the inclination of the plane, the inhomogeneities of the support surface, and the insufficient accu-

racy of the motion system for performing dynamic scans, it was considered appropriate to proceed with a series of acquisitions under static conditions. This phase made it possible to investigate several critical aspects related to surface finish, the helical geometry of the tool, and the influence of the angles in the vicinity of the cutting edges, thus providing useful insight into how these factors affect the quality of the acquired data.

In order to carry out this analysis starting from a known geometric reference, attention was initially focused on the tool shank. Its use as a reference offers significant metrological advantages: the intersection of the cylindrical shaft and the laser beam perpendicular to its axis generates a circular profile, a geometrical entity that is simpler to model and analyse than the morphology of the cutting edges. Furthermore, the regularity of its surface provides a controlled testbed for evaluating the sensor response on reflective metallic materials, reducing the influence of geometric irregularities that are difficult to quantify a priori and thereby making it possible, as far as possible, to isolate the optical behaviour of the instrument.

3.4.1 Exposure Optimization and Saturation Management

The first major criticality observed during the analysis of the profiles acquired in GoPxL concerned the non-uniform distribution of saturation along the shank section. From the very first acquisitions, it was evident that the upper portion of the tool, namely the region of the circumference located directly beneath the sensor, exhibited a significantly higher saturation level than the rest of the profile. This behaviour is consistent with both the acquisition geometry and the reflective nature of the metallic surface: in the uppermost region of the shank, the reflected beam tends to return to the receiving system with higher intensity, thereby increasing the likelihood of pixel saturation and of local degradation in the measured profile.

To address this issue, we adjusted the exposure parameters in order to identify a trade-off between two competing requirements: reducing saturation in the most reflective areas while preserving a sufficiently strong signal in regions that were less illuminated or optically less favourable. According to the official LMI documentation, exposure defines the activation time of

the camera and light source, expressed in microseconds. Longer exposure times improve the detectability of dark or distant surfaces, but they also reduce the maximum acquisition frequency, whereas polished or mirror-like surfaces generally require shorter pulse widths [33].

In the first stage of this activity, we therefore varied the single exposure time in order to observe how the profile behaved in the most critical regions of the shank. This analysis clearly showed that a single exposure value could not adequately manage the entire acquired circumference: values low enough to limit saturation in the upper area tended to weaken the signal in the lateral regions, whereas higher values improved the overall continuity of the profile but further increased saturation directly below the sensor.

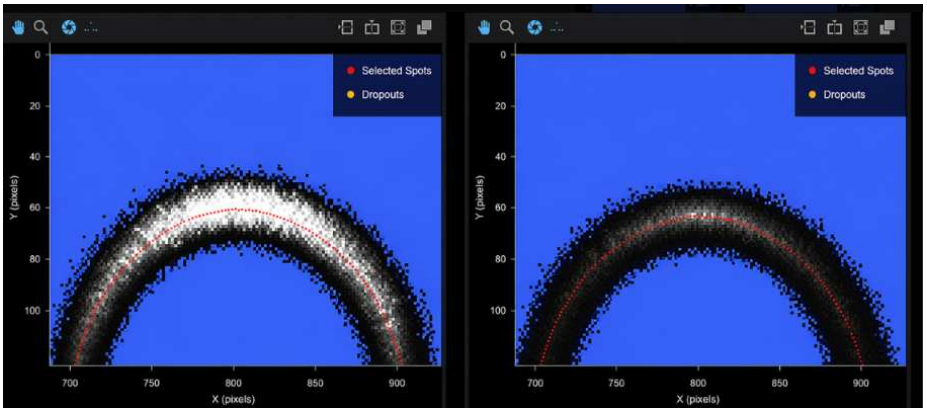

Figure 3.11: Experimental comparison of different exposure settings on the tool shank: high exposure (left) and low exposure (right).

A particularly useful option that emerged during this phase was the *multiple exposure* mode available in GoPxL. For the Gocator family of laser line profilers, LMI specifies that the sensor can combine data acquired at different exposure levels to generate a single composite profile, a solution specifically intended for surfaces exhibiting non-uniform reflectance within the same scan. Up to five exposure levels can be defined, and for each of them the sensor performs a complete scan; as a consequence, the use of multiple exposures reduces the effective acquisition frequency. The final profile is created by combining the data collected at the different exposure levels and selecting, where available, the profile data from the lowest-numbered exposure step. For this reason, progressively higher exposure values should be assigned to the subsequent steps [33].

From an experimental point of view, this functionality proved particularly advantageous, since it allowed a more effective management of the strong signal variability along the shank profile. In practice, shorter exposures limited saturation in the most reflective regions, whereas longer exposures preserved a sufficient signal level in areas where the optical return was weaker. By adopting the multiple-exposure configuration, it was finally possible to obtain an acquisition condition in which, the balance between saturated and non-saturated pixels was sufficiently effective to enable the reliable export of the profiles that were subsequently analysed in MATLAB.

Signal Saturation and Peak Extraction Algorithms

The choice of an optimal exposure strategy is not merely a practical adjustment to improve profile continuity; it is fundamentally rooted in the mathematical nature of the sensor's measurement process. When a portion of the CMOS sensor is struck by excessively high light intensity, pixel saturation occurs. This phenomenon leads to a deformation of the acquired laser spot profile: the light intensity no longer follows an ideal Gaussian distribution but instead exhibits a "plateau" where several adjacent pixels reach their maximum saturation value.

This distortion directly affects the **Center of Gravity (CoG)** algorithm used by the Gocator 2520 to locate the spot centroid with sub-pixel precision [34]. Mathematically, the sensor calculates the point's position $\bar{z}$ as the weighted average of the intensity of the involved pixels:

$$\bar{z} = \frac{\sum(I_i \cdot z_i)}{\sum I_i} \tag{3.13}$$

In the presence of saturation, the loss of the central peak makes the determination of $\bar{z}$ uncertain, as the algorithm must operate on a flattened intensity distribution. The metrological consequence of this uncertainty is an increase in spatial noise ($\sigma_{spatial}$) and the appearance of "unstable" points or outliers that deviate from the ideal geometric model. Interestingly, these errors are strictly linked to the specific local micro-geometry of the surface (which generates the same reflection pattern in every frame), explaining why the system maintains high temporal repeatability despite the localized spatial uncertainty.

3.4.2 Profile Visualization and Circular Reference Fitting

Once the optimal exposure parameters were identified via the GoPxL interface, the acquired profiles were exported in .csv format for quantitative metrological assessment. To analyze the fidelity of the tool shank reconstruction, a dedicated MATLAB algorithm was developed for the visualization and geometric fitting of the circular section.

The primary objective of this procedure is to extract an ideal mathematical model (a circle) from the experimental point cloud which, by its nature, represents only a portion (approximately a semi-circumference) of the shank as observed by the sensor.

The Fitting Algorithm: The Kåsa Method

The Kåsa method was adopted for the fitting process, providing a computationally efficient approach to approximate a set of points (x, z) to a circle. Unlike iterative non-linear optimization methods, which require significant computational resources and an initial guess for the parameters, this method linearizes the canonical circle equation:

$$(x - x_c)^2 + (z - z_c)^2 = R^2 \tag{3.14}$$

transforming it into the algebraic form:

$$x^2 + z^2 + ax + bz + c = 0 \tag{3.15}$$

where the parameters a, b, c are directly related to the center coordinates (x_c, z_c) and the radius R [35]. This formulation allows the problem to be solved efficiently using the linear least-squares method.

Implementation and Visualization

The core of the developed algorithm constructs the system matrix and solves it to derive the geometric parameters. A critical aspect of the visualization is the setting of a 1:1 aspect ratio (`daspect([1 1 1])`), which is essential to avoid anamorphic distortions that would visually transform the circle into an ellipse, hindering a direct evaluation of the fit quality.

The following MATLAB code snippet illustrates the implementation of the core calculation:

Listing 3.2: Implementation of the Kåsa circular fitting method.

```
% --- K sa Method Implementation ---
% x, z are the coordinates extracted from experimental data
n = numel(x);

% Construction of the linear system matrix A*p = b
Aeq  = [x, z, ones(n,1)];
bvec = -(x.^2 + z.^2);

% Solving the system via the backslash operator (least-squares)
abc  = Aeq \ bvec;
a = abc(1); b = abc(2); c = abc(3);

% Extraction of geometric parameters (Center and Radius)
xc = -a/2;
zc = -b/2;
R  = sqrt(max(0, (a^2 + b^2)/4 - c));
```

This procedure provides a stable and objective geometric reference, which is indispensable for the subsequent analyses concerning point dispersion and the overall quality of the data acquired by the sensor.

The result of this fitting process is graphically represented in Figure 3.12, which displays the acquired points of a 6-mm-diameter tool shank color-coded according to their absolute radial residual. The visualization confirms that the Kåsa algorithm effectively reconstructs the circular profile, providing a baseline to isolate the systematic measurement errors discussed in the previous section. By decoupling the nominal geometry from the sensor noise, it becomes possible to quantify the local deviations caused by surface reflectivity and saturation.

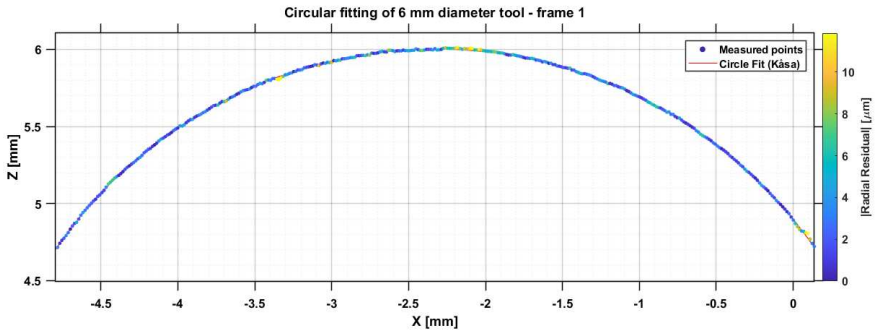

Figure 3.12: Circular fitting of a 6-mm-diameter tool shank (Frame 1).

Having established a robust fitting methodology and evaluated the individ-

ual profile quality, the analysis will now shift toward assessing the repeatability of the measurement system across multiple scans to determine the statistical stability of the extracted geometric parameters.

3.4.3 Residual Error Analysis

Once the best-fit circle has been estimated using the Kåsa method, the quality of the acquired profile can be evaluated through the analysis of the residuals, defined as the radial deviations between the measured points and the fitted geometric reference. This procedure allows for the separation of the global geometric form of the tool shank from local signal fluctuations and measurement noise.

Let $P_i = (x_i, z_i)$ be a measured point and $C = (x_c, z_c)$ be the center of the fitted circle with radius R. The radial residual r_i is defined as the difference between the Euclidean distance of the point from the center and the estimated radius:

$$r_i = \sqrt{(x_i - x_c)^2 + (z_i - z_c)^2} - R \tag{3.16}$$

By removing the macroscopic cylindrical component, the residuals describe only the local deviations of the acquired points. For the first frame of the 6 diameter tool, the residual analysis (considering the filtered region $Z \geq 4.8$ mm) yielded the following statistical indicators:

- **Mean Absolute Error (MAE)**: 3.34 μm;
- **Root Mean Square Error (RMSE)**: 4.41 μm;
- **Standard deviation of the residuals** (σ_{spatial}): 4.41 μm.

These values confirm the high metrological quality of the single acquisition. The coincidence between the RMSE and the spatial standard deviation indicates that the residuals are correctly centered around zero, validating the effectiveness of the least-squares fitting approach.

The residual histogram (Figure 3.13) provides a complementary statistical view. The distribution exhibits a bell-shaped form centered at zero, which is characteristic of a measurement process dominated by random stochastic noise. The concentration of the majority of points within a ± 10 μm interval

demonstrates that the sensor maintains high spatial precision Despite its cylindrical shape and the high reflectivity of the polished metal

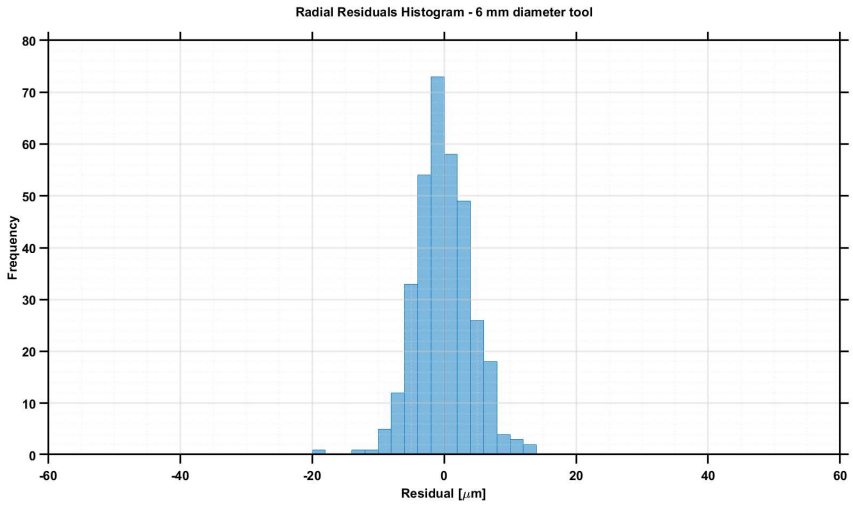

Figure 3.13: Frequency histogram of the radial residuals for Frame 1 acquired on the 6 mm diameter tool shank.

3.4.4 Temporal Analysis

To evaluate the *temporal repeatability* of the measurement system, ten consecutive acquisitions were analysed under nominally identical operating conditions.

From a qualitative standpoint, the profiles appear almost indistinguishable and largely superimposed. In particular, the regions characterized by larger residuals with respect to the fitted circle—often associated with optical artifacts or micro-scale surface irregularities—systematically reappear at the same angular positions in all acquired frames. This behaviour suggests that a significant portion of the observed deviations is not caused by purely random sensor fluctuations, but rather by systematic effects related to the interaction between the laser beam and the cylindrical geometry of the workpiece.

For a quantitative assessment, the *point-wise temporal standard deviation* σ_t was computed for each point of the profile. The distribution of this quantity over the entire set of acquired points is shown in Figure **??**, where the vertical bars represent the oscillation of the Z coordinate at the corresponding positions along X.

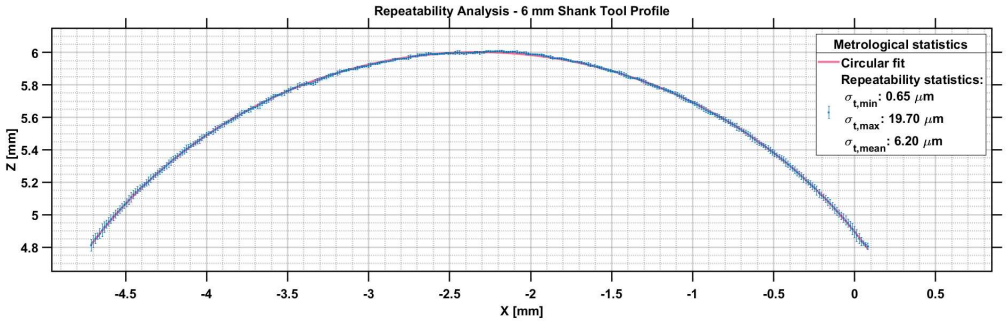

Figure 3.14: Mean profile with temporal variability

The aggregated statistics obtained over the entire analysed profile are reported below:

- $\sigma_{\mathbf{temporal,min}} = 0.65$ μm;
- $\sigma_{\mathbf{temporal,max}} = 19.70$ μm;
- $\sigma_{\mathbf{temporal,mean}} = 6.20$ μm.

The maximum value is localized in correspondence with the high-slope lateral flanks. These values, which are significantly higher than those obtained in the gauge block experiments, provided a more comprehensive understanding of the sensor behaviour when measuring the cylindrical profile of the shank. In particular, they highlight how the measurement response is strongly influenced by the local surface orientation, especially in those regions where the geometry changes more abruptly and the angle of incidence becomes less favourable.

A local analysis, carried out separately on the top region and on the lateral regions, revealed two clearly distinct behaviours:

- **Top region:** In the upper portion of the shank, i.e. the area directly underneath the sensor, the single-profile analysis had previously shown the largest deviations from the fitted circle. This initially suggested that reflection phenomena and signal saturation might affect the accurate localization of the measured points. Such an interpretation is

consistent with the observations made in GoPxL: as the exposure settings are varied, the first areas to exhibit saturation are systematically the topmost ones. However, the temporal analysis reveals an important aspect. Although the points in this region are locally biased with respect to the ideal fitted circumference, they tend to reappear in stable positions from one acquisition to the next. In other words, the upper region exhibits a local positional bias relative to the geometric model, while still maintaining good temporal repeatability. This indicates that the dominant source of error in this area is not random fluctuation, but rather a systematic offset that persists consistently across repeated measurements.

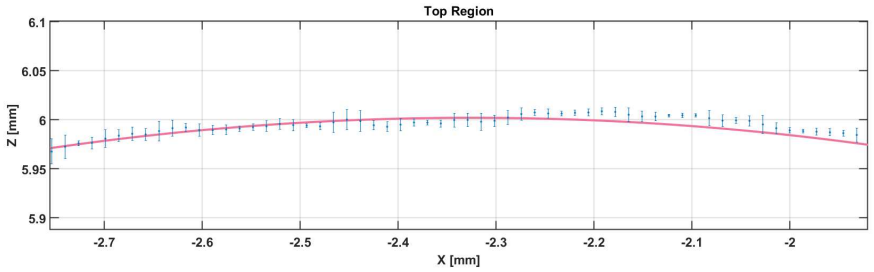

Figure 3.15: Zoom of the profile top region

- **Lateral regions:** By contrast, the lateral regions, despite being characterized by more favourable exposure conditions and lower saturation effects, exhibit a significant increase in variability between successive acquisitions. This behaviour can be attributed to the so-called *slope-induced noise*. This phenomenon arises from the fixed-grid sampling mechanism of the sensor: very small variations in the estimation of the laser profile centroid, i.e. centroid jitter, produce shifts in the X coordinate on the order of fractions of a micrometre between consecutive scans. While this effect remains negligible on nearly horizontal surfaces, it becomes significantly amplified along steep flanks, where even a microscopic lateral displacement translates into a variation of

several micrometres in the Z coordinate. Therefore, the increase in temporal standard deviation observed in the lateral regions should not be interpreted as a sensor malfunction, but rather as an intrinsic limitation of laser triangulation when measuring highly curved and steeply inclined surfaces.

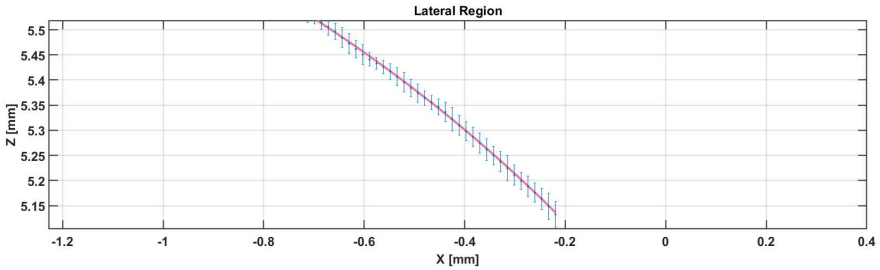

Figure 3.16: Close-up of the profile lateral flank

In light of these observations, the overall performance of the system can still be considered satisfactory with respect to the final objective of the 3D reconstruction. Although the measured deviations exceed the nominal values reported in the sensor datasheet, the magnitude of the error remains within acceptable limits for the intended application. In particular, the reconstruction accuracy can be improved by restricting the region of interest (ROI) to those portions of the profile that are less affected by temporal fluctuations. This strategy makes it possible to reduce the influence of lateral variability and, consequently, to limit the propagation of measurement errors in the subsequent processing stages.

3.4.5 Comparative Analysis Across Different Industrial Tools

Following the characterization of the main physical limitations and geometric distortions affecting the measurement process, the analysis was extended to evaluate the metrological reliability of the mathematical fitting procedure

under real operating conditions. To assess both dimensional accuracy and repeatability in a rigorous manner, an experimental campaign was carried out on five different industrial tools. For each tool, the circular fitting algorithm was applied to ten consecutive scans, allowing the extraction of the estimated radius and the evaluation of its temporal stability.

The obtained values were then compared with the nominal dimensions provided by the manufacturer specifications. The complete results of this experimental phase are reported in Table 3.4, which provides an objective assessment of the sensor performance under realistic measurement conditions. It should be emphasized that the values reported as $\sigma_{spatial}$ are included only as reference values computed with respect to the first frame, and therefore they should not be interpreted as a global indicator of measurement stability. Conversely, σ_{temp} represents the actual temporal repeatability evaluated over the entire set of repeated acquisitions.

Table 3.4: Comparison of estimated radii (R_{est}), nominal radii (R_{nom}), reference spatial deviations with respect to the first frame, and temporal standard deviations for the analyzed tools.

Tool	**Est. Radius [mm]**	**Nom. Radius [mm]**	$\sigma_{spatial}$ [μm]	σ_{temp} [μm]
Tool 1	2.9972	3.00	3.65	3.60
Tool 2	3.7097	3.75	7.18	2.21
Tool 3	5.9766	6.00	4.56	6.98
Tool 4	4.9848	5.00	8.40	11.71
Tool 5	2.9970	3.00	4.40	6.20

The comparative analysis leads to the following observations:

- **Dimensional Accuracy**: The estimated radius for each tool shows a limited deviation from the corresponding nominal value. Even in the case of the 6 mm tool (Tool 3), where the cylindrical geometry introduces more challenging measurement conditions, the radius estimation remains close to the nominal dimension. This result confirms the suitability of the Kåsa circle fitting algorithm for the reconstruction of cylindrical shank profiles.
- **Measurement Stability**: The temporal standard deviation, σ_{temp}, remains within a few micrometres for most of the analyzed tools.

Higher values are observed for Tools 3, 4, and 5, and can be attributed to the combined effect of surface finish, local curvature, and *slope-induced noise* along the lateral flanks. These effects had already been identified in the previous repeatability analysis and should therefore be interpreted as systematic measurement limitations rather than as symptoms of intrinsic sensor instability.

- **Fitting Reliability**: Although $\sigma_{spatial}$ is reported only as a frame-to-frame reference quantity with respect to the first acquisition, the overall consistency of the fitted radii across repeated scans confirms the robustness of the least-squares fitting approach. The method provides a stable geometric reference over different tool diameters, despite the presence of local signal fluctuations and optical disturbances.

Overall, the tests performed on real industrial tools confirm that the proposed measurement approach provides sufficient precision for wear monitoring applications. Although the measurements are influenced by surface finish, local curvature, and optical effects inherent to laser triangulation, the observed deviations remain within acceptable limits for the intended application. Therefore, the system can be considered a reliable reference for the subsequent three-dimensional geometric characterization of the analyzed tools.

Chapter 4

3D Tool Reconstruction

Following the preliminary activities carried out at iMAGE S, aimed at characterizing the sensor performance on gauge blocks and cutting tools under static conditions, the project entered its most significant phase, namely the evaluation of the integration of three-dimensional acquisition technologies into Speroni industrial presetting machines. Transferring the experimental activity to an industrial environment made it possible to operate on a high-precision mechanical platform, taking advantage of the machine's micrometric positioning stability and of custom-designed brackets for sensor mounting.

At this stage, the research was structured into two complementary lines of work developed in parallel. The first, carried out mainly by my colleague, concerned the two-dimensional analysis of the main geometric parameters of the cutting tool. The second, which constitutes the core of the present chapter and represents my main contribution, concerned the development of procedures for the three-dimensional reconstruction of the tool from acquisitions obtained from different viewpoints.

Compared with the initial setup of the work, this activity was progressively expanded to include the evaluation of two different optical 3D acquisition technologies: on the one hand, laser triangulation, which had already been studied extensively during the period spent at iMAGE S, and on the other hand, snapshot structured light, which became available only at a later stage of the project. Consequently, the present chapter does not limit itself to describing the 3D reconstruction methodology developed for the laser-

triangulation sensor, but also presents the most significant results obtained with the snapshot sensor, still within the framework of three-dimensional reconstruction, discussing its behaviour in the industrial context and comparing the results obtained with these two technologies.

In order to make such a comparison possible, it was necessary to define acquisition methods consistent with the operating principle of each technology, to analyse the optical occlusions induced by the complex geometry of cutting tools, and to develop data-processing strategies aimed at filtering, registering, and merging the acquired point clouds. In the case of laser triangulation, this required the definition of a sequential scanning procedure for the tool and a dedicated processing pipeline; in the case of snapshot structured light, the general approach remained similar, but the acquisition mode proved to be more immediate, since the three-dimensional data were acquired directly through a single snapshot, without the need to move the sensor during the scan, as was instead required in the case of laser triangulation.

4.1 Hardware Integration and System Setup

As already discussed in the previous chapter, the transition from static tests to full 3D reconstruction required a significant improvement in motion control. At this stage, rather than relying on an absolute machine coordinate system, which would have been difficult to apply because of the provisional sensor mounting, not perfectly centred with respect to the native machine axes, it was essential to guarantee extremely high precision in the relative movements. The adopted procedure consisted in verifying the correct framing of the tool, clamped on the rotating spindle and observed through the GoPxL visual interface. Once this starting position had been defined and recorded, the alignment calculations between scans were based on the subsequent relative displacements.

In order to ensure micrometric precision in these movements, the experimental phase was carried out using the **Speroni STP FUTURA**, an industrial presetting machine that provided a much more solid and reliable metrological basis than that available on a conventional laboratory bench. This platform made it possible to control both sensor translations and tool

rotation with high precision, which was essential for correctly merging the different acquisitions without introducing geometric errors into the final model.

In addition to the laser-triangulation sensor already described in the previous chapter, this phase of the project also made it possible to use the **Gocator 3506**, a snapshot sensor based on blue-LED structured light and a dual-camera stereo configuration. Unlike the laser profiler, which acquires 3D data profile by profile during continuous motion, the Gocator 3506 directly captures the entire observed area in a single snapshot. This approach makes it particularly suitable for stationary objects or for applications in which movement occurs in a stop-and-go fashion. The main nominal specifications of the Gocator 3506 are summarized in Table 4.1.

Table 4.1: Main nominal specifications of the Gocator 3506. Adapted from the manufacturer datasheet.

Parameter	**Nominal value**
Scan rate	3 Hz
Imager resolution	5 MP
Clearance distance (CD)	87 mm
Measurement range (MR)	25 mm
Field of view (FOV)	27 × 45 – 30 × 45 mm
Z repeatability	2.0 μm
XY resolution	20–25 μm
VDE accuracy	0.012 mm
Dimensions	49 × 136 × 170 mm
Weight	1.52 kg

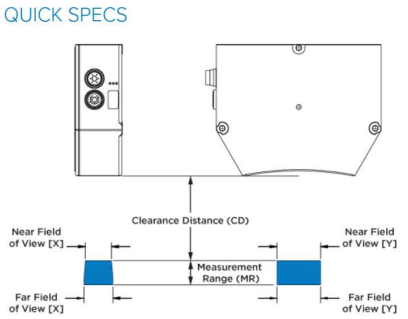

Due to delays in the sensor delivery by the supplier, it was not possible to carry out on the Gocator 3506 a preliminary testing phase at the iMAGE S comparable to that performed on the laser-triangulation sensor. Its evaluation therefore took place directly during the industrial phase, once the sensor had been installed on the Speroni machine. Despite this limitation, it was still possible to perform significant acquisitions, sufficient to obtain an initial assessment of its performance in the real application context and to compare its behaviour with that of the laser-triangulation sensor.

To enable this comparison, both devices were mounted independently on the mobile column of the machine, adopting two different configurations on the

same platform. Figure 4.1 shows the two experimental arrangements considered in this work: on the left, the laser-triangulation sensor configuration, in which the device was oriented to project the laser plane horizontally while scanning the tool through the vertical motion of the column; on the right, the configuration adopted for the Gocator 3506 snapshot sensor, designed to align the stereo cameras frontally with the tool profile and optimize the field of view for static single-shot acquisitions.

Figure 4.1: Experimental sensor configurations on the Speroni STP FUTURA: laser triangulation (left) and Gocator 3506 snapshot setup (right).

Machine Axes and Kinematic Configuration

In order to obtain accurate 3D acquisitions, it was necessary to refer to the machine coordinate system. The STP FUTURA workstation manages motion through four main axes:

- **R-axis**, which controls the radial forward–backward movement of the mobile support on which the sensor is mounted;
- **Z-axis**, which controls the vertical displacement of the column;
- **Y-axis**, which controls lateral positioning;
- **A-axis**, which controls the high-precision rotation of the tool spindle.

This configuration made it possible to control the sensor viewpoint with respect to the tool and proved fundamental both for 3D reconstruction based on sequential scanning and for the evaluation of the acquisitions performed with the snapshot sensor.

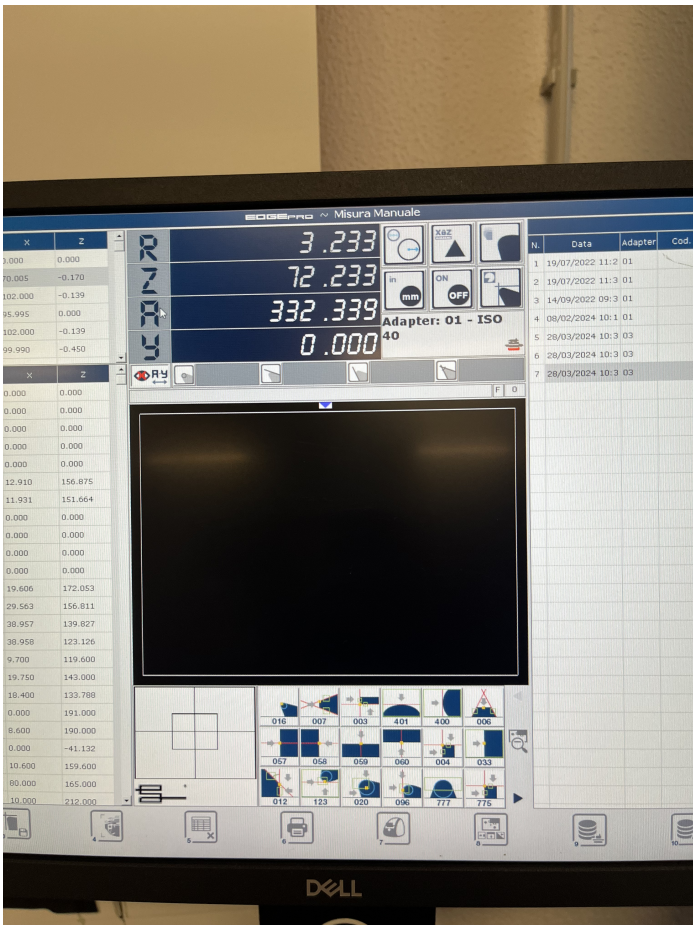

Figure 4.2: Visualization of the workstation axes and of the tool–spindle alignment area.

Spindle Precision and Rotational Accuracy (A-axis)

In 3D reconstruction, spindle rotational precision, i.e. the *run-out* of the A-axis, is a key factor. If the spindle does not rotate exactly about its theoretical axis, the tool may become misaligned between acquisitions, introducing eccentricity errors when merging data from different viewpoints. The STP FUTURA has a high-precision spindle with very low concentricity error, allowing the A-axis to be treated as a stable reference for the roto-translation algorithms developed in MATLAB and, more generally, for acquisitions requiring geometric consistency between views.

Z-axis Motion and Sampling Synchronization

A particularly important aspect concerned the synchronization between the vertical movement of the column, i.e. the Z-axis, and the acquisition frequency of the laser-triangulation sensor. It was necessary to calibrate the translation speed accurately with respect to the profiler frame rate, in order to guarantee a constant sampling pitch. Any variation in speed or any incorrect frequency setting would have introduced axial distortion in the reconstructed 3D model. Thanks to the motion control provided by the machine, it was possible to maintain a constant feed rate and to obtain regular sampling of the laser profiles.

In the case of the snapshot sensor, this problem does not exist, because the acquisition does not take place through continuous profile-by-profile scanning, but through individual snapshots of the observed area. Nevertheless, machine stability remains essential also in this case, since it guarantees the correct relative positioning between sensor and tool and improves the repeatability of the acquisitions.

Custom Sensor Mounting and Stability

The hardware integration was completed through dedicated mounting brackets designed to rigidly secure both sensors to the machine's moving column. For the laser-triangulation sensor, this ensured a stable laser plane and a known angle with respect to the tool, both essential for geometrically consistent acquisitions. The snapshot sensor likewise required a stable and repeatable mount to preserve the observation geometry during acquisition.

The presetter was thus converted into a high-performance 3D scanning station, where the rigidity of the mechanical interface reduced vibrations and improved measurement reliability. On this basis, the two acquisition strategies examined in this chapter were developed and assessed: motion-based reconstruction by laser triangulation and snapshot-based 3D acquisition by structured light.

4.2 Optical Limitations and Artifacts

In order to achieve a more comprehensive understanding of the capabilities and limitations of the two optical technologies considered, a comparative analysis of individual three-dimensional acquisitions was carried out. The aim of this phase was to directly assess the reconstructed surface quality, the presence of optical occlusions, reflection-induced artifacts, and the influence of tool geometry on the overall reliability of the acquired data. As a primary case study, a 12 mm diameter ball-nose tool was selected, since its geometry, while still including curved surfaces and well-defined cutting regions, is more favourable than that of smaller tools or tools characterized by tighter helical features.

The analysis was organized on two complementary levels. First, the full acquisition of the tool was considered, in order to highlight differences in surface coverage, point-cloud continuity, and the presence of optically critical regions. Subsequently, attention was focused on the cylindrical shank, which represents a geometrically simple and a priori known surface, particularly suitable for a quantitative assessment of point dispersion and of the apparent surface quality of the reconstruction.

Qualitative Comparison of Full Acquisitions

The first comparison was performed by considering two acquisitions of the same 12 mm ball-nose tool, obtained as far as possible from the same side of the tool: one using laser triangulation and the other using the snapshot structured-light sensor. This comparison makes it possible to directly observe how the two technologies describe the overall geometry of the tool before any multi-view registration or merging procedure is applied.

As can be observed in Figure 4.3, both technologies are capable of providing a useful three-dimensional representation of the tool, although with clear differences in the quality of the raw data. In the case of laser triangulation, the surface appears globally more continuous, regular, and clean. The visible regions are sampled with good density, and the surface noise remains limited even in areas that are more exposed to reflections. The main loss of information is concentrated in the regions that are recessed with respect to the sensor line of sight, particularly where local orientation or geome-

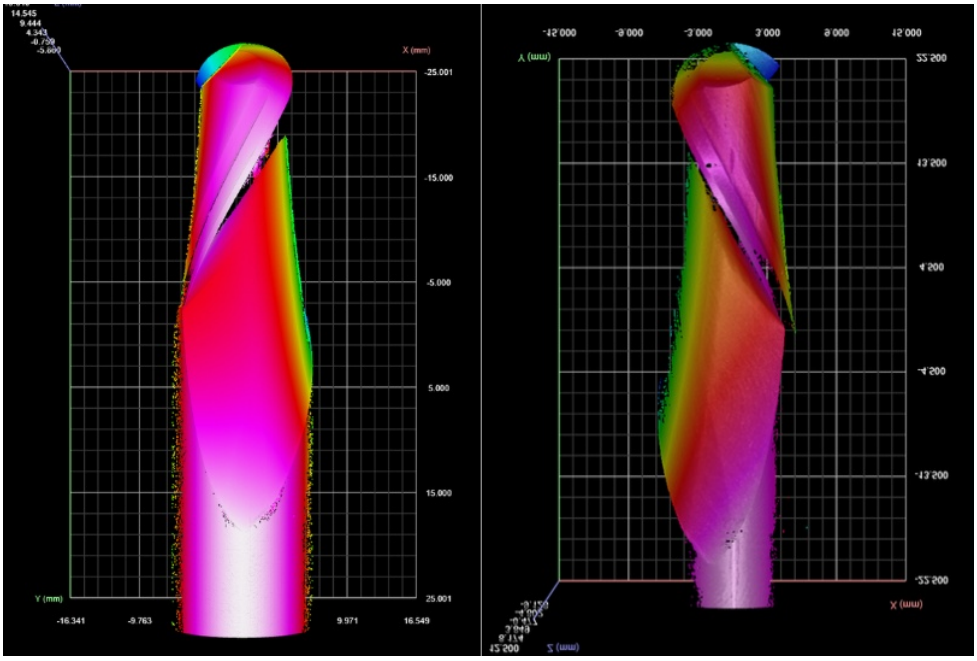

Figure 4.3: Comparison between the full acquisitions of a 12 mm ball-nose tool obtained by laser triangulation and snapshot structured light.

try gives rise to optical shadowing or partial screening of the incident and reflected signal.

In the case of the snapshot structured-light sensor, the global geometry of the tool remains clearly recognizable, although some limitations become more evident when compared with the laser-based acquisition. In particular, the acquisition returns a smaller overall number of points and tends to exhibit a non-uniform point distribution along the lateral boundaries of the observed surface. Moreover, some small local voids can be observed, that is, regions in which points are missing despite the fact that the surrounding surface has been acquired. Such anomalies are plausibly related to local optical phenomena, such as specular reflections or unfavourable illumination and viewing conditions.

Despite these inaccuracies, the acquisition produced by the snapshot sensor still preserves a good readability of the overall tool geometry. The cutting edges, slope variations, and general profile of the tool are in fact clearly visible and, at first visual inspection, may in some cases even appear more pronounced than in the corresponding laser-triangulation acquisition. However, this initial impression is partly due to the different way in which the

surface is rendered by the sensor and does not necessarily correspond to a better metrological quality of the acquired data.

Overall, this first analysis therefore shows that laser triangulation provides raw data that are generally cleaner and more stable, whereas snapshot structured light, although effective in representing the global shape of the tool, requires greater caution when the analysis shifts from a purely morphological interpretation to a finer assessment of the acquired surface quality. In both cases, however, the individual acquisitions are sufficiently informative to serve as the basis for a subsequent complete reconstruction through scans obtained from different viewpoints.

Point Dispersion on the Cylindrical Shank

In order to make the comparison between the two sensors more meaningful also from a quantitative point of view, a portion of the cylindrical shank of the tool was selected. This region represents a particularly suitable reference for the analysis, because its nominal shape is simple, known a priori, and less affected by the morphological complexity typical of the cutting region. Moreover, since this portion is intended for clamping on the spindle, it should ideally exhibit a substantially cylindrical shape.

The purpose of this analysis is not to estimate surface roughness in the strict metrological sense, but rather to evaluate the *dispersion of the acquired points with respect to a cylindrical reference surface*, thus providing a comparative measure of the apparent surface quality of the reconstruction.

For each sensor, a limited portion of the shank was therefore isolated and the fitting method developed in this work was applied to it. This approach is conceptually consistent with the procedure already adopted in the previous chapter during the static analysis of individual profiles, but extends it to a wider three-dimensional region. More specifically, instead of operating on a single profile only, the cylindrical portion was subdivided into multiple transverse sections distributed along the shank axis; for each of them, a circle was fitted, and from the set of the resulting centres and radii a representative cylinder was reconstructed for the actually acquired surface. In order to avoid unnecessary computational burden, the fitting was not performed on every available section, but rather on a regular subsampling

of profiles, still sufficient to describe the local surface trend in a realistic manner.

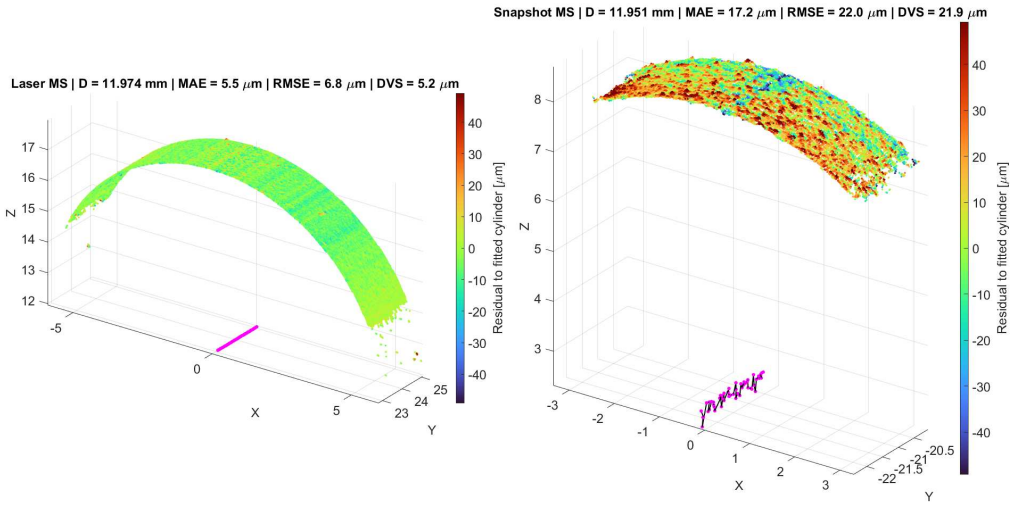

Figure 4.4: Three-dimensional distribution of the point residuals with respect to the fitted cylinder on the cylindrical shank portion.

Figure 4.4 shows, for each sensor, the three-dimensional distribution of the residuals with respect to the fitted cylinder. The colour map makes it possible to directly visualize the local deviation of the acquired points from the fitted reference surface: a more compact and uniform colour distribution indicates a more stable reconstruction, whereas larger excursions indicate a greater dispersion of the data. In the case of laser triangulation, the points are distributed much more regularly around the fitted cylindrical reference, with generally limited deviations. In the case of the snapshot sensor, on the contrary, the dispersion appears more pronounced and less uniform, thus confirming a greater sensitivity to surface noise and local artifacts.

Immediately after this figure, it is convenient to report the main numerical indicators associated with the fitted cylindrical segment.

Table 4.2: Quantitative indicators of point dispersion on the cylindrical shank portion.

Sensor	**Fitted diam. [mm]**	**MAE [μm]**	**RMSE [μm]**	**Spatial DVS [μm]**
Laser triang.	11.974	5.5	6.8	5.2
Snapshot SL	11.951	17.2	22.0	21.9

The values reported in Table 4.2 show that the indicators associated with

laser triangulation are very close to those already obtained in the previous chapter during the static analysis of a single profile, which provides an important indication of the internal consistency of the adopted methodology. In other words, the multi-section approach employed here may be interpreted as a three-dimensional extension of the previous static analysis: rather than evaluating a single profile only, the same type of assessment is reproduced over a wider surface portion, while preserving a fitting logic based on local circular cross-sections.

In order to support the interpretation of the three-dimensional residual map, a residual histogram with respect to the corresponding fitted cylinders was also constructed. This graph makes it possible to observe the statistical distribution of the deviations and to compare the quality of the two acquisitions in a more immediate way. A narrower distribution concentrated around zero indicates a lower dispersion of the points and therefore a more stable reconstruction, whereas a broader distribution with more extended tails is a sign of a noisier reconstructed surface.

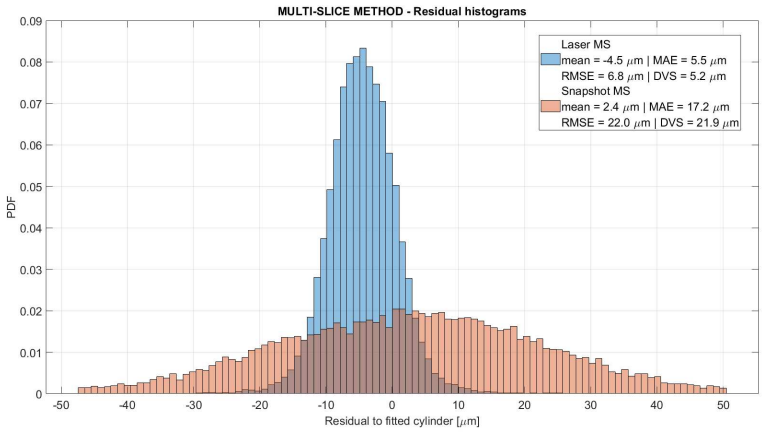

Figure 4.5: Comparative histogram of the residuals with respect to the fitted cylinders for the cylindrical shank portion acquired by laser triangulation and by the snapshot sensor.

The histogram in Figure 4.5 confirms the trend already observed in the three-dimensional map: laser triangulation yields a narrower distribution centered around zero, whereas the snapshot sensor produces a wider and more dispersed one. This indicates that laser triangulation provides a more stable and accurate acquisition on the cylindrical surface, while the snapshot

sensor, despite yielding a plausible fitted diameter, exhibits higher spatial variability.

This quantitative analysis confirms a key aspect already noted in the full tool scans: although the snapshot sensor may better highlight cutting edges, slope variations, and overall profiles, laser triangulation provides clearly superior micrometric surface regularity. Global geometric readability and local metrological quality do not necessarily coincide, making the combined use of three-dimensional residual maps and statistical residual distributions particularly informative.

Influence of Geometry, Size, and Surface Reflectivity

Beyond the intrinsic differences between the two technologies, acquisition quality is strongly affected by tool geometry, size, and material optical properties. To highlight this aspect, two complementary cases were analysed: a larger twist drill, with low reflectivity and a relatively favourable geometry, and a small polished end mill, with reduced dimensions and a more critical helical shape. In both cases, acquisitions obtained by laser triangulation and by the snapshot structured-light sensor were directly compared, together with a photograph of the real tool used as a visual reference.

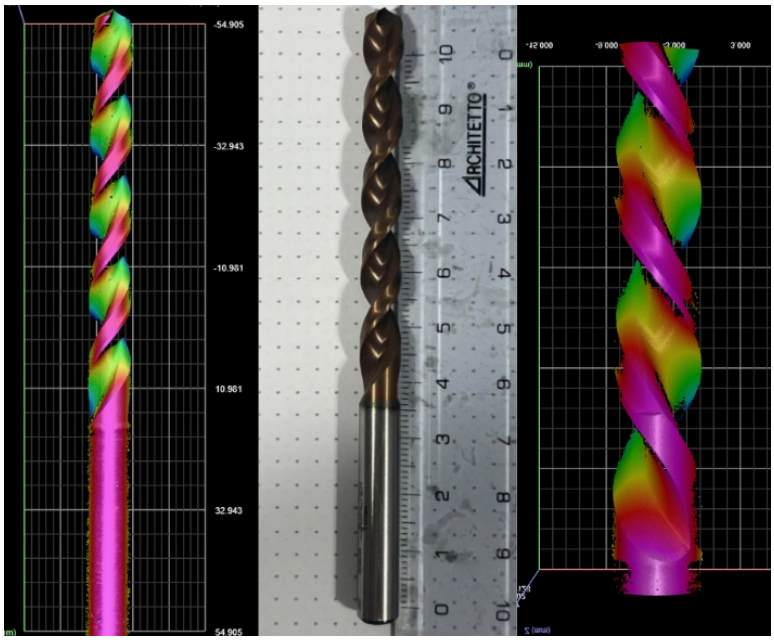

Figure 4.6: Comparison between the acquisitions of a large low-reflectivity twist drill obtained by laser triangulation and by the snapshot sensor

In the first case, a relatively long twist drill with a low-reflectivity surface and a sufficiently open geometry was considered. Under these conditions, both technologies are able to provide an overall satisfactory representation of the tool, although with significant differences in the way the surface is acquired.

Laser triangulation performs particularly well in this configuration. Since the acquisition takes place during the relative motion between sensor and tool, the system is able to cover the entire length of the tool, without being restricted to the instantaneous field of view of the sensor. Moreover, because the object is relatively large and its surface is not excessively reflective, the resulting point cloud appears continuous, sufficiently dense, and free from major gaps or discontinuities. The cutting edges are clearly recognizable and the general drill geometry is reconstructed in a convincing way. Some missing regions are naturally still present in the recessed helical portions, particularly near the rake angle and in the areas that are hidden from the sensor line of sight; however, this is a physiological optical limitation, due to the impossibility of observing such surfaces without changing the acquisition angle.

The acquisition obtained by the snapshot sensor exhibits a different limitation. Unlike laser triangulation, the sensor does not perform a continuous scan along the tool, but acquires in a single shot only the portion that falls within its field of view and within the corresponding useful measurement volume. As a consequence, a tool approximately 11 cm long cannot be fully captured in a single acquisition, and this represents an important limitation of this technology when long tools are considered. A complete reconstruction would therefore require multiple acquisitions followed by registration and merging, with an inevitable increase in operational complexity.

If the analysis is restricted to the single available acquisition, however, the snapshot sensor still returns a fairly good amount of information. It is plausible that the lower reflectivity of the tool facilitates the acquisition process, allowing the sensor to describe a sufficiently wide portion of the observed surface. Nevertheless, some local smearing and small voids are still visible, especially in regions of higher curvature and underneath the cutting edges, where the combination of local slope, optical shadowing, and

reflections makes the acquired data less stable. Overall, for this first case, laser triangulation therefore provides the better result, both in terms of the extent of the acquired area and in terms of continuity and cleanliness of the reconstruction.

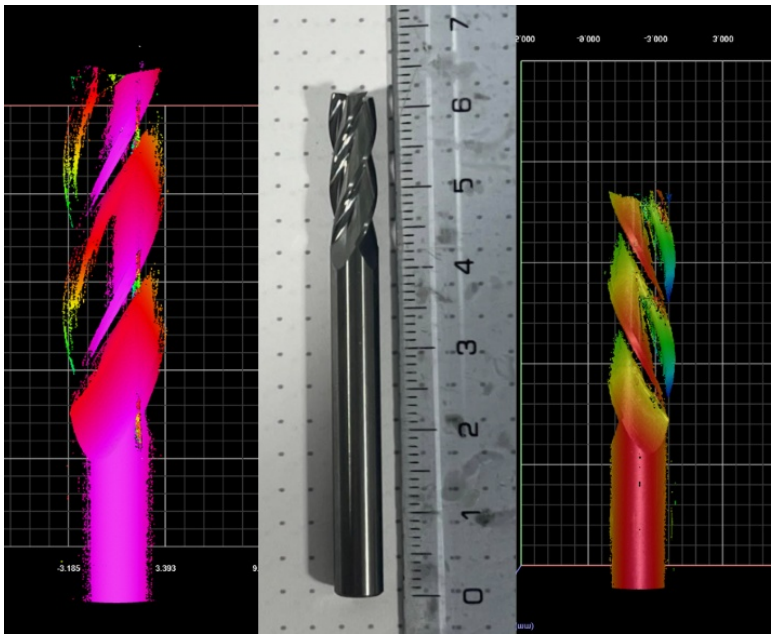

Figure 4.7: Comparison between the acquisitions of a small polished end mill obtained by laser triangulation and by the snapshot sensor

The second case concerns a small polished end mill, characterized by reduced dimensions, high surface reflectivity, and a more difficult helical geometry. In this scenario, the comparison between the two technologies leads to a different conclusion from that observed in the previous case.

Laser triangulation, although still yielding a readable geometry, produces a sparser and less continuous scan. In this case, the combination of reduced dimensions, strong metallic reflectivity, and tighter helical geometry penalizes the acquisition process. The resulting point cloud is less dense, and some regions are described in a less stable way, indicating that the sensor struggles to maintain continuity and signal quality on such small and optically challenging surfaces. It is plausible that a different optimization of the acquisition parameters could partially improve the result, but the observed behaviour nevertheless confirms the greater criticality of this case.

The snapshot sensor, on the contrary, performs relatively better in this con-

figuration. Since the tool more easily fits within the available measurement volume, the sensor can exploit its acquisition principle more effectively and returns a representation richer in detail than that obtained by laser triangulation. The general morphology of the tool, the helical layout, and several geometric details are clearly visible, to the point that, in this specific case, the snapshot acquisition appears overall more convincing than the corresponding laser-based one. This suggests that, for geometries that are not excessively large and that are fully compatible with the available measurement volume, snapshot structured light may constitute a valid and competitive solution.

This twofold comparison therefore leads to an important result: neither technology can be regarded as universally superior in an absolute sense, since performance strongly depends on the type of tool under consideration. Laser triangulation proves particularly effective for larger tools, developed in length and characterized by surfaces that are not excessively reflective, thanks to the possibility of scanning the entire object in motion with good continuity. The snapshot sensor, on the other hand, shows its strengths in the case of smaller tools, which fit completely within the measurement volume and for which the speed and completeness of the single-shot acquisition can be exploited more effectively.

More generally, the comparison confirms that size, reflectivity, and helical geometry decisively influence reconstruction quality. As surface reflectivity increases and the characteristic dimensions of the tool decrease, the probability of obtaining discontinuous point clouds, local gaps, and less stable point distributions also increases. Similarly, strongly inclined surfaces or recessed regions with respect to the sensor line of sight tend to generate occlusions and loss of information, regardless of the technology employed, albeit with different manifestations in the two cases.

Overall, these observations reinforce the idea that both technologies can be effective, provided that they are employed in the context most suited to their respective characteristics. Laser triangulation offers greater continuity and reliability in the scanning of elongated tools that are relatively favourable from an optical point of view, whereas the snapshot sensor proves particularly interesting when the tool dimensions are smaller and fully com-

patible with the available measurement volume. It was precisely the need to understand and manage these specific peculiarities that motivated the development of the scan alignment and fusion procedure described in the following section.

4.3 3D Reconstruction

This section describes the computational workflow developed to transform raw point clouds exported from GoPxL into a coherent three-dimensional representation of the cutting tool and, subsequently, into a dedicated tool for the local geometric analysis of its functional surfaces. Although the two investigated technologies rely on different acquisition modes—continuous scanning for laser triangulation and single-shot acquisition for structured light—the entire procedure was built within a common geometric framework. In this framework, the various views are mapped into a single reference system centered on the tool.

Compared to the initial setup of this work, where the focus was primarily on exporting transformed point clouds to external software such as CloudCompare for surface reconstruction or CAD modeling, the code evolution progressively shifted the core of the analysis to Matlab. This choice was driven by the fact that, while external environments remain useful for post-processing and certain surface reconstruction trials, they did not always guarantee a sufficiently faithful representation of the areas of greatest metrological interest. This was particularly evident near the cutting edges, where standard meshing algorithms tended to introduce an artificial smoothing of the actual geometry.

For this reason, the procedure was structured into two distinct but complementary scripts. The first is dedicated to the global geometric reconstruction of the tool starting from .pcd scans, while the second utilizes the resulting merged point cloud to perform an interactive analysis of local sections, aimed at evaluating the inclination of the functional surfaces. In this perspective, Matlab was employed not merely as a pre-processing environment, but as a comprehensive tool for reconstruction, visualization, and geometric analysis. The .xyz files generated by the first script remain useful as neutral and portable outputs, ready to be loaded into external platforms

such as CloudCompare or similar software for further surface reconstruction or CAD generation attempts. However, the primary results discussed in this section derive directly from the plots and interfaces developed in Matlab, as this environment allowed for more rigorous control over the measured geometry and its interpretation.

4.3.1 Workflow Architecture

The entire pipeline can be interpreted as consisting of two successive levels, each associated with a specific Matlab script.

The first level is dedicated to the global three-dimensional reconstruction of the tool. Starting from a set of partial scans acquired at known angular orientations, the code constructs a comprehensive point cloud expressed in a unique and physically significant reference system. In this phase, the fundamental operations are:

- Import of .pcd files and reading of x, y, z coordinates;
- Preliminary filtering of invalid points;
- Interactive selection of two reference sections on the cylindrical shank;
- Estimation of the actual tool axis based on the centers of these sections;
- Definition of the reference origin and construction of the rigid alignment transformation;
- Phase rotation of the different views according to the acquisition angle;
- Vertical synchronization of the scans;
- Export of the results in .xyz, .pcd, and .mat formats;
- Generation of 3D scatter previews.

The second level is focused on local sectional analysis. In this case, the code uses the merged cloud produced by the first script as direct input and allows for the analysis of specific regions of the tool in a two-dimensional form. The main operations performed in this phase are:

- Reloading of the merged cloud and initial visualization of the global geometry;

- Interactive selection of the Y coordinate corresponding to the area to be analyzed;
- Extraction and representation of the section in the $X - Z$ plane;
- Definition of an interactive Region of Interest (ROI) on the profile;
- Robust linear fitting on the points contained within the ROI;
- Calculation of slopes to evaluate key geometric parameters of the tool

In this manner, the first script provides a coherent global reconstruction of the tool, while the second translates this reconstruction into a practical tool for the local analysis of functional geometries.

4.3.2 Geometric Reconstruction of the Tool

The first script is designed to transform a set of partial scans of the tool into a single merged point cloud, aligned within a unique and coherent reference system. As input, the code reads the scans in `.pcd` format, extracts their Cartesian coordinates, and removes invalid points, so that all subsequent operations are performed on a numerically consistent three-dimensional dataset. Denoting the imported cloud as

$$\mathbf{P} = \begin{bmatrix} x_1 & y_1 & z_1 \\ x_2 & y_2 & z_2 \\ \vdots & \vdots & \vdots \\ x_N & y_N & z_N \end{bmatrix} \tag{4.1}$$

the first stage consists of filtering out all points for which at least one coordinate is not finite.

Interactive selection of the reference slices on the shank

The first scan is then used as a reference for estimating the actual longitudinal axis of the tool. To this end, the code asks the user to select two different height levels along the cylindrical shank, namely the most regular portion of the tool and the one least affected by the presence of the cutting edges. Around each selected level y_k, with $k \in \{1, 2\}$, a slice of points is extracted according to

$$\mathcal{S}_k = \{\mathbf{p}_i = (x_i, y_i, z_i) \ : \ |y_i - y_k| \leq \Delta y\} \tag{4.2}$$

where Δy denotes the half-thickness of the selected section.

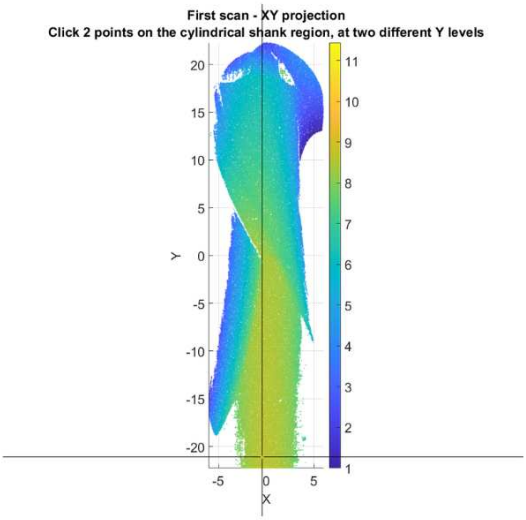

Figure 4.8: Interactive selection of two height levels along the cylindrical shank of the first scan, used to estimate the actual axis of the tool.

Estimation of the section centers

For each slice, the section center is estimated in the transverse $X-Z$ plane. In the current implementation, the preferred solution is a robust circle fitting procedure, which is geometrically consistent with the cylindrical shape of the shank. If (a_k, b_k) denotes the center of the fitted circle and r_k its radius, the local model is

$$(x - a_k)^2 + (z - b_k)^2 = r_k^2 \tag{4.3}$$

and the corresponding three-dimensional reference point is

$$\mathbf{C}_k = \begin{pmatrix} a_k \\ y_k \\ b_k \end{pmatrix} \tag{4.4}$$

Whenever the circular fit is not sufficiently stable, the code automatically falls back to the centroid of the points in the slice, expressed as

$$\mathbf{C}_k = \begin{pmatrix} \bar{x}_k \\ y_k \\ \bar{z}_k \end{pmatrix}, \qquad \bar{x}_k = \frac{1}{N_k}\sum_{i=1}^{N_k} x_i, \qquad \bar{z}_k = \frac{1}{N_k}\sum_{i=1}^{N_k} z_i \tag{4.5}$$

This choice makes it possible to maintain a reliable estimate of the section center even when the local distribution of points is not ideal.

Estimation and alignment of the actual tool axis

Once the two section centers $\mathbf{C}_1$ and $\mathbf{C}_2$ have been identified, the actual axis of the tool is obtained from the normalized vector joining them:

$$\mathbf{v}_{\text{axis}} = \frac{\mathbf{C}_2 - \mathbf{C}_1}{\|\mathbf{C}_2 - \mathbf{C}_1\|} \tag{4.6}$$

The estimated axis is then aligned with the vertical direction of a common reference system, defined as

$$\mathbf{v}_{\text{target}} = \begin{pmatrix} 0 \\ 1 \\ 0 \end{pmatrix} \tag{4.7}$$

To construct the rigid transformation, the code first defines a reference origin as the midpoint between the two section centers:

$$\mathbf{o}_{\text{ref}} = \frac{\mathbf{C}_1 + \mathbf{C}_2}{2} \tag{4.8}$$

Each point of the cloud is then translated with respect to this origin,

$$\tilde{\mathbf{p}} = \mathbf{p} - \mathbf{o}_{\text{ref}} \tag{4.9}$$

and subsequently rotated through an alignment matrix $\mathbf{R}_{\text{align}}$, computed through Rodrigues' formula starting from the vectors $\mathbf{v}_{\text{axis}}$ and $\mathbf{v}_{\text{target}}$. Defining

$$\mathbf{k} = \mathbf{v}_{\text{axis}} \times \mathbf{v}_{\text{target}}, \qquad s = \|\mathbf{k}\|, \qquad c = \mathbf{v}_{\text{axis}} \cdot \mathbf{v}_{\text{target}} \tag{4.10}$$

and the associated skew-symmetric matrix

$$[\mathbf{k}]_\times = \begin{bmatrix} 0 & -k_z & k_y \\ k_z & 0 & -k_x \\ -k_y & k_x & 0 \end{bmatrix} \tag{4.11}$$

the alignment matrix can be written as

$$\mathbf{R}_{\text{align}} = \mathbf{I} + [\mathbf{k}]_\times + [\mathbf{k}]_\times^2 \frac{1-c}{s^2} \tag{4.12}$$

The aligned points are therefore written as

$$\mathbf{p}_{\text{align}} = \mathbf{R}_{\text{align}}(\mathbf{p} - \mathbf{o}_{\text{ref}}) \tag{4.13}$$

This operation effectively straightens the tool and places all scans into a common reference system in which the longitudinal axis coincides with Y.

Phase rotation and vertical synchronization

Once the common reference system has been defined, each scan is rotated around the Y-axis according to its acquisition phase. For the i-th view, the phase angle is given by

$$\theta_i = (i-1)\Delta\theta \tag{4.14}$$

where $\Delta\theta$ is the angular step between consecutive acquisitions. The corresponding phase-rotation matrix is

$$\mathbf{R}_{\text{phase}}(\theta_i) = \begin{bmatrix} \cos\theta_i & 0 & \sin\theta_i \\ 0 & 1 & 0 \\ -\sin\theta_i & 0 & \cos\theta_i \end{bmatrix} \tag{4.15}$$

The complete transformation applied to the points of the i-th scan can therefore be written as

$$\mathbf{p}_i^* = \mathbf{R}_{\text{phase}}(\theta_i)\, \mathbf{R}_{\text{align}}\, (\mathbf{p}_i - \mathbf{o}_{\text{ref}}) \tag{4.16}$$

A further vertical synchronization is then introduced. In a first stage, the code can compensate for coarse differences between scans by comparing their minimum Y-values. In a second stage, after alignment and phase rotation, the global minimum of the transformed views is computed and subtracted from all points, so that the common minimum is mapped to $Y = 0$. In this way, the lower part of the tool, which approximately corresponds to the tip, is taken as a shared vertical reference.

Outputs and global 3D visualization

At the end of the process, the first script generates the aligned scans and the overall reconstruction in `.pcd`, `.xyz`, and `.mat` formats, together with metadata and a direct three-dimensional visualization in Matlab. This stage therefore supports both data export and an immediate verification of reconstruction consistency.

For laser triangulation, the final reconstruction was obtained by merging four scans acquired at angular steps of 90°. In this framework, the configuration proved sufficient to obtain a globally complete and geometrically coherent model.

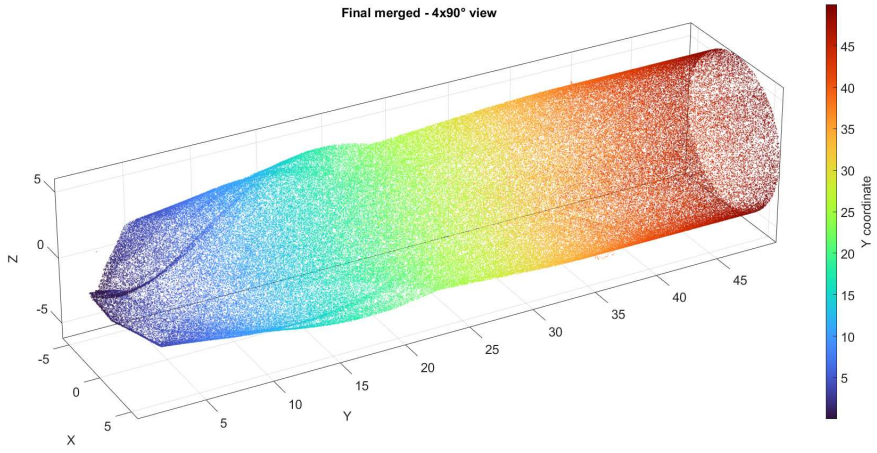

Figure 4.9: Three-dimensional reconstruction obtained by laser triangulation from four scans acquired at 90° angular intervals.

The same procedure was then applied to the structured-light dataset. In a first test, four scans acquired at 90° intervals were used, following the same logic as for laser triangulation. In this case, however, the reconstruction

clearly showed large missing regions, due to the smaller surface portion captured in each individual snapshot.

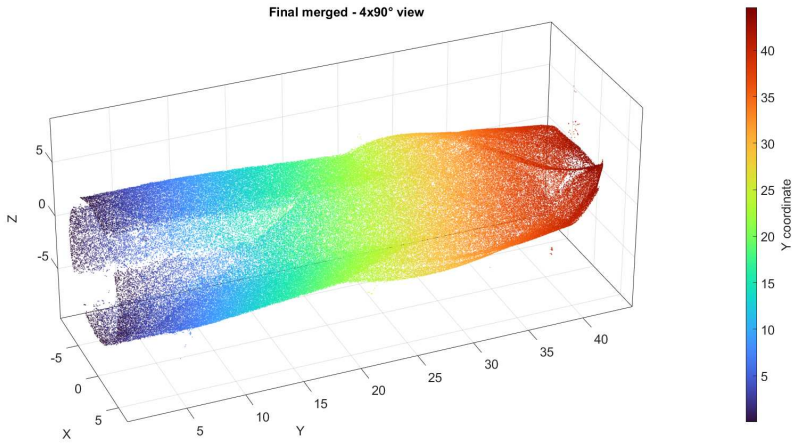

Figure 4.10: Three-dimensional reconstruction obtained by structured light from four scans acquired at 90° intervals.

Based on this result, a second test was carried out by increasing the number of acquisitions and reducing the angular step to 45°, thus obtaining a configuration with eight views. This choice improved the overall surface coverage of the tool and yielded a much more complete and readable reconstruction, although at the cost of a more demanding processing stage.

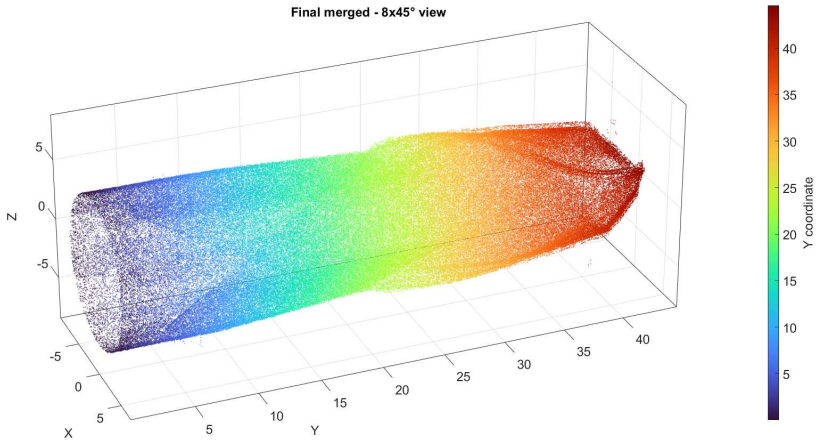

Figure 4.11: Three-dimensional reconstruction obtained by structured light from eight scans acquired at 45° intervals.

Overall, these visualizations show that, in the case of structured light, a sufficient number of scans enables a coarse reconstruction of the tool's 3D geometry, but at the cost of greater complexity in the alignment and registration stages. By contrast, laser triangulation requires only four scans to obtain a more faithful and consistent reconstruction of the tool.

4.3.3 Interactive Analysis of Local Sections

While the first script builds a global three-dimensional representation of the tool, the second focuses on local geometric analysis. It extracts transverse sections from selected regions of the reconstructed tool and uses these two-dimensional profiles to evaluate functional quantities, such as the inclination of the rake and clearance surfaces.

The script takes as input the merged cloud generated by the first script, `merged_aligned.xyz`, and displays a three-dimensional preview of the reconstructed tool. The user then selects a point on a $Y-Z$ projection of the cloud, and the corresponding Y-coordinate defines the section height.

Interactive selection of the section height

This first interactive step allows the region of interest to be chosen directly on the reconstructed geometry. The section is therefore not defined a priori, but selected according to the area to be analysed, for example near the cutting region or along a surface whose inclination must be evaluated.

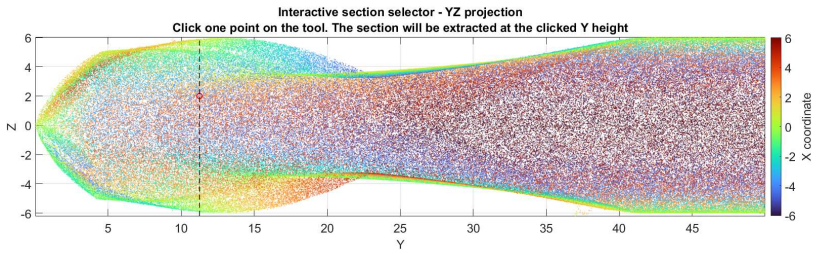

Figure 4.12: Interactive selection of the section height on the $Y-Z$ projection of the reconstructed cloud.

Extraction of the thin profile

Once the height y_s is selected, the code extracts a thin portion of the point cloud centred on that section, in order to approximate a two-dimensional profile of the tool in the $X-Z$ plane. The extracted set can be written as

$$\mathcal{P}(y_s) = \{\mathbf{p}_i : |y_i - y_s| \leq \Delta y_{\text{thin}}\} \tag{4.17}$$

where Δy_{thin} denotes the half-thickness of the selected section; in this study, it was set in the range 10–20 μm.

Restricting the analysis to such a thin layer reduces the overlap of points from different axial levels and yields a clearer two-dimensional representation of the local geometry. This is particularly important in the regions of greatest functional interest, where the inclination of the rake and clearance surfaces must be evaluated as accurately as possible.

A clear difference emerged between the two acquisition technologies. In the case of laser triangulation, the extracted profile was sufficiently regular and well defined to support the subsequent local analysis. By contrast, when the same procedure was applied to the structured-light reconstruction, the resulting section appeared much less homogeneous and was affected by the overlap of neighbouring surfaces that were not matched consistently. As a result, the extracted profile could not be interpreted unambiguously, and the subsequent ROI-based local analysis could not be applied reliably.

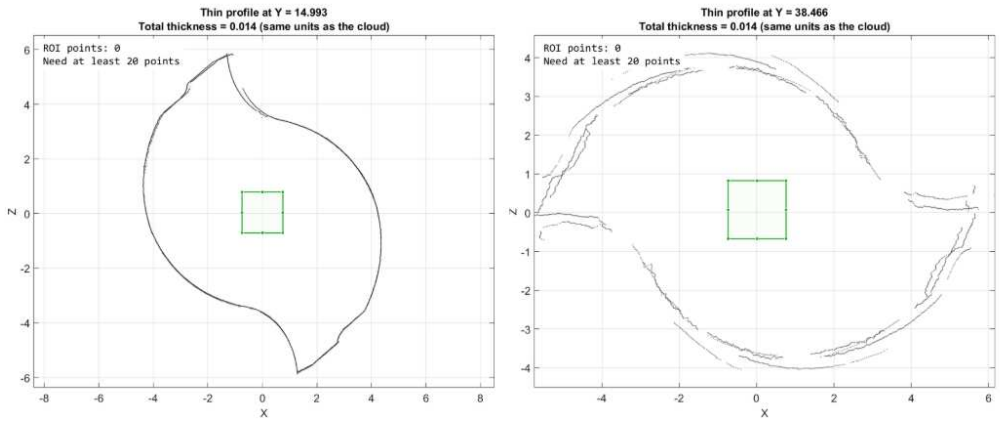

Figure 4.13: Comparison of extracted thin profiles: laser triangulation (left) and structured light (right) results.

ROI-based evaluation of local geometric parameters

With regard to the thin profile extracted from the laser triangulation reconstruction, the script allows the user to define an interactive rectangular ROI in the region to be examined. Within this window, a line-fitting routine developed in parallel within the project is used to approximate the local edges and surfaces of interest. Since the detailed development of this fitting algorithm was carried out mainly by my colleague, it is not discussed here at the algorithmic level. In the present section, the focus is instead placed on how this routine is used within the overall workflow and on the geometric quantities that can be extracted from it.

In practical terms, this procedure proved effective when applied to the clear profiles obtained from the laser-triangulation reconstruction, whereas it was not considered sufficiently reliable in the case of structured-light reconstructions, for which the extracted sections remained too irregular and ambiguous. Through the analysis of the laser-based profiles, the user can identify local linear features and directly obtain the parameters of greatest interest for tool analysis, such as the inclination of the clearance surface, the inclination of the rake surface, and the lengths of the fitted segments. The graphical output therefore acts as an operational interface between the reconstructed three-dimensional dataset and the subsequent geometric interpretation of the tool section.

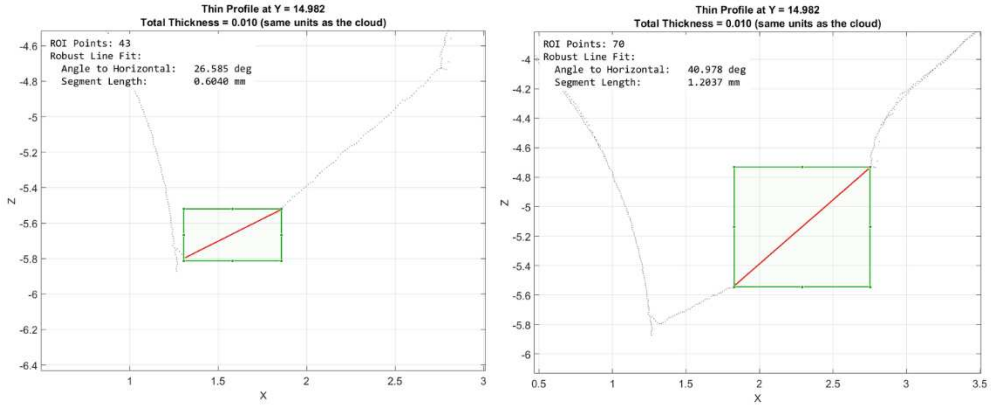

Figure 4.14: Examples of local analysis performed on the extracted thin profile obtained from laser triangulation.

In this way, the second script does not aim to reconstruct the tool globally, but rather to transform the reconstructed cloud into a practical environment

for the local inspection of the section geometry. This step is particularly relevant because it enables the transition from the three-dimensional acquisition stage to the direct evaluation of the functional parameters of interest.

4.4 Analysis of Results

After defining the 3D reconstruction workflow and verifying its geometric consistency, the results obtained with the two investigated technologies were analysed separately.

With regard to structured light, the results confirmed the limitations already observed in the extracted sectional profiles. Within the workflow adopted here, based on three-dimensional reconstruction, sectioning, and subsequent local analysis, neither the four-view nor the eight-view configuration provided profiles sufficiently clear and homogeneous to support a reliable angular evaluation. For this reason, the two-dimensional analysis of the angles was not pursued further for the structured-light reconstruction.

This does not imply, however, that the technology should be excluded in absolute terms. If the individual scans are considered separately, extracting local profiles directly from single acquisitions rather than from the complete merged reconstruction, structured light may still allow a sufficiently rigorous observation of tool surfaces, particularly in the case of small tools. This possibility must nevertheless be considered with the awareness that the surface noise associated with structured light remains significantly higher than that observed in laser triangulation.

By contrast, laser triangulation provided a much more suitable basis for the intended analysis. Already with four scans acquired at 90°, the reconstructed tool geometry proved sufficiently complete and coherent to allow the effective use of the interactive section-selection interface developed in Matlab. This made it possible to rapidly identify the region of interest, extract clear local profiles, and proceed with the subsequent two-dimensional analysis of the relevant geometric quantities.

For consistency within the overall structure of the thesis work, the detailed formulation of the line-fitting system and the angular analysis procedure is discussed in my colleague's thesis, whereas the present work focuses on

the three-dimensional reconstruction stage that enabled such an analysis. In this section, I therefore report only the final values obtained from the two-dimensional measurements carried out on the profiles extracted from the laser-triangulation reconstruction.

Table 4.3 summarizes the main measured quantities obtained for the analysed ball-nose tools and compares them with the corresponding expected values provided by the nominal tool geometry. The reported results confirm that the reconstruction obtained by laser triangulation was sufficiently clear and stable to support the extraction of measurable angular and dimensional parameters.

Feature	**Ball Nose 6 mm**	**Ball Nose 12 mm**
Rake angle [°]	9.9489°	5.7410°
Expected	$6° \pm 1°$	$6° \pm 1°$
Primary clearance [°]	11.2728°	13.6422°
Expected	$14° \pm 2°$	$14° \pm 2°$
Primary clearance [mm]	0.2811 mm	0.6115 mm
Expected	0.3 mm	0.6 mm
Secondary clearance [°]	28.4006°	28.0714°
Expected	$30° \pm 2°$	$30° \pm 2°$
Secondary clearance [mm]	0.7017 mm	1.2187 mm
Expected	0.6 mm	1.2 mm

Table 4.3: Summary of the final measurements obtained from the two-dimensional analysis.

Chapter 5

Conclusions

This thesis investigated the feasibility of extending industrial tool presetting from a purely two-dimensional paradigm toward a three-dimensional measurement framework, within a collaborative research activity carried out with iMAGE S and Speroni. In this context, the main contribution of the present work lies in the development and preliminary validation of a complete workflow for the three-dimensional reconstruction of cutting tools from multiple optical acquisitions, with the aim of obtaining a coherent geometrical representation of the tool capable of supporting the local analysis of its functional surfaces.

The work was developed in parallel with a complementary activity focused on the two-dimensional evaluation of local tool parameters. Within this framework, the role of the present thesis was not to replace the 2D analysis, but to provide its geometric basis, making its application more flexible and physically meaningful. In particular, the proposed reconstruction pipeline makes it possible to move from the observation of multiple scans to a complete three-dimensional representation of the tool, from which specific sections can be extracted a posteriori at selected heights and analysed locally according to the region of interest.

From a technological point of view, the comparative study and the experimental validation confirmed that, among the investigated solutions, laser triangulation and structured light were the two most promising candidates for integration into the industrial presetting context. However, the three-dimensional reconstruction attempts highlighted a clear difference in per-

formance between the two approaches. Structured light proved capable of providing an overall three-dimensional representation of the tool and, in some cases, showed potentially useful behaviour, especially for small tools and for the direct observation of individual acquisitions. Within the reconstruction workflow developed in this thesis, however, the corresponding data were affected by higher surface noise, reduced useful coverage in each view, and greater difficulty in the alignment and registration of multiple scans. As a consequence, neither the four-view nor the eight-view reconstruction provided sectional profiles sufficiently clear and homogeneous to support a reliable local angular analysis.

By contrast, laser triangulation provided a much more robust basis for the intended application. Already with four scans acquired at angular intervals of 90°, the reconstructed geometry proved sufficiently complete and coherent to enable the generation of a faithful three-dimensional representation of the tool. This result is particularly significant because it shows that a relatively limited number of views is enough to obtain a geometrical model that is not only visually meaningful, but also suitable for subsequent metrological interpretation. The Matlab workflow developed in this work made it possible to import, filter, align, and roto-translate the individual scans into a common reference system, merge them into a single point cloud, and interactively select the height at which the local profile had to be extracted.

This aspect represents one of the most relevant outcomes of the work. The reconstruction is not intended merely as a graphical visualization of the tool, but as a practical geometric environment in which the operator can explore the full 3D morphology of the component and decide, at a later stage, where to perform the local inspection. In this way, the tool is no longer analysed only through its instantaneous silhouette, but through a reconstructed spatial model from which thin bidimensional sections can be derived in the areas of greatest functional interest. This introduces a concrete element of innovation with respect to the conventional presetting logic, since it opens the possibility of separating the acquisition of the geometry from the subsequent evaluation of the section.

Overall, the results confirm that laser triangulation is the most suitable technology for a three-dimensional extension of industrial tool presetting. The

work developed in this thesis therefore represents a preliminary but concrete validation of a new measurement paradigm, in which three-dimensional reconstruction and local two-dimensional analysis become two integrated stages of the same metrological workflow.

5.1 Future Perspectives

Although the results obtained in this thesis are encouraging, further developments are still required to transform the current workflow into a fully integrated industrial solution.

First, the entire reconstruction and analysis chain should be integrated more directly into the software architecture of the presetting machine. At present, the procedure relies on exporting point clouds and subsequently processing them in Matlab. A future development should therefore aim at embedding the main functionalities of scan alignment, reconstruction, and section extraction into a dedicated industrial software environment, in order to reduce manual intervention and improve usability under production conditions.

Second, the interaction between the three-dimensional reconstruction stage and the subsequent local analysis could be further strengthened. In the current implementation, the reconstructed cloud is already used as a practical environment for selecting the section of interest. In a future version, this step could be made more automatic, for instance by introducing strategies for the assisted identification of relevant tool regions, such as the cutting edge, the rake face, or the primary and secondary clearance zones. This would make the overall workflow more efficient and more consistent with the needs of industrial presetting.

Third, the results obtained suggest that laser triangulation should remain the main reference technology for future developments, whereas structured light may still deserve further investigation under more specific operating conditions. Although it did not prove sufficiently robust within the multi-view reconstruction workflow adopted in this work, its behaviour in individual acquisitions, particularly in the case of smaller tools, suggests that it may still offer some potential in applications where full multi-view merging is not required or where the acquisition strategy can be further optimized.

Finally, from an industrial perspective, the most promising implication of this work lies in the possibility of enriching future Speroni presetting systems with a genuine three-dimensional analysis capability. Such an evolution would not only improve the geometric understanding of the tool, but could also introduce a more advanced interaction paradigm, in which the operator is able to visualize the complete reconstructed geometry of the tool and inspect it locally in a flexible and selective way. In this sense, the work developed in this thesis represents not only a technical feasibility study, but also a concrete first step toward a possible innovation path for next-generation industrial presetting machines.

Bibliography

[1] D. A. Stephenson and J. S. Agapiou, *Metal Cutting Theory and Practice*. Boca Raton, FL: CRC Press, 3 ed., 2016. Official product page. Accessed: 2026-01-9.

[2] MVTec Software GmbH, *Solution Guide III-C – 3D Vision*. MVTec Software GmbH, n.d. Official product page. Accessed: 2026-01-10.

[3] H.-R. Chen and L.-C. Chen, "Full-field chromatic confocal microscopy for surface profilometry with sub-micrometer accuracy," *Optics and Lasers in Engineering*, vol. 161, p. 107384, 2023. Official product page. Accessed: 2026-01-12.

[4] LMI Technologies, "Gocator 2500 series: 3d smart line profile sensors – datasheet," tech. rep., LMI Technologies, 2025. Official product page. Accessed: 2026-01-12.

[5] Speroni S.p.A., "Stp futura." `https://speroni.info/en/prodotti/stp-futura/`, n.d. Official product page. Accessed: 2026-01-12.

[6] ZOLLER, "smile." `https://global.zoller.info/in/products/presetting-measuring/vertical-devices/smile`, n.d. Official product page. Accessed: 2026-01-15.

[7] HAIMER, "Tool presetting technology." `https://www.haimer.com/en/products/presetting-technology`, n.d. Official product page. Accessed: 2026-02-9.

[8] Bruker Alicona, "Focus variation." `https://www.alicona.com/en/technologies/focus-variation`, n.d. Official technology page. Accessed: 2026-02-22.

[9] J. G. D. M. França, M. A. Gazziro, A. N. Ide, and J. H. Saito, "A 3d scanning system based on laser triangulation and variable field of view," in *Proceedings of the IEEE International Conference on Image Processing (ICIP)*, vol. 1, pp. I–425–I–428, 2005. Official product page. Accessed: 2026-02-25.

[10] MVTec Software GmbH, *HALCON Operator Reference: create_sheet_of_light_model*. MVTec Software GmbH, 2025. Official product page. Accessed: 2026-03-15.

[11] F. J. Brosed, J. J. Aguilar, D. Guillomía, and J. Santolaria, "3d geometrical inspection of complex geometry parts using a novel laser triangulation sensor and a robot," *Sensors*, vol. 11, no. 1, pp. 90–110, 2011. Official product page. Accessed: 2026-03-16.

[12] J. Schlarp, E. Csencsics, and G. Schitter, "Optical scanning of a laser triangulation sensor for 3-d imaging," *IEEE Transactions on Instrumentation and Measurement*, vol. 69, no. 6, pp. 3606–3613, 2020. Official product page. Accessed: 2026-03-17.

[13] LMI Technologies, "Official website and three dimensional sensor specifications." `https://lmi3d.com/`, 2026. Official product page. Accessed: 2026-03-20.

[14] Teledyne Vision Solutions, "Official website and profiler specifications." `https://www.teledynevisionsolutions.com/`, 2026. Official product page. Accessed: 2026-03-20.

[15] Automation Technology, "At sensors official website and technical datasheets." `https://www.at-sensors.com/`, 2026. Official product page. Accessed: 2026-03-20.

[16] J. Geng, "Structured-light 3d surface imaging: a tutorial," *Advances in Optics and Photonics*, vol. 3, no. 2, pp. 128–160, 2011. Official product page. Accessed: 2026-03-27.

[17] J. Salvi, S. Fernandez, T. Pribanic, and X. Llado, "A state of the art in structured light patterns for surface profilometry," *Pattern Recognition*, vol. 43, no. 8, pp. 2666–2680, 2010. Official product page. Accessed: 2026-04-2.

[18] C. Zuo, S. Feng, L. Huang, T. Tao, W. Yin, and Q. Chen, "Phase shifting algorithms for fringe projection profilometry: A review," *Optics and Lasers in Engineering*, vol. 109, pp. 23–59, 2018. Official product page. Accessed: 2026-04-7.

[19] H. Zhang, L. Ji, S. Liu, S. Li, S. Han, and X. Zhang, "Three-dimensional shape measurement of a highly reflected, specular surface with structured light method," *Applied Optics*, vol. 51, no. 31, pp. 7724–7732, 2012. Official product page. Accessed: 2026-04-8.

[20] S. Feng, C. Zuo, L. Zhang, T. Tao, Y. Hu, W. Yin, J. Qian, and Q. Chen, "Calibration of fringe projection profilometry: A comparative review," *Optics and Lasers in Engineering*, vol. 143, p. 106622, 2021. Official product page. Accessed: 2026-04-11.

[21] R. Hartley and A. Zisserman, *Multiple View Geometry in Computer Vision*. Cambridge University Press, 2 ed., 2004. Official product page. Accessed: 2026-04-10.

[22] R. Szeliski, *Computer Vision: Algorithms and Applications*. Springer, 2 ed., 2022. Official product page. Accessed: 2026-04-8.

[23] IDS Imaging Development Systems GmbH, "Ensenso stereo 3d cameras." `https://en.ids-imaging.com/ensenso-stereo-3d-camera.html`, n.d. Official product page. Accessed: 2026-04-9.

[24] R. Danzl, F. Helmli, and S. Scherer, "Focus variation – a robust technology for high resolution optical 3d surface metrology," *Strojniški vestnik – Journal of Mechanical Engineering*, vol. 57, no. 3, pp. 245–256, 2011. Official product page. Accessed: 2026-04-2.

[25] Xpert3D, "Alicona infinitefocus sl: Optical 3d micro coordinate measurement system." `https://xpert3d.ca/alicona/alicona-infinitefocus-sl/`, 2026. Official product page. Accessed: 2026-04-2.

[26] J. Li, R. Ma, and J. Bai, "High-precision chromatic confocal technologies: A review," *Micromachines*, vol. 15, no. 10, p. 1224, 2024. Official product page. Accessed: 2026-02-26.

[27] JCGM, *Evaluation of Measurement Data – Guide to the Expression of Uncertainty in Measurement*. 2008. Official product page. Accessed: 2026-02-23.

[28] JCGM, *International Vocabulary of Metrology – Basic and General Concepts and Associated Terms (VIM)*. 2012. Official product page. Accessed: 2026-02-12.

[29] E. O. Doebelin, *Measurement Systems: Application and Design*. 2008. Official product page. Accessed: 2026-03-3.

[30] S. Shirmohammadi, L. Mari, and D. Petri, "A proposito della (spesso sbagliata...) rappresentazione grafica dell'accuratezza e della precisione," *Tutto_Misure*, vol. 2, 2021. Official product page. Accessed: 2026-03-19.

[31] ISO, *Accuracy (Trueness and Precision) of Measurement Methods and Results – Part 1: General Principles and Definitions*. 1994. Official product page. Accessed: 2026-03-21.

[32] International Organization for Standardization, "ISO 3650:1998 – Geometrical Product Specifications (GPS) – Length standards – Gauge blocks," 1998. Official product page. Accessed: 2026-03-12.

[33] LMI Technologies, *GoPxL Web Interface Manual for Gocator Laser Line Profilers*. LMI Technologies, 2025. Official product page. Accessed: 2026-03-22.

[34] LMI Technologies, "Understanding laser line profilers: Peak extraction and sub-pixel interpolation," technical white paper, LMI Technologies Inc., 2022. Official product page. Accessed: 2026-04-10.

[35] I. Kåsa, "A curve fitting procedure and its error analysis," *IEEE Transactions on Instrumentation and Measurement*, vol. 25, no. 1, pp. 8–14, 1976. Official product page. Accessed: 2026-04-10.